



# Dynamic Models for Wind Turbines and Wind Power Plants

**January 11, 2008 – May 31, 2011**

Mohit Singh  
Surya Santoso (Principal Investigator)  
*The University of Texas at Austin*  
*Austin, Texas*

NREL is a national laboratory of the U.S. Department of Energy, Office of Energy Efficiency & Renewable Energy, operated by the Alliance for Sustainable Energy, LLC.

**Subcontract Report**  
NREL/SR-5500-52780  
October 2011

Contract No. DE-AC36-08GO28308

# Dynamic Models for Wind Turbines and Wind Power Plants

**January 11, 2008 – May 31, 2011**

Mohit Singh  
Surya Santoso (Principal Investigator)  
*The University of Texas at Austin*  
*Austin, Texas*

NREL Technical Monitor: Eduard Muljadi  
Prepared under Subcontract No. XEE-8-77567-01

**NREL is a national laboratory of the U.S. Department of Energy, Office of Energy Efficiency & Renewable Energy, operated by the Alliance for Sustainable Energy, LLC.**

**This publication received minimal editorial review at NREL.**

### **NOTICE**

This report was prepared as an account of work sponsored by an agency of the United States government. Neither the United States government nor any agency thereof, nor any of their employees, makes any warranty, express or implied, or assumes any legal liability or responsibility for the accuracy, completeness, or usefulness of any information, apparatus, product, or process disclosed, or represents that its use would not infringe privately owned rights. Reference herein to any specific commercial product, process, or service by trade name, trademark, manufacturer, or otherwise does not necessarily constitute or imply its endorsement, recommendation, or favoring by the United States government or any agency thereof. The views and opinions of authors expressed herein do not necessarily state or reflect those of the United States government or any agency thereof.

Available electronically at <http://www.osti.gov/bridge>

Available for a processing fee to U.S. Department of Energy and its contractors, in paper, from:

U.S. Department of Energy  
Office of Scientific and Technical Information  
P.O. Box 62  
Oak Ridge, TN 37831-0062  
phone: 865.576.8401  
fax: 865.576.5728  
email: <mailto:reports@adonis.osti.gov>

Available for sale to the public, in paper, from:

U.S. Department of Commerce  
National Technical Information Service  
5285 Port Royal Road  
Springfield, VA 22161  
phone: 800.553.6847  
fax: 703.605.6900  
email: [orders@ntis.fedworld.gov](mailto:orders@ntis.fedworld.gov)  
online ordering: <http://www.ntis.gov/help/ordermethods.aspx>

Cover Photos: (left to right) PIX 16416, PIX 17423, PIX 16560, PIX 17613, PIX 17436, PIX 17721



Printed on paper containing at least 50% wastepaper, including 10% post consumer waste.

## **Abstract**

Manufacturer-specific models of wind turbines are favored for use in wind power interconnection studies. While they are detailed and accurate, their usages are limited to the terms of the non-disclosure agreement, thus stifling model sharing. The primary objective of the work proposed is to develop universal manufacturer-independent wind power plant models that can be shared, used, and improved without any restrictions by project developers, manufacturers, and engineers. Each of these models includes representations of general turbine aerodynamics, the mechanical drive-train, and the electrical characteristics of the generator and converter, as well as the control systems typically used. To determine how realistic model performance is, the performance of one of the models (doubly-fed induction generator model) has been validated using real-world wind power plant data. This work also documents selected applications of these models.

## Contents

<b>Abstract</b> .....	<b>4</b>
<b>1. Introduction</b> .....	<b>9</b>
1.1 Background and Motivation .....	9
1.1.1 The changing power system .....	9
1.1.2 Wind power integration and wind turbine modeling .....	9
1.2 Research Objectives .....	10
1.3 Wind Turbine Technologies .....	11
1.3.1 Modern utility-scale wind turbines .....	11
1.3.2 Classification of wind turbines .....	11
1.4 Contributions .....	13
1.5 Brief Summary .....	13
<b>2. Modeling of Fixed-Speed (Type 1) Wind Turbine Generators</b> .....	<b>14</b>
2.1 Introduction to Wind Turbine Modeling .....	14
2.2 Aerodynamics .....	15
2.2.1 A brief introduction to the aerodynamics of wind turbines.....	15
2.2.2 Aerodynamic Block .....	16
2.2.3 Tip-speed ratio calculations.....	16
2.2.4 Rotor power coefficient ( $C_p$ ) calculation .....	17
2.2.5 Aerodynamic torque calculation .....	17
2.3 Mechanical Drivetrain .....	18
2.4 Induction Generator .....	21
2.5 Control Block .....	22
2.6 Complete Model Implemented in PSCAD/EMTDC .....	22
2.7 Power Curve for Fixed-Speed Model.....	22
2.8 Dynamic Response.....	23
2.9 Summary.....	24
<b>3. Modeling of Variable-Slip (Type 2) Wind Turbine Generators</b> .....	<b>25</b>
3.1 Rotor Resistance Control Concept.....	25
3.1.1 Induction machine equivalent circuit.....	25
3.1.2 Effect of rotor resistance change on equivalent circuit and torque and power equations .....	27

3.2 Methods for Rotor Resistance Control.....	28
3.2.1 Model implementation.....	28
3.2.2 Two-loop PI controller based on output power and rotor current.....	29
3.3 Dynamic Response.....	31
3.4 Summary.....	32
<b>4. Modeling of DFIG (Type 3) Wind Power Plants: Current Source Representation .....</b>	<b>33</b>
4.1 Introduction to DFIG Technology .....	33
4.2 Prior Work on DFIG Dynamic Modeling .....	33
4.2.1 Work done under IEA Wind Annex 21.....	33
4.3 Three-Phase Model: Development and Implementation .....	34
4.3.1 Doubly-Fed Induction Generators: Basic Concepts.....	34
4.3.2 Modeling Approach: Use of Regulated Current Source instead of Detailed Device Models .....	39
4.3.3 Implementation of DFIG WPP Model in PSCAD/EMTDC .....	42
4.3.4 Model Development Summary .....	50
4.4 Three-Phase Model: Steady-State Performance .....	50
4.4.1 Method of Computing Real and Reactive Power in the $qd0$ Frame with Validation .....	51
4.4.2 Wind Power Curve.....	55
4.4.3 Reactive Power Control and Less-Than-Maximum Power Output.....	57
4.4.4 Changes in Wind Speed .....	60
4.4.5 Model Performance Summary .....	62
4.5 Three-Phase Model: Validation Using Field Data .....	63
4.5.1 Introduction to the Validation Process.....	63
4.5.2 Collector System .....	63
4.5.3 Steady-State Validation: Pre-Fault .....	65
4.5.4 Dynamic Performance .....	72
4.6 Summary.....	78
<b>5. DFIG (Type 3) Wind Turbine Generators: Single-Machine Detailed Model .....</b>	<b>79</b>
5.1 Introduction.....	79
5.2 Model Development.....	79
5.2.1 Aerodynamic and Mechanical drivetrain models.....	79
5.2.2 Reference power calculation.....	80
5.2.3 Pitch control block.....	80
5.2.4 Induction generator.....	81
5.2.5 Rotor and grid side converter control for DFIG.....	81
5.2.6 Unit transformer and grid representation .....	86

5.2.7 Complete model implemented in PSCAD/EMTDC .....	86
5.3 Model Testing.....	86
5.3.1 Power curve.....	86
5.3.2 Independent real and reactive power control .....	88
5.3.3 Pitch control .....	90
5.4 Dynamic Response.....	90
5.5 Summary.....	92
<b>6. Modeling of Full-Converter (Type 4) Wind Turbine Generators Employing Permanent Magnet Alternators .....</b>	<b>93</b>
6.1 Introduction.....	93
6.2 Model Development.....	93
6.2.1 Aerodynamic and mechanical drivetrain models.....	94
6.2.2 Reference power calculation from wind speed .....	94
6.2.3 Pitch control block.....	94
6.2.4 Permanent magnet alternator .....	95
6.2.5 Rectifier and buck/boost converter for DC-link voltage control.....	96
6.2.6 Inverter .....	96
6.2.7 Unit transformer and grid representation .....	98
6.2.8 Complete model implemented in PSCAD/EMTDC .....	99
6.3 Model Testing.....	99
6.3.1 Power curve.....	99
6.3.2 Independent real and reactive power control .....	101
6.3.3 Pitch control .....	102
6.4 Dynamic Response.....	103
6.5 Summary.....	104
<b>7. Conclusion and Future Work.....</b>	<b>105</b>
7.1 Conclusion .....	105
7.2 Future Work.....	105
<b>Appendices .....</b>	<b>106</b>
<b>Appendix A: Wind Turbine Ratings and Parameters .....</b>	<b>107</b>
A.1 Fixed-Speed (Type 1) Single Turbine Estimated Ratings and Parameters (note: parameters modified for consistency across turbine types) .....	107
A.2 Variable-Slip (Type 2) Single Turbine Estimated Ratings and Parameters (note: parameters modified for consistency across turbine types) .....	107
A.3 Doubly-Fed Induction Generator (Type 3) Single Turbine Estimated Ratings and Parameters (note: parameters modified for consistency across turbine types).....	108

A.4 Full-Converter (Type 4) Single Turbine Estimated Ratings and Parameters (note: parameters modified for consistency across turbine types) .....	109
<b>Appendix B: Fifth- and Third-Order Equations for Induction Machines .....</b>	<b>110</b>
B.1 Fifth-Order Model .....	110
B.2 Third-Order Model .....	110
<b>Bibliography.....</b>	<b>111</b>

# 1. Introduction

## 1.1 Background and Motivation

### 1.1.1 The changing power system

The bulk power system was called “the largest, most complex machine ever devised by man” by Charles Steinmetz in the early 1900s, and its complexity has increased considerably since then. The basic characteristics of the power system in the 20th century were that they were comprised of 3-phase AC systems at constant voltage, used synchronous AC machines (alternators) running at constant frequency for generation, and transmitted power over significant distances [1]. Our understanding of the power system has been based on these underlying characteristics. However, in the 21st century, these characteristics no longer apply universally and our understanding of power system concepts is no longer quite as firmly entrenched. The power system today is expected to integrate a variety of AC and DC systems in all three areas: generation, transmission and distribution. It is expected to be able to handle both synchronous and asynchronous generators, centralized and distributed resources, and to handle inherently controllable as well as inherently intermittent and variable sources of energy. Moreover, the need for a large centralized bulk power system as a one-size-fits-all solution for every energy need is being questioned, and smaller grids (“microgrids”) are gaining currency in niche applications. These grids still require the bulk power system to back them up. These changes in the bulk power system are a result of a multitude of factors [2]. In the United States, the capacity of wind power and other renewables being interconnected and being planned for interconnection is steadily increasing. This trend is expected to continue due to increased concerns about environmental issues such as carbon emissions and global climate change, energy security in a less-than-unipolar world, and job creation in a recession environment. Renewables are at the nexus of all these complex issues. Of all modern renewable energy sources, wind power has been the most successful, and hence poses the most immediate integration challenge.

### 1.1.2 Wind power integration and wind turbine modeling

Wind power installed capacity is growing exponentially [3]. Integration of wind power is proceeding at a rapid pace, and it is feasible that the United States may receive 20% of its electrical energy from wind by 2030 [2]. This 20% target corresponds to 300 GW installed capacity (mostly asynchronous). Wind turbine technology has been evolving continuously and has come a long way since the energy crisis of the 1970s when wind power began its resurgence [4], with individual wind turbines of 5-MW capacity being installed today as compared to wind turbines of the past which were rated in tens of kilowatts. As wind turbine technology matures and wind power penetration levels increase, interconnecting a large-scale wind power plant (WPP) into the bulk power system has become a more important issue. The literature available suggests that large-scale WPPs can have a significant impact on the grid [5–12], and the topic has been a matter of interest in the United States since the late 1970s and early 1980s. This was a period when wind turbine technology was starting to become viable, and concerns about the effects of large-scale WPPs on the grid began to be voiced [13–18]. The intermittent and variable nature of wind, the reliance of most wind power plants on induction generators, and the fact that wind generation tends to displace conventional generation, negatively affect system stability [19]. Some experiences of integrating wind power into the existing grid in Denmark, Sweden, Germany, California, the Midwestern United States and India have been discussed in [20]. The work described in this report directly addresses these effects of wind power integration on the grid through the development of generic, manufacturer-independent wind power plant simulation models for interconnection studies. Right now, there is a need for wind turbine dynamic models, with potential users being power system planners and operators, researchers, consultants, wind plant developers. Reliability entities also need validated, non-proprietary models to meet reliability standards such as those set by the North American Electric Reliability Corporation (NERC). The purpose of these models is to observe the impact of wind turbine generators (WTGs) on the power system during dynamic events such as loss of load, loss

of generation, loss of line, loss of wind, short circuits and voltage ride-through. Interconnection studies require steady-state and dynamic transient models of a WPP along with its collector system. Failure to perform proper interconnection studies could lead to non-optimal designs and operations of the WPP. Numerical power system simulation tools developed specifically for power systems and dynamic modeling, such as PSCAD/EMTDC, SIMPOW, or PSS/E may be used for these interconnection studies [21–23]. General purpose modeling software such as MATLAB/Simulink may also be used. The dynamic models of wind plants for power system studies are not usually built-in in these software tools, and have to be developed independently. Model development is an involved process, as is model validation. Models developed for system stability studies also need to be able to reproduce events on a timescale ranging from milliseconds to tens of seconds. Existing models are proprietary and manufacturer-specific, and are bound by the manufacturer’s non-disclosure agreements. They are usually positive-sequence models, and hence, cannot model unbalanced faults. In addition, they are usually not detailed; they often model the generator alone, and do not model aerodynamics and mechanics of the wind turbine and generator. Most models are also not validated using real data. The need for robust generic wind turbine and wind power plant models has been the motivation behind the research described here.

## 1.2 Research Objectives

Proprietary and manufacturer-specific models of wind turbines are typically favored for use in wind power interconnection studies. While they are detailed and accurate, their usages are limited to the terms of non-disclosure agreement, thus stifling model sharing. The primary objective of the work described herein was to develop universal manufacturer-independent wind turbine and wind power plant models that can be shared, used, and improved without any restrictions by project developers, manufacturers, and engineers. The emphasis is on development and validation of standardized “textbook models,” similar to those for other power system apparatus. In addition to the primary objective, the secondary objective was to use these models to perform many other studies such as on inertial response of wind turbines during a unit trip on the grid, and to model controls which allow wind turbines to provide inertial support under such conditions. The salient features of these models are:

- They are generic and manufacturer-independent models;
- Selected models have been validated with real data;
- They are detailed analytical models intended for power system stability studies;
- They are three-phase, time-domain models implemented in PSCAD/EMTDC but portable to other modeling software, and can model balanced and unbalanced faults, frequency excursions and other dynamic events;
- They can successfully represent the diversity of wind turbine technologies currently in use;
- They can model fast and slow phenomena: electromagnetic transients (1ms) to system-wide controls (50s);
- They are scalable (from single turbine to large wind power plant);
- They are comprehensive:
  - They can model wind behavior (wind ramps/gusts etc.);
  - They include basic wind turbine aerodynamic characteristics;
  - They include basic wind turbine mechanical characteristics;
  - They include generator and power electronic converters (if present);
  - They include controls for mechanical and electrical systems;
  - They include collector system (interface to grid) of wind power plant.

Some of the above features, while desirable, also have associated tradeoffs. Generic models will always be approximate, and can be relied on for good estimates rather than precision. They do however have the advantage that they do not need large datasets for validation. Also, three-phase time-domain models are computationally intensive and require more time and computing power than frequency-domain models. However they do provide greater detail in short time scales. Allowing scalability of models from single wind turbines to large wind power

plants has some drawbacks; namely, that the wind power plant’s collector system, i.e., the dispersed electrical equipment necessary for collecting the wind power plant’s output power and feeding it into the grid needs to be reduced to a single-line representation. One of the complicating factors in this work was the diversity of wind power technologies in use. This was overcome by classification of wind turbines into four basic types based on the WECC classifications (technology differences described in [24] and [25]), and modeling each of these types separately.

### 1.3 Wind Turbine Technologies

#### 1.3.1 Modern utility-scale wind turbines

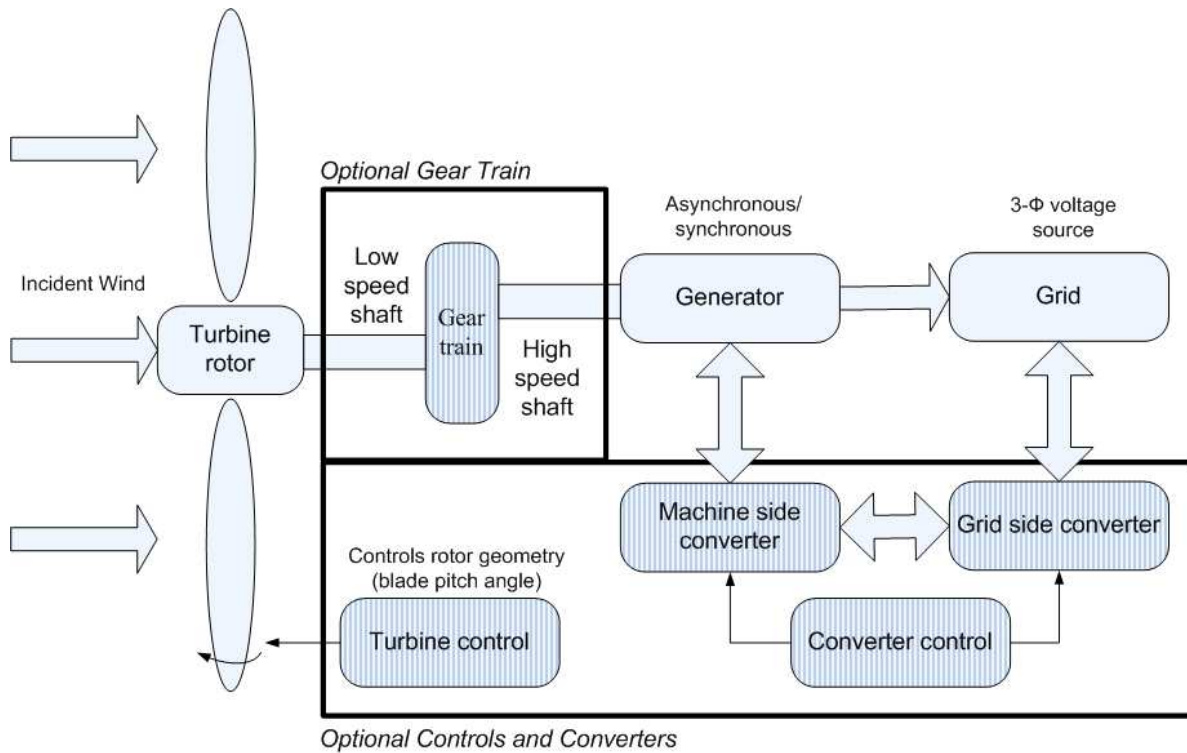


Figure 1.1: Modern wind turbine diagram.

The dominant technology for utility-scale applications is the horizontal axis wind turbine. Typical ratings range from 500 kW to 5 MW. It must be noted that the power output is inherently fluctuating and non-dispatchable. A typical wind turbine consists of the following subsystems (a block diagram is provided in Figure 1.1):

- Rotor (consists of blades and hub)
- Drive-train (shafts, gearbox, couplings, mechanical brake, and electrical generator)
- Nacelle and main-frame (housing, bedplate, and yaw system)
- Tower and foundation
- Electrical system (cables, switchgear, transformers, and power electronic converters if present)

#### 1.3.2 Classification of wind turbines

A wide variety of wind turbine technologies are in use today. Typical wind power plants consist of hundreds of turbines, usually all employing the same technology. A summary of these technologies is presented in [26] and in [27]. These technologies vary in cost, complexity, efficiency of wind power extraction, and equipment used. A

typical wind turbine employs a blade and hub rotor assembly to extract power from the wind, a gear-train to step up the shaft speed at the slowly-spinning rotor to the higher speeds needed to drive the generator, and an induction generator as an electromechanical energy conversion device. Induction machines are popular as generating units due to their asynchronous nature, since maintaining a constant synchronous speed in order to use a synchronous generator is difficult due to variable nature of wind speed. Power electronic converters may be used to regulate the real and reactive power output of the turbine. In [24, 25], wind turbines have been classified into four basic types:

- Type 1: Fixed-speed wind turbines
- Type 2: Variable-slip wind turbines
- Type 3: Doubly-fed induction generator (DFIG) wind turbines
- Type 4: Full-converter wind turbines

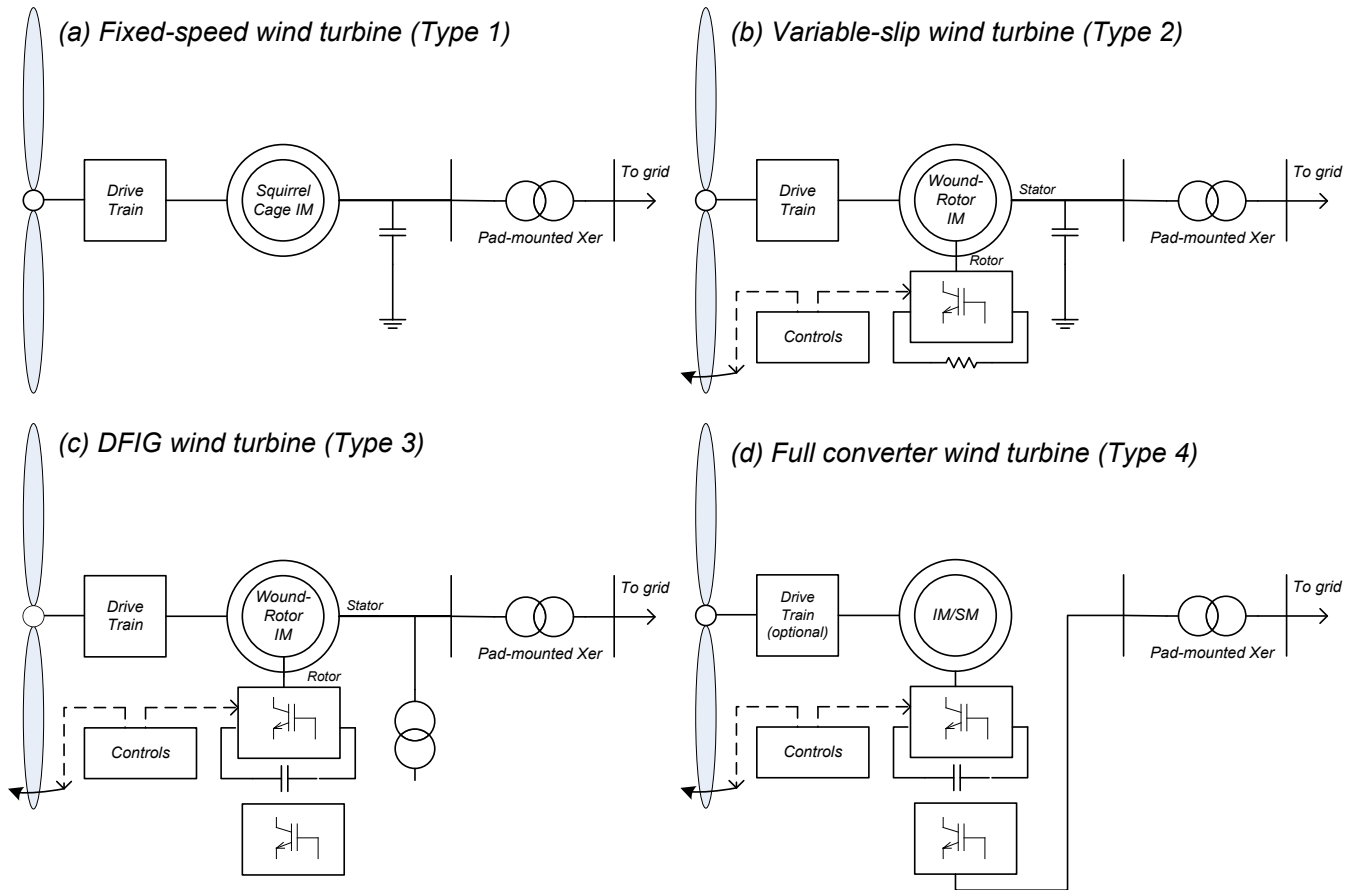


Figure 1.2: Dominant wind turbine technologies.

Fixed-speed wind turbines are the most basic utility-scale wind turbines in operation. They operate with very little variation in turbine rotor speed, and employ squirrel-cage induction machines (IM) directly connected to the grid. Some of these turbines do not have blade-pitching capability. Although relatively robust and reliable, there are significant disadvantages of this technology, namely that energy capture from the wind is sub-optimal and reactive power compensation is required. Variable-speed wind turbines (the broad category into which the other three dominant technologies fall) are designed to operate at a wide range of rotor speeds. These turbines usually employ blade-pitching. Speed and power controls allow these turbines to extract more energy from a given wind regime than fixed-speed turbines can. Variable-slip (VS) or dynamic rotor resistance (DRR) turbines control the resistance in the rotor circuit of the machine to allow a wide range of operating slip (speed) variation (up to 10%). However, power is lost as heat in the rotor resistance. Doubly-fed induction generator (DFIG) turbines remedy

this problem by employing a back-to-back AC/DC/AC converter in the rotor circuit to recover the slip power. Flux-vector control of rotor currents allows decoupled real and reactive power output, as well as maximized wind power extraction and lowering of mechanical stresses. Since the converter is only handling the power in the rotor circuit, it does not need to be rated at the machine's full output. In full converter turbines, a back-to-back AC/DC/AC converter is the only power flow path from the wind turbine to the grid. There is no direct connection to the grid. These turbines may employ synchronous or induction generators and offer independent real and reactive power control. In the full-converter turbine model described in this report, a permanent magnet alternator (PMA) machine with full converter is simulated. Block diagrams for the four models are shown in Figure 1.2. Modeling of each of these types is described in detail in the following chapters.

## 1.4 Contributions

The work featured here fits into the broader theme of developing standardized wind turbine dynamic models. The main contribution of this research is the development of reliable time-domain three-phase wind turbine models of four different basic types for evaluating stability impacts of wind integration on the grid. These models are physics-based, generic, and manufacturer-independent, and have been developed with an approach emphasizing accuracy, detail, and consistency across model types rather than simulation efficiency. The models are modifiable and open, and have no restrictions governing their use. These models exceed the requirements of typical models used in stability studies and offer high resolution and detail in short timescales. Typical models used in power system studies are positive-sequence models and are not suitable to study unbalanced faults which are the majority of fault events on the power system. Preliminary work on modeling of induction generators has been reported in [28]. Modeling of Type 1 and Type 2 turbines has been reported in [29]. Work on Type 3 turbines has been documented in [30] and [31], and work on Type 4 turbines has been documented in [32] and [33]. An overview of the modeling techniques used is presented in [34,35]. The secondary contributions emerging from this research are:

- Evaluation of dynamic response of each of the four different basic types of wind turbine has been performed, and the results indicate that each type of wind turbine differs widely from the others in terms of response to events in the transient and dynamic timescales.
- For DFIG (Type 3) turbines, a way of representing the entire wind power plant as a unified current source, and an “equivalencing” technique, previously used in steady-state models, for reducing wind power plant collector systems to a single-line representation has been tested and evaluated for dynamic models. The DFIG model has also been validated using real data [30, 31].

## 1.5 Brief Summary

In this report, chapter 2 deals with fixed-speed (Type 1) wind turbine modeling and chapter 3 deals with variable-slip (Type 2) wind turbine modeling. Chapter 4 describes the modeling of a DFIG wind power plant as a single unified current source and also describes the model's validation. Chapter 5 also describes DFIG turbine modeling, specifically a single-machine detailed model. Chapter 6 describes a full-converter wind turbine model employing a permanent magnet alternator (PMA). Each of these chapters provides details on model structure, model components, model development, model testing, and dynamic response.

## 2. Modeling of Fixed-Speed (Type 1) Wind Turbine Generators

### 2.1 Introduction to Wind Turbine Modeling

This chapter describes the development of a generic dynamic model for a fixed-speed wind turbine, the most basic type of utility-scale wind turbine in operation today. Fixed-speed wind turbines are called so because they operate with less than 1% variation in rotor speed. They employ squirrel-cage induction machines directly connected to the power grid. They usually employ pitch control to control power extracted from the wind, though they may also employ stall control. Typically in pitch-controlled turbines, the blades are not rigidly fixed to the hub, and can be rotated a few degrees to turn them out of or into the wind. In stall-controlled turbines, the rotor blades are fixed to the hub, and are designed so that the air flow over the blades changes from streamlined (i.e., laminar) flow to turbulent flow at high wind speeds. This limits the mechanical power extracted from the wind at high wind speeds in order to protect the induction machine from overloads. A side effect of stall regulation is that energy capture from the wind is sub-optimal. The models described here and in the next chapter employ the stall control method for simplicity.

Variable-speed wind turbines are designed to operate at a wide range of rotor speeds. Their rotor speed varies with the wind speed or other system variables, based on the design employed. Additional speed and power controls allow variable-speed turbines to extract more energy from a wind regime than would be possible with fixed-speed turbines. For Type-3 and Type-4 turbines, power converters are needed to interface the wind turbine and the grid. The advantage of converter-based systems is that they allow independent real and reactive power control.

Fixed-speed wind turbines are low-cost, robust, reliable, simple to maintain, and proven in the field [20]. A large number of fixed-speed wind turbines have been installed over the past decade and a half, and more continue to be installed. While variable-speed wind turbines form the bulk of new installed capacity, a niche for fixed-speed wind turbines still exists. Therefore, it can be expected that fixed-speed wind turbines will continue to play a role in the power systems of the future.

While there are many wind turbine dynamic models available in the literature [19, 36–39], the focus is largely on modeling variable-speed wind turbines. These models often oversimplify the mechanical drive train and aerodynamics, since the aim is to evaluate power and rotor speed control mechanisms. Thus, there exists a gap in the literature which the model described in this chapter attempts to address. While the model's central purpose is to study the interaction between the wind turbine and the power system, it may also be used to examine the interaction of aerodynamic, mechanical, and electrical functions within the wind turbine. This model is a platform on which more advanced variable-speed wind turbine models can be developed. The complete model has been implemented in PSCAD/EMTDC for the purposes of this report. However, the model is straightforward to implement using other popular simulation packages such as MATLAB/SIMULINK. The model is based on parameters from an NEG Micon 1.5-MW turbine (specifications provided in Appendix A).

Wind turbines are designed to capture the kinetic energy present in wind and convert it to electrical energy. An analogy can be drawn between wind turbines and conventional generating units which harness the kinetic energy of steam. From a modeling standpoint, a fixed-speed wind turbine consists of the following components:

- Turbine rotor and blade assembly (prime mover);
- Shaft and gearbox unit (drivetrain and speed changer);
- Induction generator;
- Control system.

The interaction between each of the components listed above determines how much kinetic energy is extracted from the wind. Figure 2.1 illustrates the interaction between the wind turbine components. Modeling of the

electrical subsystems is fairly straightforward, as power system modeling software usually includes a built-in induction machine model. However, modeling of the aerodynamics and mechanical drivetrain is more challenging. These components are modeled based on the differential and algebraic equations that describe their operation. The following sub-sections describe the modeling of the components listed above.

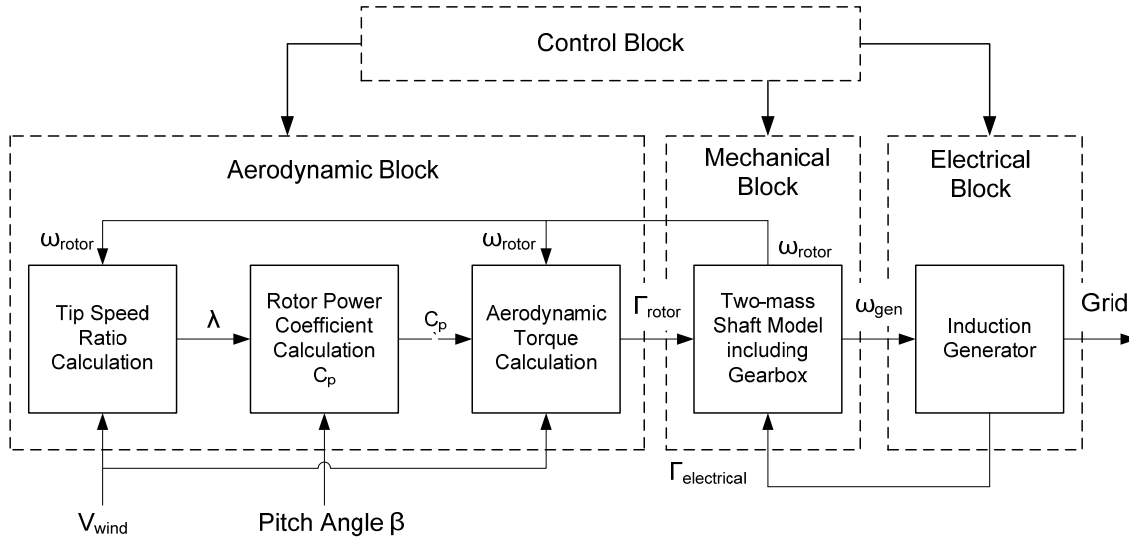


Fig. 2.1. Block diagram for a fixed-speed stall-regulated wind turbine.

## 2.2 Aerodynamics

### 2.2.1 A brief introduction to the aerodynamics of wind turbines

Wind turbine power production depends on interaction between the wind turbine rotor and the wind. The mean power output is determined by the mean wind speed, thus only steady-state aerodynamics have been considered to be important in this project and turbulence has been ignored. The first aerodynamic analyses of wind turbines were carried out by Betz [40] and Glauert [41] in the late 1920s and early 1930s. Power available in the wind is given by:

$$P_{wind} = \frac{1}{2} \rho A V_{wind}^3 \quad (2.1)$$

In the above equation,  $\rho$  is air density,  $A$  is area swept by blades, and  $V_{wind}$  is wind speed. Betz proved that the maximum power extractable by an ideal turbine rotor with infinite blades from wind under ideal conditions is 59.26% (0.5926 times) of the power available in the wind. This limit is known as the Betz limit. In practice, wind turbines are limited to two or three blades due to a combination of structural and economic considerations, and hence, the amount of power they can extract is closer to about 50% (0.5 times) of the available power. The ratio of extractable power to available power is expressed as the rotor power coefficient  $C_p$ . The extractable power can thus be written as:

$$P_{wind} = \frac{1}{2} C_p \rho A V_{wind}^3 \quad (2.2)$$

Modern utility-scale wind turbines use airfoils (shapes similar to an aircraft wing) shown in Figure 2.2 to harness the kinetic energy in the wind. Two wind-induced forces act on the airfoil; lift and drag. Turbines depend predominantly on lift force to apply torque to rotor blades, though some torque is caused by the drag force as well. The lift force is shown perpendicular to effective airflow direction; it is primarily responsible for the torque that rotates the rotor. The tips of the blades, being farthest from the hub, are responsible for the major part of the torque.

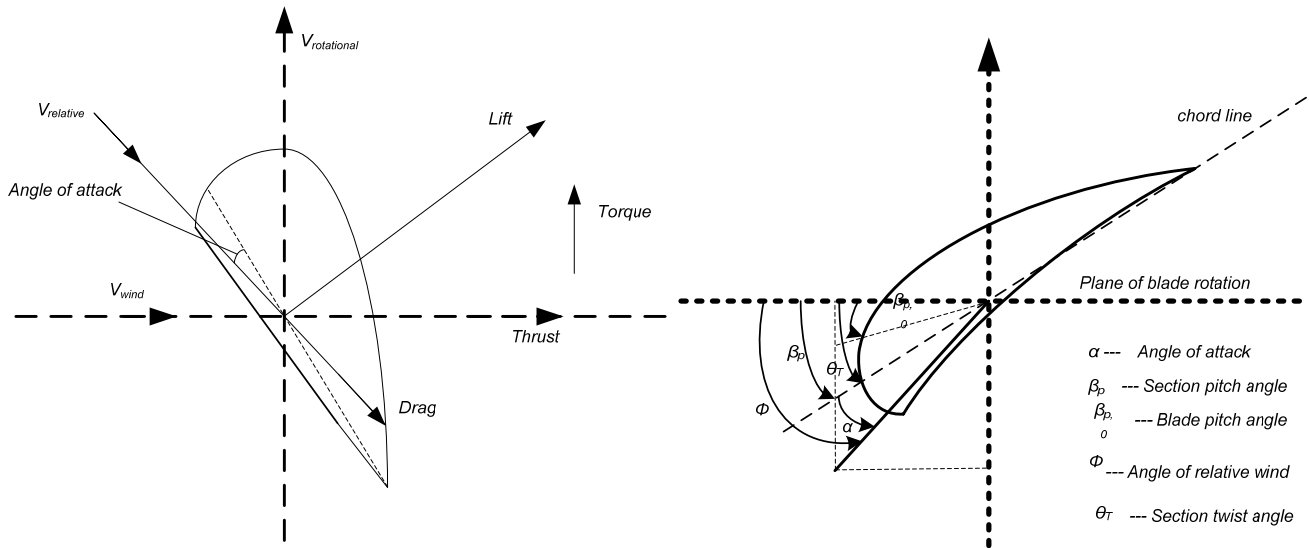


Figure 2.2: Cross section of wind turbine blade airfoil (left) and relevant angles (right).

Depending on the type of turbine, one of two techniques [42] may be used to prevent high wind speeds from causing the wind turbine to operate at higher-than-rated power output. This condition is undesirable because it causes premature wear and tear on the turbine components and reduces the life of the turbine. The first of these is known as stall regulation. In this technique, the wind turbine blades are designed such that when the angle of attack becomes too high (at high wind speeds), a wake forms above the airfoil, aerodynamic lift fails, drag increases, and the net power extracted from the wind falls. The advantages of stall-regulated wind turbines are that they are simple since no extra controllers are necessary. However, there is a considerable disadvantage; power that could have been captured is lost. The alternative strategy is known as blade pitching. In this strategy, a control system changes the angles of the tips of the rotor blades or rotates the entire blade to control the angle of attack and to control extracted power. Pitch-regulated wind turbines can extract more energy from similar wind regimes than non-pitch controlled machines, but require additional controllers and machinery, and increase complexity and cost. Fixed-speed wind turbines may be stall-regulated or they may employ blade pitching.

### 2.2.2 Aerodynamic Block

The aerodynamic block consists of three subsystems: tip-speed ratio calculation, rotor power coefficient ( $C_p$ ) calculation, and aerodynamic torque calculation. Wind speed and pitch angle are user-defined inputs. Since the model is intended to study the dynamic response of wind turbines to grid events, the assumption is usually made that the wind speed stays constant during the grid event. However, this model allows the wind speed input signal to be set to any value at the start of the simulation run-time and also to be modified during the run. It is also possible to use a time-series of actual wind speed data. Since the focus of this chapter is on a fixed-speed stall-regulated wind turbine model, the pitch angle is fixed at the start of the simulation so that the wind turbine achieves rated power at the rated wind speed.

### 2.2.3 Tip-speed ratio calculations

The tip-speed ratio or TSR, denoted by  $\lambda$ , is the ratio of the blade-tip linear speed to the wind speed [42]. The TSR determines the fraction of available power extracted from the wind by the wind turbine rotor. In a fixed-speed wind turbine, the blade tip speed is held relatively constant since the rotor is connected directly to the induction generator via a gearbox, and the induction generator is directly connected to the grid. The TSR can be calculated as follows:

$$\lambda = \frac{\omega_{rotor} \cdot R_{rotor}}{V_{wind}} \quad (2.3)$$

where  $\omega_{rotor}$  = rotor angular speed [rad/s]  
 $R_{rotor}$  = rotor radius [m]  
 $V_{wind}$  = wind speed [m/s]

#### 2.2.4 Rotor power coefficient ( $C_p$ ) calculation

The TSR, together with the user-defined blade pitch angle  $\beta$ , are used to calculate the rotor power coefficient, denoted by  $C_p$ . The rotor power coefficient is a measure of the rotor efficiency and is defined as:

$$C_p = \frac{\text{Extracted power}}{\text{Power in wind}} = \frac{P_{rotor}}{P_{wind}} \quad (2.4)$$

There is a constant value of  $\lambda$  which, if maintained for all wind speeds, will result in an optimal  $C_p$  curve and optimal power extraction from the wind. Variable-speed wind turbines are equipped with a pitch-change mechanism to adjust the blade pitch angle and obtain a better power coefficient profile.

In case of a fixed-speed wind turbine which is directly connected to the grid, the electrical generator speed,  $\omega_{gen}$ , is essentially fixed by the grid frequency. In turn, the rotor speed,  $\omega_{rot}$ , is also fixed since it is directly connected to the generator via a gearbox. As a result, the blade tip speed is practically unchanged. As the wind speed increases, the  $C_p$  of a direct-connect fixed-speed wind turbine will increase at first, achieve an optimal value at rated wind speed (the wind speed corresponding to rated power output), and decrease at higher wind speeds. In the model, a set of generic  $C_p$  curves [43] shown in Figure 2.2 are used to calculate the value of  $C_p$ .

#### 2.2.5 Aerodynamic torque calculation

The aerodynamic torque developed by the rotor blades is calculated in this subsystem using the theory given in [42]. The kinetic energy  $E$  (in J) of an air mass  $m$  (in kg) moving at a speed  $V_{wind}$  (in m/s) is given by:

$$E = \frac{1}{2} m V_{wind}^2 \quad (2.5)$$

If the air density is  $\rho$  (kg/m<sup>3</sup>), mass flow through an area  $A$  is given by:

$$\dot{m} = \rho A V_{wind} \quad (2.6)$$

Thus, an equation for the power (in W) through a cross-sectional area  $A$  normal to the wind is:

$$P_{wind} = \frac{1}{2} \rho A V_{wind}^3 \quad (2.7)$$

In the case of a wind turbine, area  $A$  is the area swept by the rotor blades. Only a part of this power may be captured due to the non-ideal nature of the rotor, hence the need for the coefficient  $C_p$ . The result is shown in Equation 2.8.

$$P_{rotor} = \frac{1}{2} \rho \cdot C_p \cdot \pi R_{rotor}^2 \cdot V_{wind}^3 \quad (2.8)$$

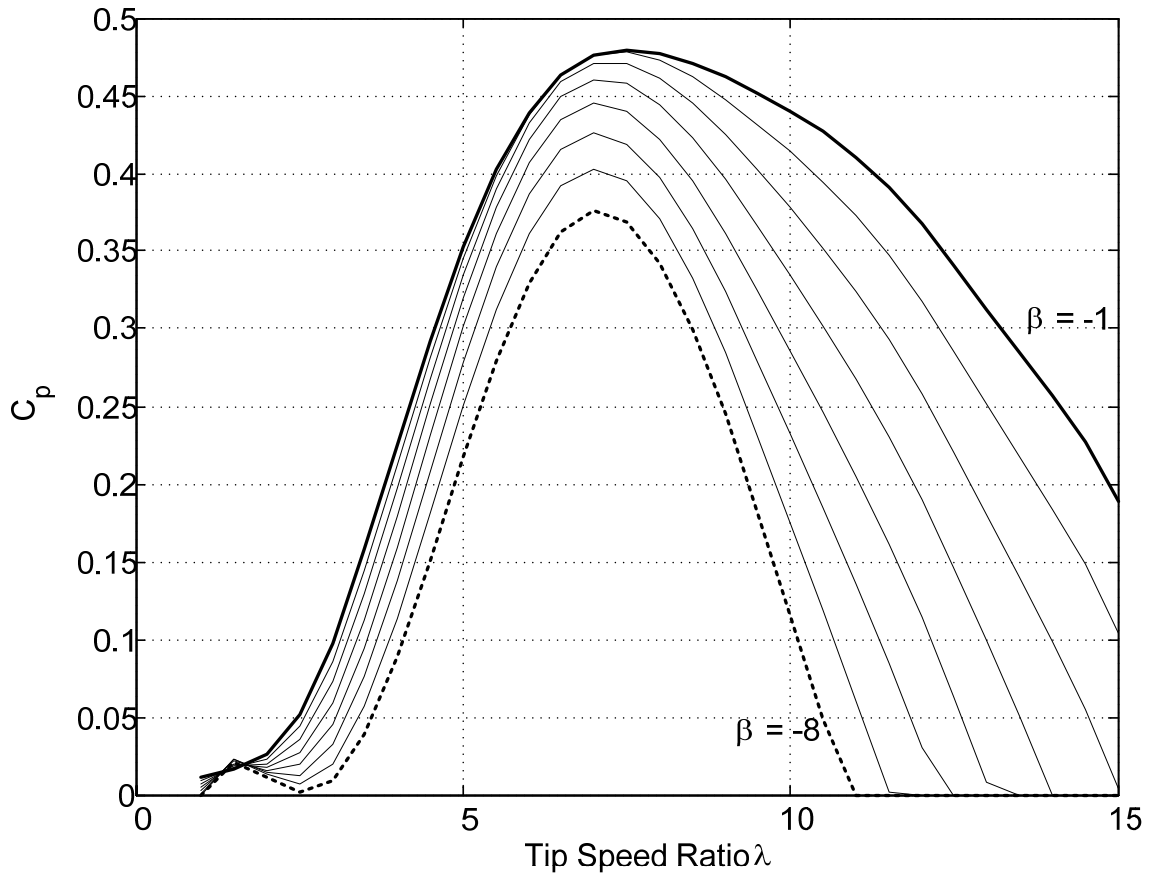


Figure 2.3: Generic  $C_p$  curves for values of pitch ranging from  $-1^\circ$  to  $-8^\circ$ .

The aerodynamic torque developed (in Nm) can then be calculated:

$$\Gamma_{rotor} = \frac{P_{rotor}}{\omega_{rotor}} = \frac{\frac{1}{2} \rho \cdot C_p \cdot \pi R_{rotor}^2 \cdot V_{wind}^3}{\omega_{rotor}} \quad (2.9)$$

### 2.3 Mechanical Drivetrain

The mechanical block consists of the rotor shaft, generator shaft, and a gearbox. The shafts and the gearbox are modelled using a two-mass inertia representation. For a rotational system [44] such as the one shown in Figure 2.3a, consisting of a disk with a moment of inertia  $J$  mounted on a shaft fixed at one end, let us assume that the viscous friction coefficient (damping) is  $D$  and that the shaft torsional spring constant (stiffness) is  $K$ .

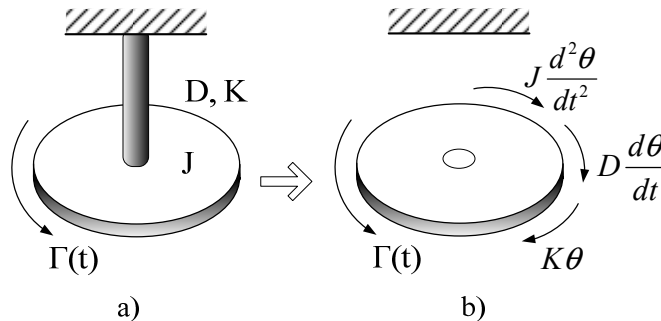


Figure 2.4: Rotational system with a disk.

The torque acting on the disk can be calculated from the free-body diagram of the disk, shown in Figure 2.3b, as follows.

$$\Gamma(t) = J \frac{d^2\theta(t)}{dt^2} + D \frac{d\theta(t)}{dt} + K\theta(t) \quad (2.10)$$

A more complex rotational system, consisting of two such systems, is shown in Figure 2.4a. The two systems are coupled through a gear train, and  $\Gamma$  is the external torque applied to the disk of System 1.  $\Gamma_1, \Gamma_2$  are transmitted torques.  $N_1, N_2$  are the numbers of teeth of Gear 1 and Gear 2.  $J_1, J_2, D_1, D_2, K_1, K_2$  are the moments of inertia, damping, and stiffness of System 1 and System 2, respectively. The system is still time-dependent, but the notation  $t$  is dropped for the sake of clarity.

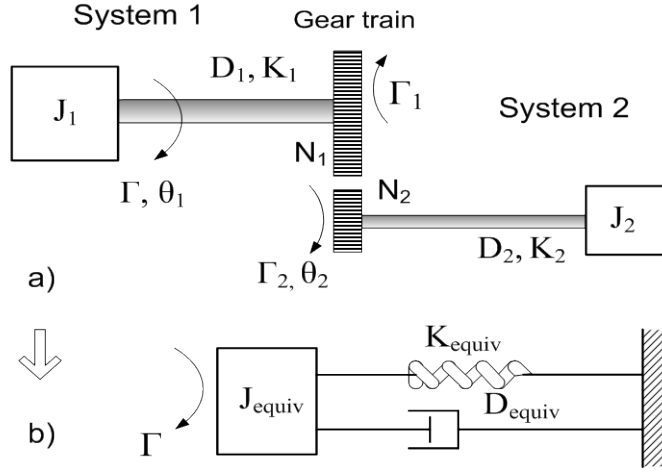


Figure 2.5: Rotational system incorporating a gear train.

Applying Equation 2.10 to the system in Figure 2.4a, the torque equation at  $J_1$  is

$$\Gamma = J_1 \frac{d^2\theta_1}{dt^2} + D_1 \frac{d\theta_1}{dt} + K_1\theta_1 \quad (2.11)$$

The torque equation at  $J_2$  is

$$\Gamma_2 = J_2 \frac{d^2\theta_2}{dt^2} + D_2 \frac{d\theta_2}{dt} + K_2\theta_2 \quad (2.12)$$

Since  $\Gamma_1 = (N_1/N_2)\Gamma_2$  and  $\theta_2 = (N_1/N_2)\theta_1$ , the quantities on Gear 2 side can be referred to the Gear 1 side [44].

$$\Gamma_1 = \left(\frac{N_1}{N_2}\right) \left( J_2 \frac{d^2\theta_2}{dt^2} + D_2 \frac{d\theta_2}{dt} + K_2\theta_2 \right) \quad (2.13)$$

$$\Gamma_1 = \left(\frac{N_1}{N_2}\right) \left[ J_2 \left(\frac{N_1}{N_2}\right) \frac{d^2\theta_1}{dt^2} + D_2 \left(\frac{N_1}{N_2}\right) \frac{d\theta_1}{dt} + K_2 \left(\frac{N_1}{N_2}\right) \theta_1 \right]$$

$$\Gamma_1 = J_{refl} \frac{d^2\theta_1}{dt^2} + D_{refl} \frac{d\theta_1}{dt} + K_{refl}\theta_1 \quad (2.14)$$

where  $J_{refl}$ ,  $D_{refl}$ , and  $K_{refl}$  are the quantities reflected on the Gear 1 side. Substituting Equation 2.14 into Equation 2.11 and rearranging, we obtain Equation 2.15 for the applied torque. The system in Figure 2.4a is reduced to the equivalent system in Figure 2.4b with the gear train eliminated.

$$\Gamma = J_{equiv} \frac{d^2\theta_1}{dt^2} + D_{equiv} \frac{d\theta_1}{dt} + K_{equiv}\theta_1 \quad (2.15)$$

where

$$J_{equiv} = J_1 + J_2 \left(\frac{N_1}{N_2}\right)^2 = J_1 + J_{refl}$$

$$D_{equiv} = D_1 + D_2 \left(\frac{N_1}{N_2}\right)^2 = D_1 + D_{refl}$$

$$K_{equiv} = K_1 + K_2 \left(\frac{N_1}{N_2}\right)^2 = K_1 + K_{refl}$$

The simplified wind turbine configuration shown in Figure 2.5a is similar to the system in Figure 2.4a. The wind turbine drivetrain can therefore be modelled as a two-mass system coupled through a gear train. The quantities on the wind turbine rotor side of the gearbox can be reflected to the generator side. This eliminates the gear ratio and results in a two-mass representation of the wind turbine (Figure 2.5b). Neglecting the effects of the gearbox moment of inertia, damping, and stiffness is justifiable since the moment of inertia of the wind turbine rotor is comparatively very high.

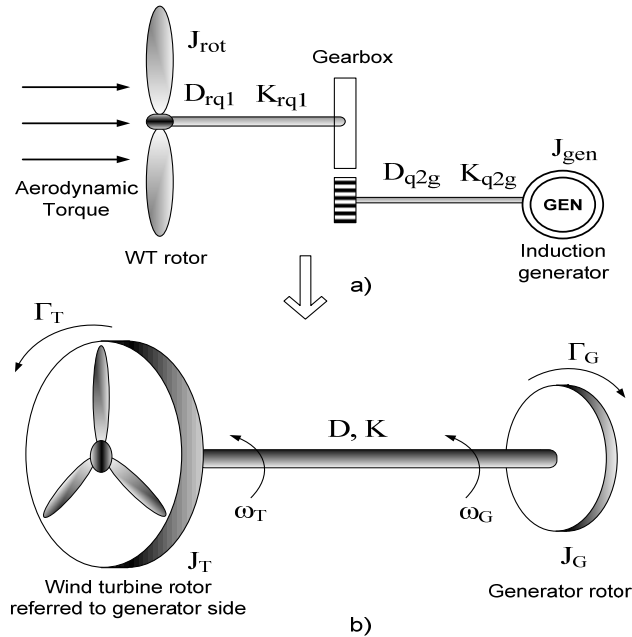


Figure 2.6: Wind turbine drivetrain model.

Torque equations representing the mechanical behaviour of the wind turbine are derived, based on the two-mass model. The aerodynamic torque from the wind turbine rotor and the electromechanical torque from the direct-connect induction generator act in opposition to each other. Torque equations with all quantities referred to the generator side are:

$$J_T \ddot{\theta}_T + D(\omega_T - \omega_G) + K(\theta_T - \theta_G) = \Gamma_T \quad (2.16)$$

$$J_G \ddot{\theta}_G + D(\omega_G - \omega_T) + K(\theta_G - \theta_T) = -\Gamma_G \quad (2.17)$$

where

$$J_T, J_G = \text{moments of inertia of the wind turbine rotor and the generator [kgmm]}$$

$$\Gamma_T, \Gamma_G = \text{wind turbine aerodynamic and generator electromagnetic torque [Nm]}$$

$\omega_T, \omega_G$  = wind turbine rotor and the generator speed [rad/s]  
 $\theta_T, \theta_G$  = angular position of the rotor and the generator [rad]  
 $D, K$  = equivalent damping and stiffness [Nms/rad], [Nm/rad]

Speeds and torques of the turbine rotor and the generator can be determined for each simulation time step by solving Equations 2.16 and 2.17 using a state-space approach. The state-space equations are:

$$\frac{d}{dt}(\theta_G - \theta_T) = (\omega_T - \omega_G) \quad (2.18)$$

$$\dot{\omega}_T = \left(\frac{1}{J_T}\right) [\Gamma_T - D(\omega_T - \omega_G) - K(\theta_T - \theta_G)] \quad (2.19)$$

$$\dot{\omega}_G = \left(\frac{1}{J_G}\right) [D(\omega_T - \omega_G) + K(\theta_T - \theta_G) - \Gamma_G] \quad (2.20)$$

## 2.4 Induction Generator

Most fixed-speed wind turbines employ squirrel-cage induction machines, for which models are readily available in most power system modeling software. The platform of choice to implement the model was PSCAD/EMTDC, and the in-built induction machine model was used. Alternatively, if the modeling platform does not offer a built-in model, users may develop third- or fifth-order algebraic models for induction machines based on the literature available [45]. The rating and parameters of the induction generator used in the model are given in Appendix A. The torque-speed curve of the machine is shown here in Figure 2.7. Note the narrow speed range within which the machine acts as a generator. The fifth- and third-order equations governing the induction machine are provided in Appendix B.

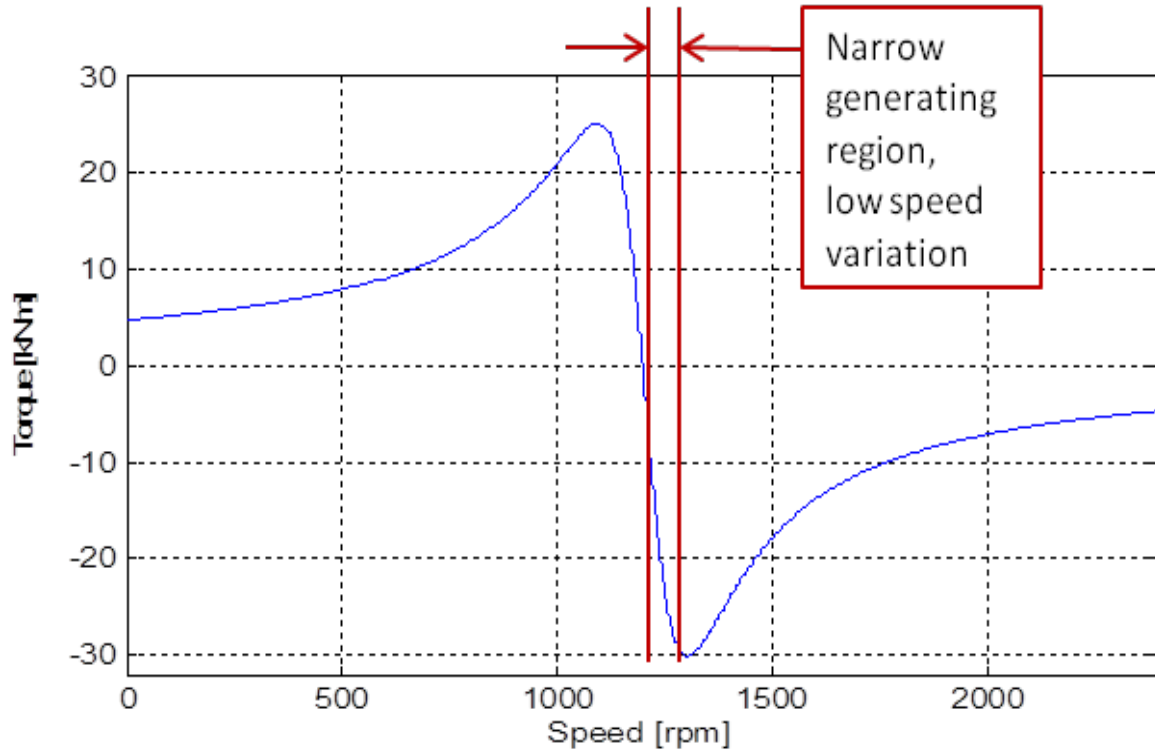


Figure 2.7: Induction machine torque-speed curve (note narrow generating region).

## 2.5 Control Block

Because the focus of the modelling exercise is a fixed-speed wind turbine, pitch-angle control and power control are absent. This block may be added later for modelling variable-speed wind turbines or for reactive power management.

## 2.6 Complete Model Implemented in PSCAD/EMTDC

Figure 2.8 shows the complete model implemented in PSCAD/EMTDC. It is connected to an ideal voltage source (representing the grid) through a step-up transformer. The inputs and outputs for each block and subsystem are shown.

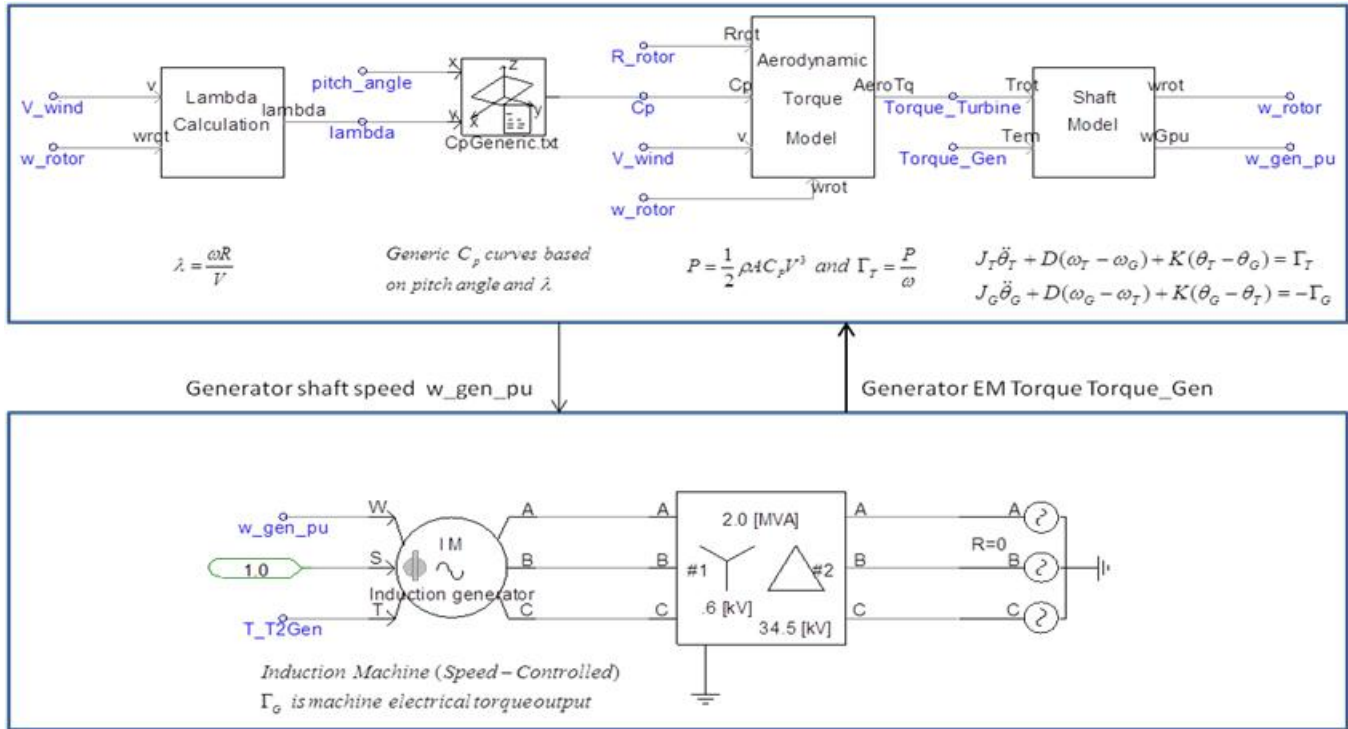


Figure 2.8: Complete model implemented in PSCAD/EMTDC.

## 2.7 Power Curve for Fixed-Speed Model

The most fundamental measure of a wind turbine's performance is given by its power curve. The wind turbine model developed in the previous section is tested by running the simulation at wind speeds from 1 to 20 m/s, with increments of 1 m/s between runs. As expected, the power output peaks at rated wind speed and then falls due to stalling.

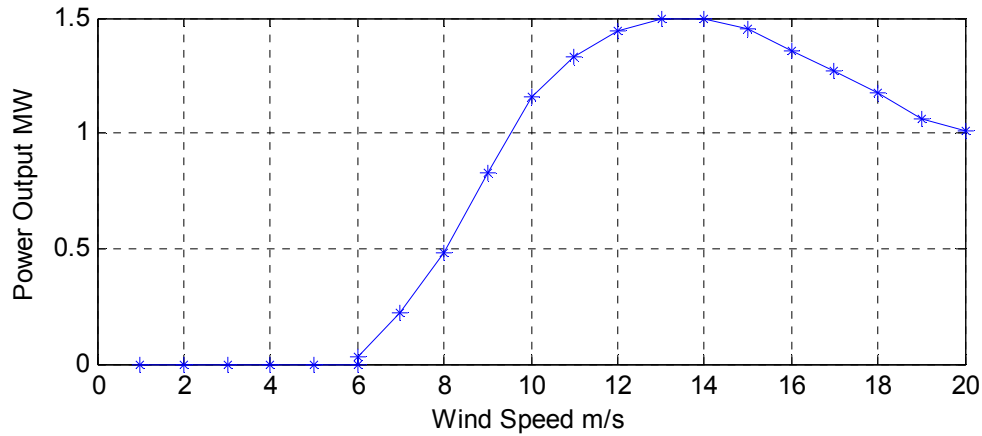


Figure 2.9: Power curve for model.

Table 2.1: Data for power curve.

$V_{wind}$ m/s	$P_{out}$ MW
6	0.03
7	0.22
8	0.484
9	0.825
10	1.159
11	1.332
12	1.441
13	1.5
14	1.5
15	1.452
16	1.359
17	1.267
18	1.171
19	1.063
20	1.007

## 2.8 Dynamic Response

To demonstrate the model's ability to reproduce wind turbine dynamics, a test was created. The wind turbine was operated with a constant wind speed (13 m/s). This wind speed was chosen to be the rated value. A voltage sag on the grid was simulated, and the real and reactive power response of the wind turbine was observed. Note that this is not an implementation of low-voltage ride through (LVRT), but rather a test of dynamic response. The grid voltage drops from 1 p.u. to 0.8 p.u. at  $t=15s$ , and the sag persists for 18 cycles (0.3 seconds). The intent of the test is to show that the model does indeed respond to events occurring in the dynamic timescale and that the response of the machine to this event is realistic. Fig. 2.10 shows the results of the test, and shows that the model does indeed respond to the grid event as expected. The grid voltage, rotor speed, real power, and reactive power during the event are shown. As expected, the step changes in the grid voltage magnitude when the sag begins and ends cause an immediate response. Note that the speed does not change by much (approximately 2%), as expected from a fixed-speed wind turbine. The real power and reactive power outputs experience a disturbance too, and the outputs show that a mechanical oscillation occurs after the sag ends, and that the oscillation eventually damps out.

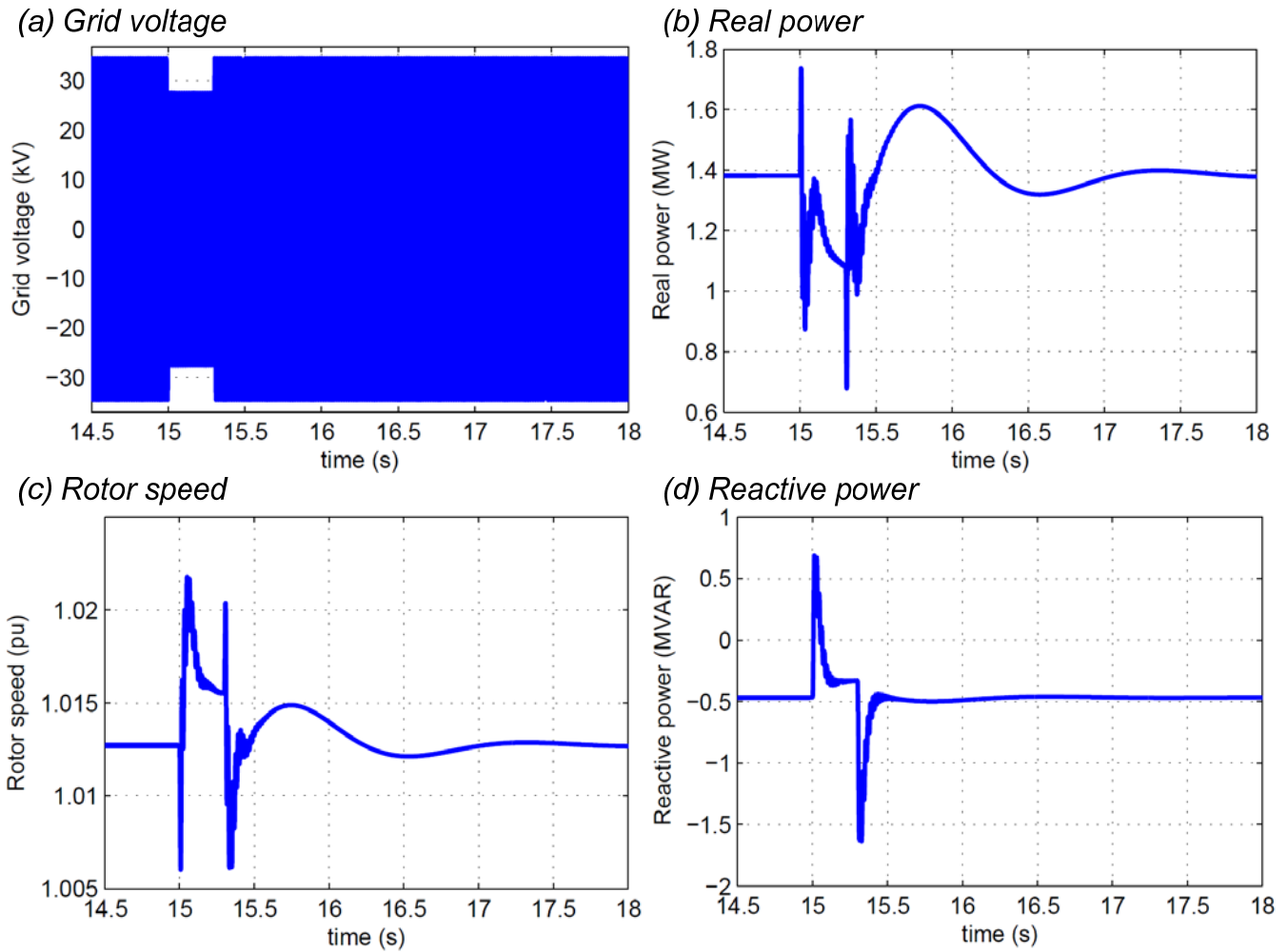


Figure 2.10: Real and reactive power response during voltage sag on the grid.

## 2.9 Summary

In summary, a complete model for a Type-1 fixed-speed wind turbine has been developed and implemented in PSCAD/EMTDC. The model incorporates the aerodynamics, mechanical drivetrain, and electrical systems typically used in such a turbine. Basic performance evaluation of the model has been carried out and a power curve for the turbine has been plotted. Dynamic response of the model has also been evaluated. The model is ready for use in grid integration studies, or as a platform for modeling control schemes for variable-speed operation.

### 3. Modeling of Variable-Slip (Type 2) Wind Turbine Generators

While fixed-speed wind turbines are simple and robust, they have a significant disadvantage: they cannot optimally extract power from the wind. It would be preferable to have the generator continue to output rated power at high wind speeds. To achieve this, variable-speed wind turbines are employed. While largely relying on the same concepts as fixed-speed wind turbines at lower-than-rated wind speeds, they typically incorporate blade pitch and output power controls to optimize power extraction at higher-than-rated wind speeds [46]. The Type-2 turbines which are the focus of this chapter use rotor resistance control to achieve output power control. This chapter discusses the concept of rotor resistance control, its basis in machine theory and the induction machine equivalent circuit, a few methods of achieving optimal power output based on rotor resistance control, the implementation of the control methods using a modified version of the fixed-speed wind turbine model, and provides a discussion of the results obtained from the modified model [47]. Once again, stall regulation is employed rather than pitch regulation in order to focus on the rotor resistance controller action.

#### 3.1 Rotor Resistance Control Concept

Induction machines were invented over a hundred years ago, and are fairly well understood. The basic principle behind their operation is electromagnetic induction. Voltages applied to a multiphase AC stator winding result in currents which produce a rotating magnetic field. This field induces voltages (and therefore currents) in the rotor circuit. The interaction between the stator produced field and the rotor induced currents produces torque. If the induction machine is driven by a prime mover at a speed greater than its synchronous speed, it acts as a generator. The rotor circuit may consist of bars short-circuited through end rings in the case of squirrel cage machines, or in the case of wound-rotor machines, multiphase windings accessible through slip rings and brushes. In this chapter, we are concerned only with wound-rotor machines. Since the rotor windings are accessible, modifications to the rotor circuit are possible. One of these possible modifications is changing the rotor resistance. Revisiting the induction machine equivalent circuit is necessary to evaluate the impact of changing the rotor resistance on the torque and power associated with the machine.

##### 3.1.1 Induction machine equivalent circuit

The equivalent circuit in steady state for an induction machine is shown in Figure 3.1. It is similar to that of a transformer. The equivalent circuit for only one phase is shown since in steady state, all three phases are balanced and thus the equivalent circuit is identical.  $R_1$  and  $X_1$  are the stator series resistance and reactance, respectively, while  $X_m$  is the magnetizing reactance. The rotor resistance  $R_r$  and reactance  $X_r$  can be referred to the stator side using the ideal transformer's turns ratio with  $R_2$  and  $X_2$  representing the referred quantities. This eliminates the transformer. The resulting circuit is shown in Figure 3.2. Here  $s$  refers to the slip. The rotor windings are shorted, i.e. no external resistance is present.

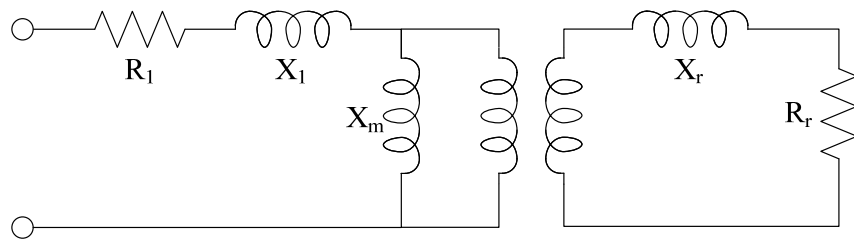


Figure 3.1: Induction machine equivalent circuit.

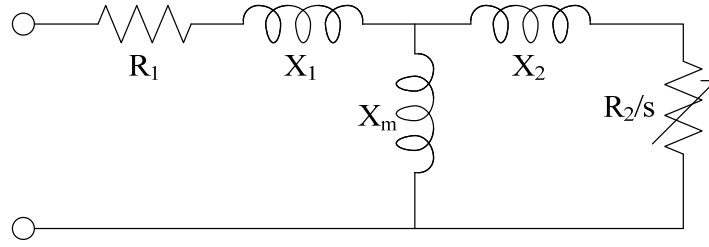


Figure 3.2: Equivalent circuit with all quantities referred to stator.

Based on the equivalent circuit, we can construct a Thevenin equivalent model, from which the following equations for air gap power and torque may be derived [48]:

$$P_{\text{airgap}} = 3V_{TH}^2 \frac{R_2}{s} \frac{1}{\left(R_{TH} + \frac{R_2}{s}\right)^2 + (X_{TH} + X_2)^2} \quad (3.1)$$

$$\Gamma = \frac{P_{\text{airgap}}}{\omega_s} = 3V_{TH}^2 \frac{R_2}{\omega_s s} \frac{1}{\left(R_{TH} + \frac{R_2}{s}\right)^2 + (X_{TH} + X_2)^2} \quad (3.2)$$

where:

$$V_{TH} = \frac{jX_m}{R_1 + j(X_1 + X_m)}$$

$$R_{TH} = \text{Re}(Z_{TH}) = \text{Re}\left(\frac{jX_m(R_1 + jX_1)}{R_1 + j(X_1 + X_m)}\right)$$

$$X_{TH} = \text{Im}(Z_{TH}) = \text{Im}\left(\frac{jX_m(R_1 + jX_1)}{R_1 + j(X_1 + X_m)}\right)$$

Here  $V_{TH}$  is the Thevenin-equivalent voltage at the equivalent circuit terminals, and  $R_{TH}$  and  $X_{TH}$  are Thevenin-equivalent resistance and reactance respectively. Slip  $s$  varies from 1 at zero rpm, to 0 at synchronous speed. A plot of the induction machine torque as a function of speed (and slip) is shown in Figure 3.3.

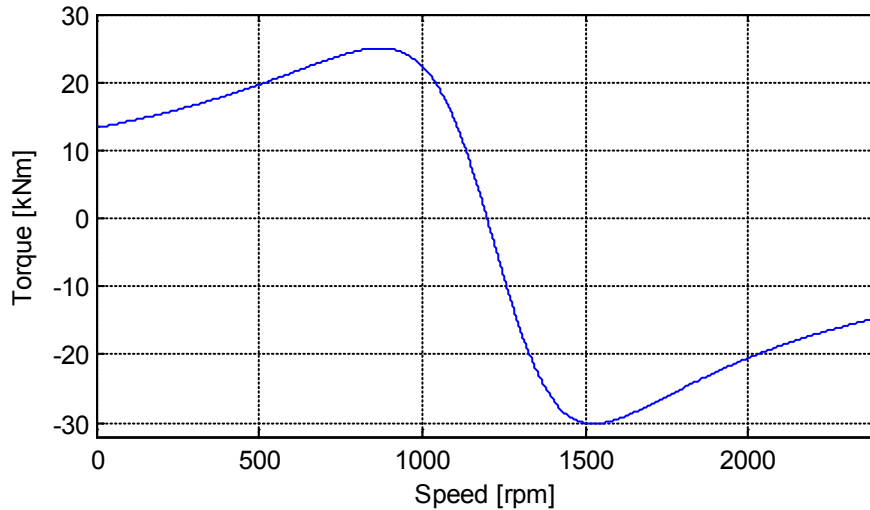


Figure 3.3: Induction machine torque-speed curve.

### 3.1.2 Effect of rotor resistance change on equivalent circuit and torque and power equations

So far external resistance has not been considered, i.e., the rotor windings have been assumed to be shorted. With the external resistance also included, the circuit is as shown in Figure 3.4.

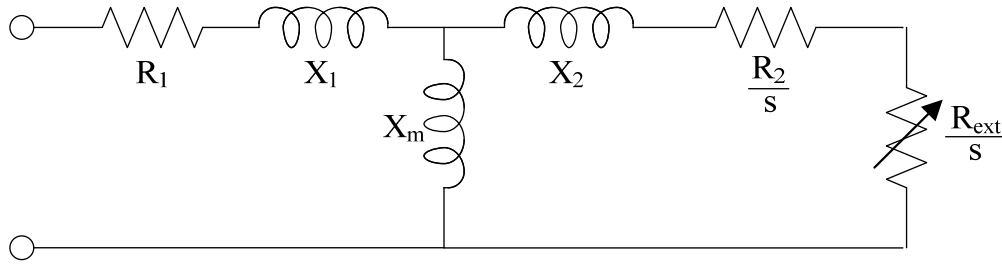


Figure 3.4: Equivalent circuit with  $R_{ext}$  included

A resistor in each phase is required since the equivalent circuit represents one phase of a balanced three-phase circuit. Due to the transformer turns ratio, the value of  $R_{ext}$  in Figure 3.4 will not necessarily be equal to the actual resistance value used to implement the external rotor resistance. The power and torque equations are modified as follows:

$$P_{\text{airgap}} = 3V_{TH}^2 \frac{R_2 + R_{ext}}{s} \frac{1}{\left(R_{TH} + \frac{R_2 + R_{ext}}{s}\right)^2 + (X_{TH} + X_2)^2} \quad (3.1)$$

$$\Gamma = \frac{P_{\text{airgap}}}{\omega_s} = 3V_{TH}^2 \frac{R_2 + R_{ext}}{\omega_s s} \frac{1}{\left(R_{TH} + \frac{R_2 + R_{ext}}{s}\right)^2 + (X_{TH} + X_2)^2} \quad (3.2)$$

The variation in the torque-speed curve of the machine with variation in  $R_{ext}$  is shown in Figure 3.5. A desired value of torque can thus be achieved at many different speeds, by varying the external rotor resistance.

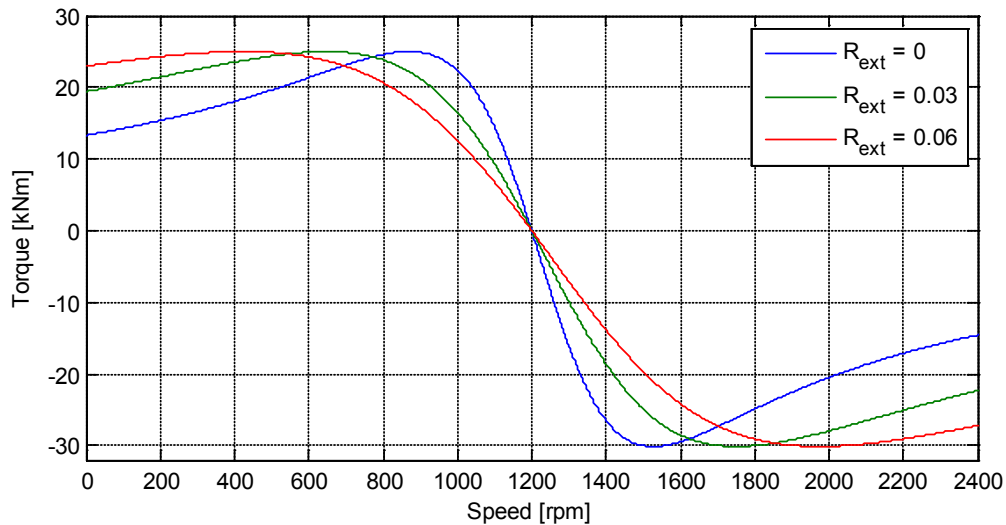


Figure 3.5: Torque-speed curves for different values of  $R_{ext}$ .

For motor operation, it can be seen from Figure 3.5 that higher rotor resistance yields high starting torque, but also causes increased running losses during normal operation, due to power dissipated in the rotor resistance. In a wound rotor induction machine, an external resistance may be inserted into the rotor circuit during starting, and when operating under load, the external resistance can be shorted out, thus achieving both objectives: high starting torque and low running losses. The rotor resistance controller in a variable-speed wind turbine is more complicated, and requires consideration of the aerodynamics. Development and testing of rotor resistance control schemes is discussed in the next section.

### 3.2 Methods for Rotor Resistance Control

As shown in Equation 3.3, control of power output of a Type-2 turbine can be accomplished by varying the rotor resistance. The objective of a rotor resistance controller in this situation is to seek the operating point at which power extraction from the wind is maximized, and also prevent the power extracted from exceeding the machine’s ratings. In this section, changes made to the fixed-speed model (described in the previous chapter) in order to model variable speed operation are described. The basic control method, i.e. PI control, is also briefly covered. The focus is on development and testing of a PI controller for rotor resistance control.

#### 3.2.1 Model implementation

In PSCAD/EMTDC, a wound-rotor induction machine model is available. The same machine parameters as were used for the fixed-speed machine are used here, with some small modifications (see Appendix A). The machine model is shown in Figure 3.6. The internal rotor resistance is “pulled out” and shown explicitly on the rotor circuit, in series with the controlled external resistances.

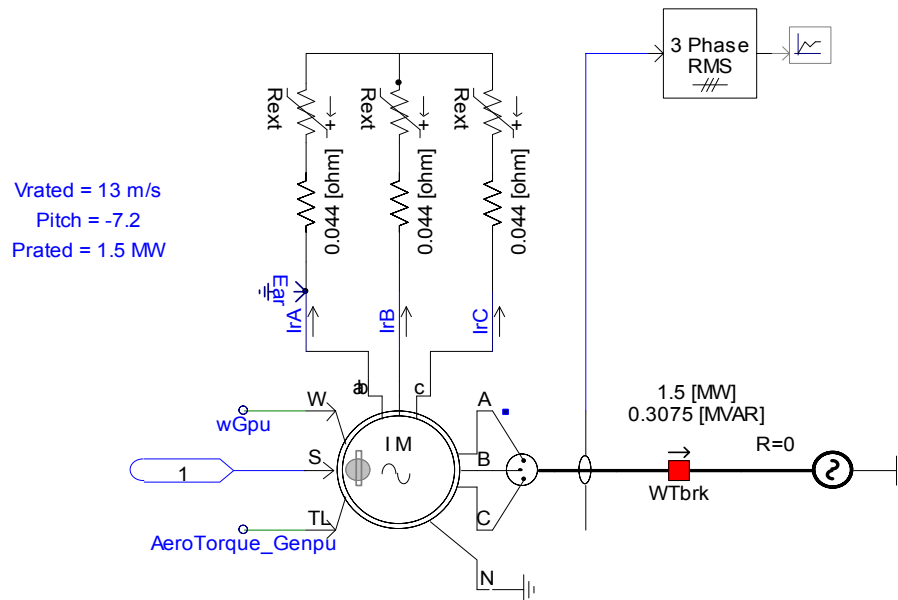


Figure 3.6: Wound-rotor induction machine in PSCAD/EMTDC.

Another modification to the fixed-speed model is the inclusion of a control block for external resistance control. This control block employs Proportional-Integral or PI controllers. PI controllers are standard for wind turbine control. A PI controller attempts to minimize the error between a measured process variable and a desired reference value by calculating and outputting a control action that can adjust the process in a rapid manner to keep the error minimal. In practice, this takes the shape of a feedback loop as shown in Figure 3.7. By tuning the proportional and integral gains, the speed of response of the controller and the magnitude of the overshoot can be chosen appropriately for the desired control action. Tuning of PI controllers is fairly straightforward [44]. The difference between the control methods lies in the choice of measured process variable for generating the error

signal. The controller described here is similar to that employed by real-world turbines. The controller action is based on two measured quantities; output real power (primary) and rotor currents (secondary). The controller employs two loops; an outer loop for real power control which is a relatively slow-changing quantity and an inner loop which reads the output of outer loop controller as set-point, and controls the rapidly changing rotor currents. The measured power signal is compared to the desired power, and the error drives a PI controller. The output of the PI controller is the reference rotor current. This reference current is compared with the measured rotor current and the error is fed to another PI controller. The output of this PI controller is the rotor resistance value for achieving desired rotor current (and thus output power). The two-loop controller is shown in Figure 3.8.

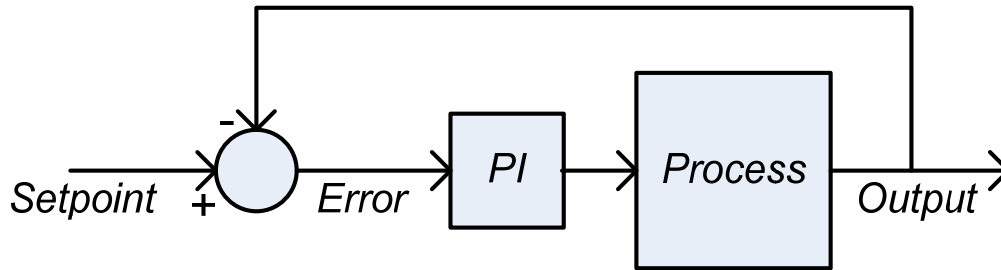


Figure 3.7: Generic PI controller

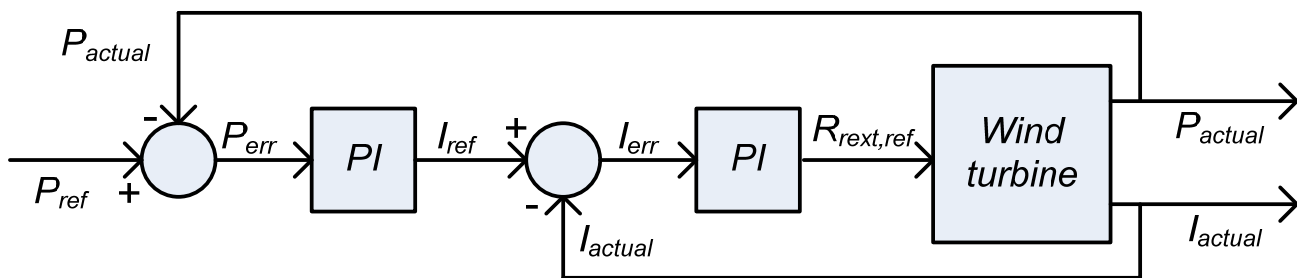


Figure 3.8: Two-loop PI controller for constant rotor current control (inner loop) and real power control (outer loop).

### 3.2.2 Two-loop PI controller based on output power and rotor current

The most straightforward way of controlling the output power is to use the measured power value as the process variable for comparison. The rotor resistance controller implementation is shown in Figure 3.9. A reference power signal is generated by measuring the machine slip, and using a non-linear characteristic (shown in the Figure 3.10) to find the desired value of power for that value of slip. This reference power value is compared with the measured power and the error signal is fed to the PI control. The output of the PI controller is the reference rotor current (rms) that is necessary to achieve the reference output power. This reference current is compared with the actual measured rotor currents (rms), and the error between them drives a second PI controller. The output of this second PI controller is the external rotor resistance required to maintain the rotor currents (and thus the generator power output) at its rated value. The power controller is inactive when the wind speed is below the rated wind speed. It only becomes active when wind speed exceeds rated wind speed. This is due to the disabling of the pitch controller for the purpose of simplicity.

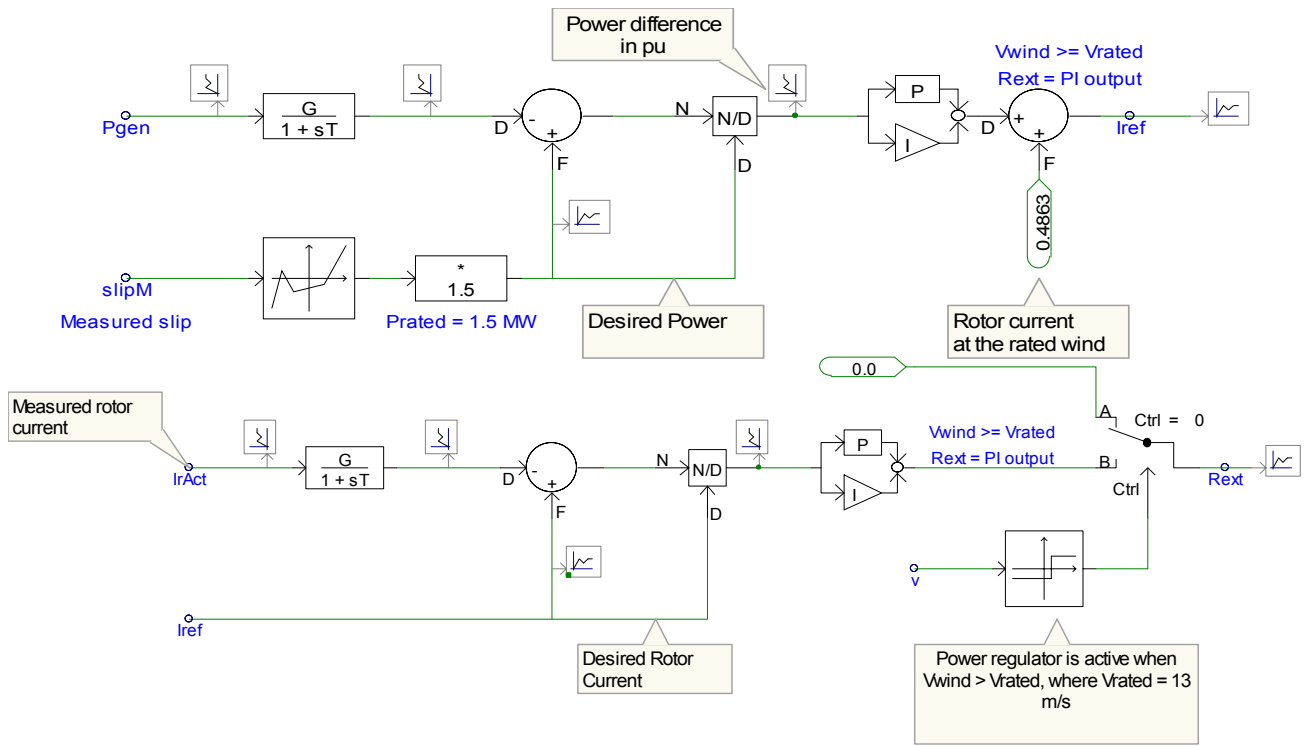


Figure 3.9: PI controller based on output power.

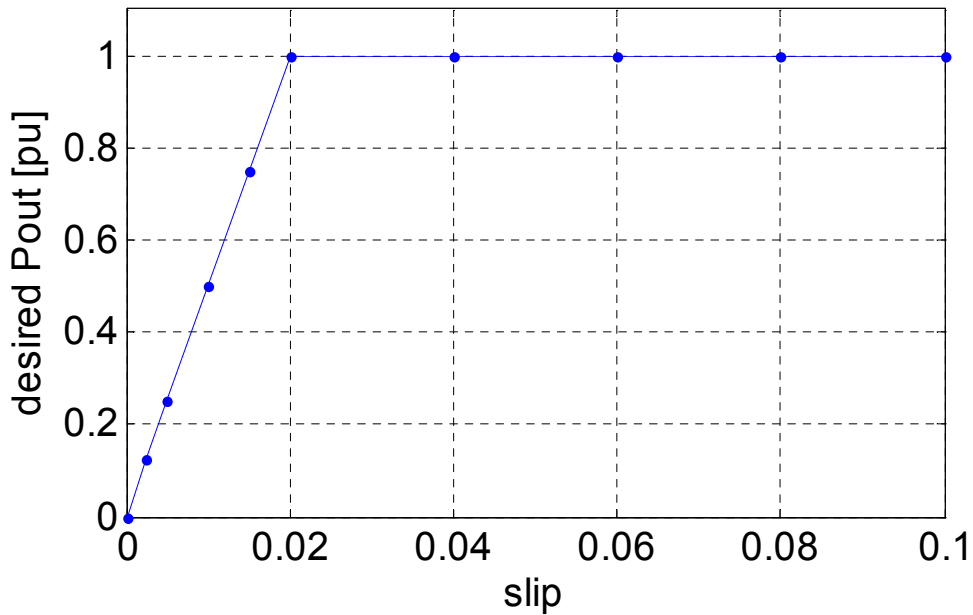


Figure 3.10: Desired output power characteristic.

The power curve of the wind turbine can be plotted (Figure 3.11). The curve is flat at wind speeds higher than rated, as was desired. The results are shown in tabular form in Table 3.1. By comparison, the curve for the fixed-speed wind turbine shown in Figure 2.9 droops at higher-than-rated wind speeds. The results show that a PI controller using measured power and rotor currents as the input variables is a credible solution for maintaining rated power at higher than rated wind speeds.

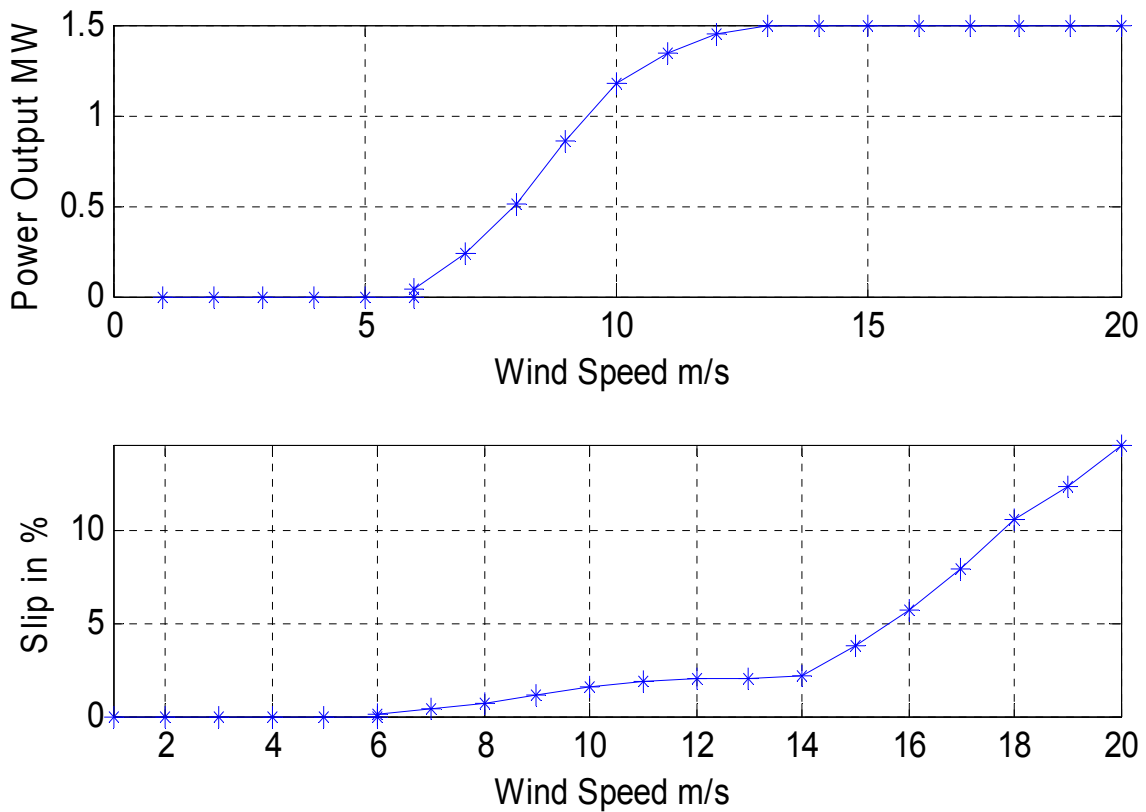


Figure 3.11: Power curve and variation of slip with wind speed.

Table 3.1: Data for power curve, slip, rotor resistance, speed, and torque.

$V_{wind}$	$P_{out}$	$Slip$	$R_{ext}$
m/s	MW	% (neg)	Ohms
6	0.035	0.06	0
7	0.231	0.329	0
8	0.503	0.7	0
9	0.852	1.175	0
10	1.179	1.619	0
11	1.342	1.839	0
12	1.447	1.982	0
13	1.5	2.05	0
14	1.5	2.19	0.00285
15	1.5	3.76	0.0358
16	1.5	5.65	0.0734
17	1.5	7.98	0.12468
18	1.5	10.52	0.17533
19	1.5	12.394	0.21214
20	1.5	14.63	0.257

### 3.3 Dynamic Response

To demonstrate the model's ability to reproduce wind turbine dynamics, a test was created. The wind turbine was operated with a constant wind speed (13 m/s). This wind speed was chosen to be the rated value. A voltage sag on the grid was simulated, and the real and reactive power response of the wind turbine was observed. Note that this is not an implementation of low-voltage ride through (LVRT), but rather a test of dynamic response. The grid voltage drops from 1 p.u. to 0.8 p.u. at  $t=15s$ , and the sag persists for 18 cycles (0.3 seconds). The intent of the

test is to show that the model does indeed respond to events occurring in the dynamic timescale and that the response of the machine to this event is realistic. Fig. 3.12 shows the results of the test, and shows that the model does indeed respond to the grid event as expected. The grid voltage, rotor speed, real power, and reactive power during the event are shown. As expected, the step changes in the grid voltage magnitude when the sag begins and ends cause an immediate response. Note that the speed experiences a greater change (approximately 5%) as compared to the fixed-speed wind turbine in the previous chapter. The real power and reactive power outputs experience a disturbance too, however, the disturbance is once again qualitatively and quantitatively different from the response of the fixed speed wind turbine due to the rotor resistance controller. As in the previous case, the outputs also show that a mechanical oscillation occurs after the sag ends, and that the oscillation eventually damps out.

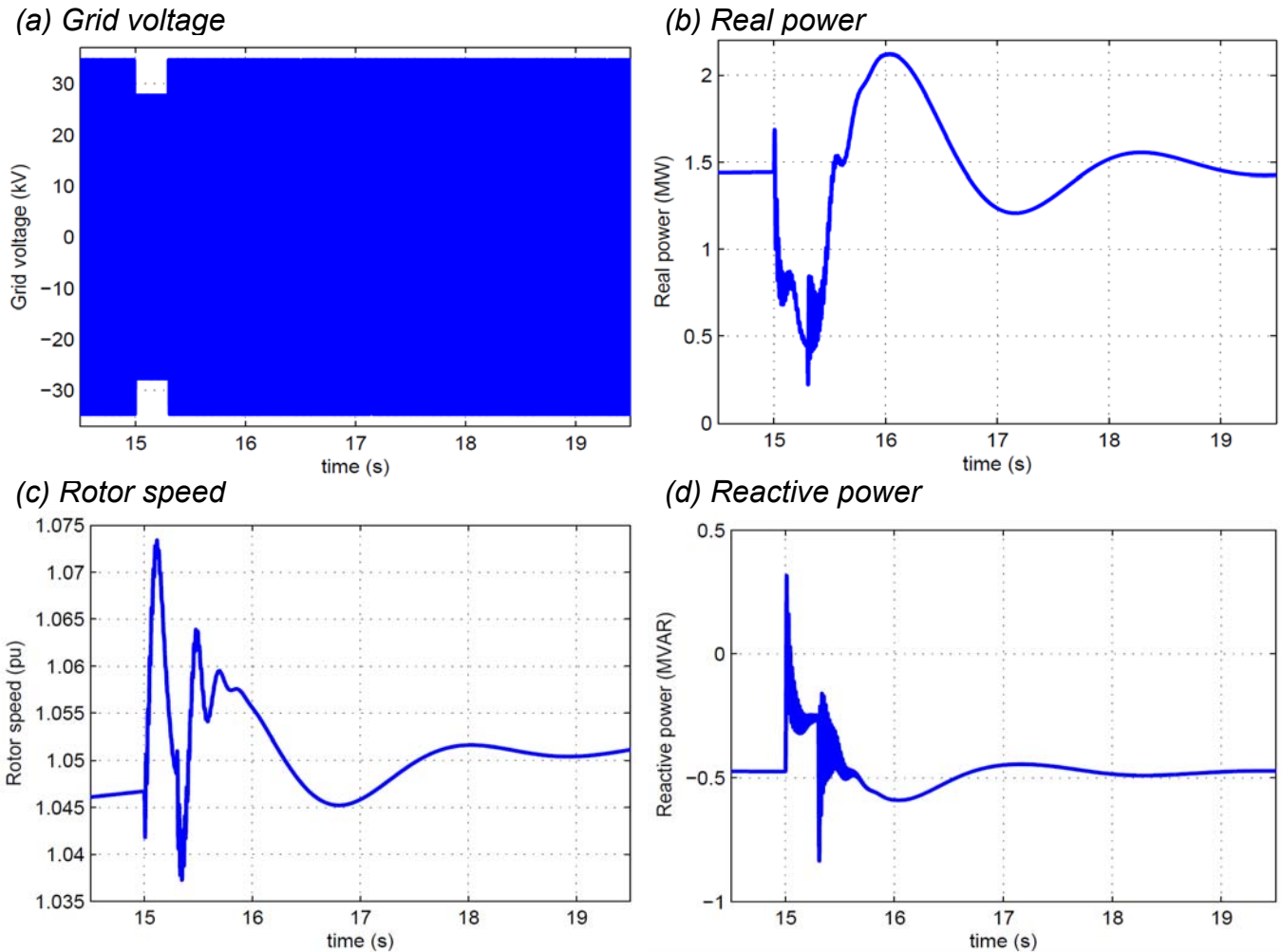


Figure 3.12: Real and reactive power response during voltage sag on the grid.

### 3.4 Summary

In summary, the modeling of a Type-2 variable-speed wind turbine incorporating rotor resistance control has been described. It differs from the fixed-speed model in that a wound-rotor machine with external rotor resistance is used instead of a squirrel-cage machine. A block is added to control the value of rotor resistance. The controller ensures that power extracted from the wind at higher-than rated wind speeds equals the rated power of the machine. A controller based on measured power and currents has been developed, and the dynamic response of the model has also been evaluated.

## 4. Modeling of DFIG (Type 3) Wind Power Plants: Current Source Representation

### 4.1 Introduction to DFIG Technology

This chapter documents the modeling of a generic doubly-fed induction generator (DFIG) for a wind turbine. The model includes simplified aerodynamic representation of the turbine blades, drive-train of the turbine-generator shaft model, generator, and converter. A novel feature of the model is that it represents multiple wind turbine generators as a single equivalent source, i.e., a regulated current source. The source can be sized to the rating of an individual wind turbine, a group of wind turbines, or the entire WPP. A set of three-phase currents is injected into the grid such that the real and reactive power of the generator can be independently controlled. The performance of the generic DFIG model is then evaluated and validated with actual wind power data collected from WPPs having DFIG turbines. The model for the Type-3 wind turbine generator is built using PSCAD/EMTDC software. It is based on the WECC general model, developed by the Wind Generator Modeling Group of the WECC [24].

The modeling procedure detailed in this chapter loosely follows the procedure described in [43]. Wind turbine subsystems are modeled individually and assembled into a complete model. The internals of the two models, however, are considerably different. One of the fundamental differences is that a regulated current source is used to represent the generator and converter in the model described in this chapter. Another feature of the developed model is that it is a three-phase model. There are some advantages of a three-phase model compared to a positive-sequence model, namely, that voltages and currents at points within the model can be used for validation as well as real and reactive power values. Higher-frequency dynamics can be observed. Also, the three-phase model can be easily modified into a positive-sequence dynamic model that can be implemented in available dynamic modeling software packages. The validation of the model against real-world fault data (using current data as well as real and reactive power data) is also described in this chapter. The validation results show that the model is accurate, and addresses the issue of reproducing higher-frequency dynamics.

### 4.2 Prior Work on DFIG Dynamic Modeling

The behavior of DFIG WPPs during faults is well-documented. Dynamic models for DFIG WPPs are presented in [19] and [49]. These models are detailed representations of DFIG WPPs and are not specific to a single turbine manufacturer; however, they have not been validated against real-world WPP fault data. Manufacturer-specific models have been described in [50] and [43], but without validation. Another manufacturer-specific modeling exercise described in [51] includes validation of the model for capacitor switching events. The test events are of long duration (seconds), and it is unclear if the model is able to reproduce shorter-duration dynamics. A validation of the WECC generic model is presented in [24] based on measured field data during fault events. The model described is a positive sequence representation of a three-phase system and while adequate for observing the general trends of real and reactive power output during faults, just as in [51], the higher-frequency perturbations due to the fault event are not reproduced. In both [51] and [24], the only quantities used for validation are the real and reactive power output of the WPP.

#### 4.2.1 Work done under IEA Wind Annex 21

IEA Wind Annex 21 was an international collaboration for WPP modeling and validation [52]. The task undertaken was to characterize the four different types of wind turbines, namely fixed-speed, rotor-resistance control, DFIG and synchronous with full converter, and build dynamic models for each, with suitable validation. The following were listed as “immediate objectives”:

- Establishment of an international forum for exchanging knowledge and experience within the field of wind plant modeling for power system studies.

- Development, description, and validation of wind farm models.
- Set-up and operation of a common database for benchmark testing of wind turbine and wind plant models as an aid for securing good quality models.

The task required the development of models in various software packages [53]. The end result was the establishment of a modeling framework, and strong validation of the models developed. The models built as part of this task had a considerable amount of detail, and while the framework was general, the models themselves were manufacturer-dependent. Part of the research described in this chapter, namely the development of a general model for DFIG WPPs, may be seen as an extension of the work done as part of this task.

### 4.3 Three-Phase Model: Development and Implementation

Doubly-fed induction generators or DFIGs have emerged as the generator technology of choice for modern WPPs. This section provides a description of the DFIG concept and its underlying principles. The development of a time-domain simulation of a DFIG WPP based on these principles is also described.

#### 4.3.1 Doubly-Fed Induction Generators: Basic Concepts

A rotating machine is said to be a generator when it is converting mechanical input power to electrical output power. When induction machines are operated at speeds greater than their synchronous speeds, they act as generators. DFIGs operate on the same principles as conventional wound-rotor induction generators with additional external power electronic circuits on the rotor and stator windings to optimize the wind turbine operation. These circuits help extract and regulate mechanical power from the available wind resource better than would be possible with simpler squirrel-cage induction generators. A schematic representation of a DFIG wind turbine system is shown in Figure 4.1. As wind turbine technology has progressed, turbines have been getting larger in diameter, sweep larger areas, and achieve higher power ratings. This requires longer blades rotating at a slower angular speed to keep the audible noise level within acceptable limits. Therefore, the turbine blades and hub assembly are connected to the generator shaft through a gearbox which steps up the angular speed and interfaces with the induction generator.

In DFIG turbines, the induction generator is a wound-rotor induction machine. Slip-rings and brushes are usually used to access the rotor circuit. The three-phase stator winding is fed directly from the three-phase supply voltage which is typically below 1 kV at the power system frequency (50/60 Hz). A back-to-back AC-DC-AC power electronic converter is used to rectify the supply voltage and convert it to three-phase AC at the desired frequency for rotor excitation. The power converter is connected to the rotor winding to process the slip-power. Thus, unlike a singly-excited squirrel-cage induction machine, stator and rotor windings of a DFIG are independently excited. The power converter is connected to the rotor winding to process the slip power. Because only part of the real power flows through the rotor circuit, the power rating of the converter need only be about 20% - 30% of the rated turbine output. A control system is employed to regulate the real and reactive power (by regulating the current flowing in the rotor winding) to extract the maximum possible power from the wind and to regulate the reactive power output of the generator. The control method usually employed is vector control or field-oriented control, though direct torque control (DTC) has also been used. This chapter concentrates on vector control because it is the predominant control method. Vector control allows decoupling of real and reactive power control, i.e., real power can be independently controlled without affecting reactive power output and vice versa. Although DFIG wind turbines are generally more complex and expensive than wind turbines employing uncontrolled squirrel-cage induction generators or rotor-resistance controlled wound-rotor machines, they have certain advantages:

- Independent active real and reactive power control is possible;
- There is a wide generator shaft speed range of up to 30% above and below rated speed for which generation can take place with minimum slip losses;

- Maximized aerodynamic power extraction;
- Improved fault ride-through performance, and;
- They can be controlled to reduce mechanical stress.

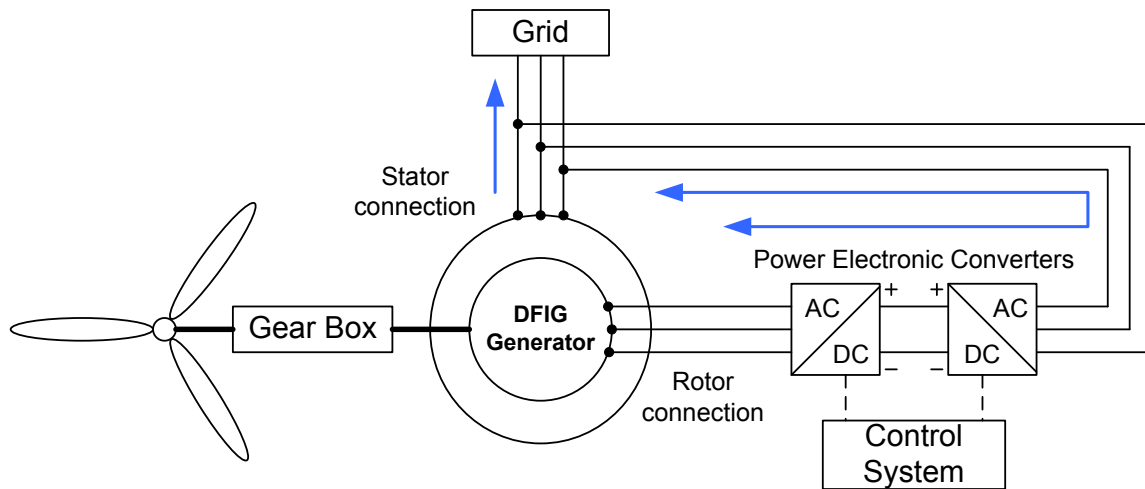


Figure 4.1: Schematic for a doubly-fed induction generator (DFIG).

DFIGs have some advantages over full-converter machines as well. Full-converter machines use an AC-DC-AC converter for the stator, which means that the converter has to be rated for the entire output power of the generator, thus increasing the cost relative to DFIGs. The electrical dynamic performance of the DFIG at the fundamental frequency is dominated by the converter. The conventional aspects of generator performance related to internal angle, excitation voltage, and synchronism are not relevant in the case of the DFIG, as it is an induction machine. Since the rotor rotates faster than the rotating magnetic field set up by the stator, the internal angle changes continuously. The current regulated power converter determines the desired values of real and reactive power. The electrical behavior of the generator and converter in the DFIG is largely like that of a current-regulated voltage source inverter, which may be simplified for modeling purposes as being a regulated current source.

To apply the vector control method to control real and reactive power output, it is necessary to understand the behavior of the wound rotor induction machine. In this section, the winding arrangement, equivalent circuit and principle of operation of a wound rotor machine are described, along with the supporting equations. The equations show that in the stationary abc reference frame, machine parameters such as inductance are time-varying. The equivalent circuit in the stationary abc reference frame is transformed using the Park transform to the equivalent in the rotating qd0 reference frame, to make machine parameters such as inductance time-invariant. In the qd0 reference frame, the q-axis and d-axis are 90 degrees apart and hence decoupled. It is shown that q-axis currents can be used to control real power and d-axis currents can be used to control reactive power, and that a simplified representation of the power electronic converter and induction generator as a regulated current source is indeed valid.

The winding arrangement of a conventional 2-pole, 3-phase, wye-connected symmetrical induction machine is shown in Figure 4.2. The stator windings are identical with equivalent turns  $N_s$  and resistance  $r_s$ . The rotor windings can be approximated as identical windings with equivalent turns  $N_r$  and resistance  $r_r$ . The air-gap is uniform and the windings are approximated to be sinusoidally distributed.

In Figure 4.2, the winding of each phase is represented by an elementary coil. One side of the coil is represented by a  $\otimes$  indicating that the assumed positive direction of current is down the length of the stator (into the paper). The other side of the same coil is represented by a  $\odot$  which indicates that the assumed positive direction of current is out of the paper. The axes  $as$ ,  $bs$ , and  $cs$  represent the positive directions of the magnetic fields

produced due to the currents flowing in the stator windings of phase  $a$ ,  $b$ , and  $c$  respectively. These directions are obtained by using the right hand rule on the phase windings. Similarly axes  $ar$ ,  $br$ , and  $cr$  with respect to the rotor windings are shown. These rotor axes are fixed to the rotor and rotate with it at an angular velocity of  $\omega_r$ . The angular displacement of the rotor with respect to the positive  $as$  axis is  $\theta_r$ .

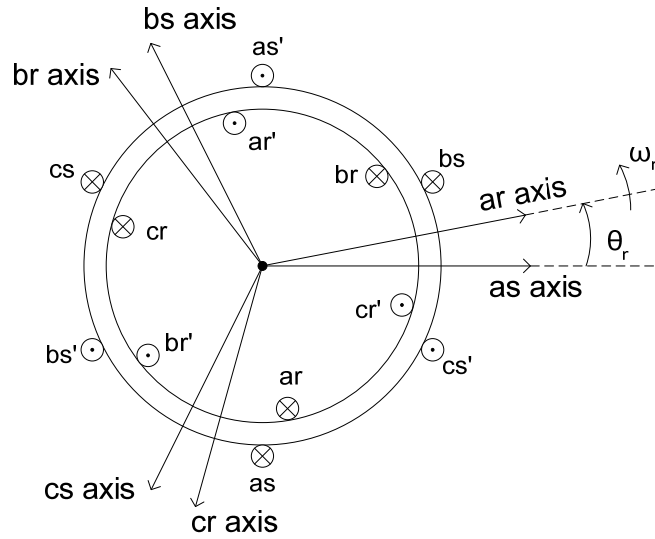


Figure 4.2: Schematic winding diagram.

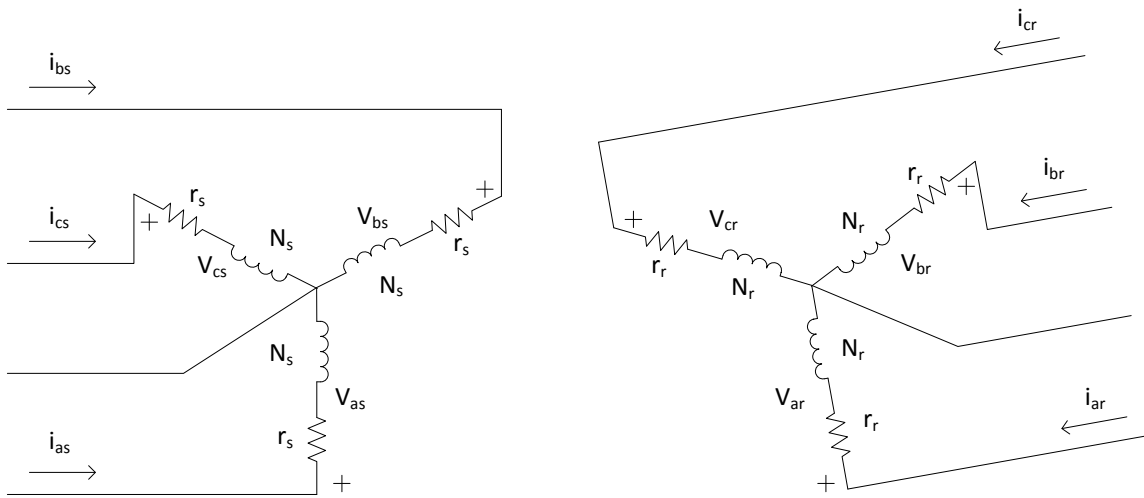


Figure 4.3: Equivalent Circuit (2-pole, 3-phase, wye-connected IM)

In the stationary  $abc$  reference frame, the relationships between the voltages, currents, and flux linkages of each phase for this machine can be written from Figure 4.3. They are as follows.

Stator Voltage Equations:

$$V_{as} = r_s i_{as} + \frac{d\lambda_{as}}{dt} \quad (4.1)$$

$$V_{bs} = r_s i_{bs} + \frac{d\lambda_{bs}}{dt} \quad (4.2)$$

$$V_{cs} = r_s i_{cs} + \frac{d\lambda_{cs}}{dt} \quad (4.3)$$

Rotor Voltage Equations (referred to the stator side):

$$V_{ar}' = r_r' i_{ar}' + \frac{d\lambda_{ar}'}{dt} \quad (4.4)$$

$$V_{br}' = r_r' i_{br}' + \frac{d\lambda_{br}'}{dt} \quad (4.5)$$

$$V_{cr}' = r_r' i_{cr}' + \frac{d\lambda_{cr}'}{dt} \quad (4.6)$$

where  $\lambda$  denotes the flux linkage, subscripts  $s$  and  $r$  indicate variables and parameters associated with the stator and rotor respectively, and prime ' indicates variables and parameters referred to the stator side.

Rewriting the stator and rotor voltage equations in the matrix form yields:

$$\overline{V_{abcs}} = \overline{r_s' i_{abcs}} + p \overline{\lambda_{abcs}} \quad (4.7)$$

$$\overline{V'_{abcr}} = \overline{r_r' i'_{abcr}} + p \overline{\lambda'_{abcr}} \quad (4.8)$$

where  $p$  stands for a differentiation operator. The flux linkages in Equations 4.7 and 4.8 are expressed as:

$$\overline{\lambda_{abcs}} = \overline{L_s i_{abcs}} + \overline{L'_{sr} i'_{abcr}} \quad (4.9)$$

$$\overline{\lambda'_{abcr}} = \overline{L_{sr}^T i_{abcs}} + \overline{L_r' i'_{abcr}} \quad (4.10)$$

where the winding inductances are given by:

$$\overline{L_s} = \begin{bmatrix} L_{ls} + L_{ms} & -\frac{1}{2}L_{ms} & -\frac{1}{2}L_{ms} \\ -\frac{1}{2}L_{ms} & L_{ls} + L_{ms} & -\frac{1}{2}L_{ms} \\ -\frac{1}{2}L_{ms} & -\frac{1}{2}L_{ms} & L_{ls} + L_{ms} \end{bmatrix} \quad (4.11)$$

$$\overline{L_r'} = \begin{bmatrix} L_{lr}' + L_{ms} & -\frac{1}{2}L_{ms} & -\frac{1}{2}L_{ms} \\ -\frac{1}{2}L_{ms} & L_{lr}' + L_{ms} & -\frac{1}{2}L_{ms} \\ -\frac{1}{2}L_{ms} & -\frac{1}{2}L_{ms} & L_{lr}' + L_{ms} \end{bmatrix} \quad (4.12)$$

$$\overline{L_{sr}'} = L_{ms} \begin{bmatrix} \cos\theta_r & \cos(\theta_r + 120^\circ) & \cos(\theta_r - 120^\circ) \\ \cos(\theta_r - 120^\circ) & \cos\theta_r & \cos(\theta_r + 120^\circ) \\ \cos(\theta_r + 120^\circ) & \cos(\theta_r - 120^\circ) & \cos\theta_r \end{bmatrix} \quad (4.13)$$

In the above inductance equations,  $L_{ls}$  and  $L_{ms}$  are the leakage and magnetizing inductances of the stator windings, respectively.  $L_{lr}'$  is the leakage inductance of the rotor windings referred to the stator. Combining Equations 4.7 through 4.10, we get:

$$\overline{V_{abcs}} = (\overline{r_s} + p \overline{L_s}) \overline{i_{abcs}} + p \overline{L_{sr}' i'_{abcr}} \quad (4.14)$$

$$\overline{V_{abc r'}} = p\overline{L_{sr}^T i_{abc s}} + (\overline{r_r'} + p\overline{L_r'})\overline{i_{abc r'}} \quad (4.15)$$

Inductances, voltages, and current quantities in Eqs. 4.14 and 4.15 are derived in the stationary  $abc$  reference frame. They are thus time-variant. Analysis and modeling will be unnecessarily cumbersome. Time variant quantities can be made time invariant by transforming them into an appropriate rotating reference frame, i.e., the rotating  $qdo$  reference frame. Using Park transforms, Equations 4.14 and 4.15 become,

$$\overline{V_{qd0s}} = \overline{r_s i_{qd0s}} + \omega\overline{\lambda_{dqs}} + p\overline{\lambda_{qd0s}} \quad (4.16)$$

$$\overline{V'_{qd0r}} = \overline{r_r' i'_{qd0r}} + (\omega - \omega_r)\overline{\lambda'_{dqr}} + p\overline{\lambda'_{qd0r}} \quad (4.17)$$

where  $\omega$  and  $\omega_r$  are the rotational speeds of the  $qdo$  reference frame and the rotor frame respectively. They are given in rad/s. Equations 4.16 and 4.17 can be expanded as follows.

Stator Voltage Equations:

$$V_{qs} = r_s i_{qs} + \omega\lambda_{ds} + p\lambda_{qs} \quad (4.18)$$

$$V_{ds} = r_s i_{ds} - \omega\lambda_{qs} + p\lambda_{ds} \quad (4.19)$$

$$V_{0s} = r_s i_{0s} + p\lambda_{0s} \quad (4.20)$$

Rotor Voltage Equations:

$$V'_{qr} = r_r' i'_{qr} + (\omega - \omega_r)\lambda'_{dr} + p\lambda'_{qr} \quad (4.21)$$

$$V'_{dr} = r_r' i'_{dr} - (\omega - \omega_r)\lambda'_{qr} + p\lambda'_{dr} \quad (4.22)$$

$$V'_{0r} = r_r' i'_{0r} + p\lambda'_{0r} \quad (4.23)$$

Likewise, the flux linkages in the rotating  $qdo$  frame are given by:

Stator Flux Equations:

$$\lambda_{qs} = (L_{ls} + L_M)i_{qs} + L_M i'_{qr} \quad (4.24)$$

$$\lambda_{ds} = (L_{ls} + L_M)i_{ds} + L_M i'_{dr} \quad (4.25)$$

$$\lambda_{0s} = L_{0s} i_{0s} \quad (4.26)$$

Rotor Flux Equations:

$$\lambda'_{qr} = L_M i_{qs} + (L'_{lr} + L_M) i'_{qr} \quad (4.27)$$

$$\lambda'_{dr} = L_M i_{ds} + (L'_{lr} + L_M) i'_{dr} \quad (4.28)$$

$$\lambda'_{0r} = L'_{lr} i'_{0r} \quad (4.29)$$

where  $L_M = \frac{3}{2} L_{ms}$ . Note that the reference frame rotates at a speed of  $\omega$ . Equations 4.18 through 4.29 can be visualized as the equivalent circuits shown in Figure 4.4.

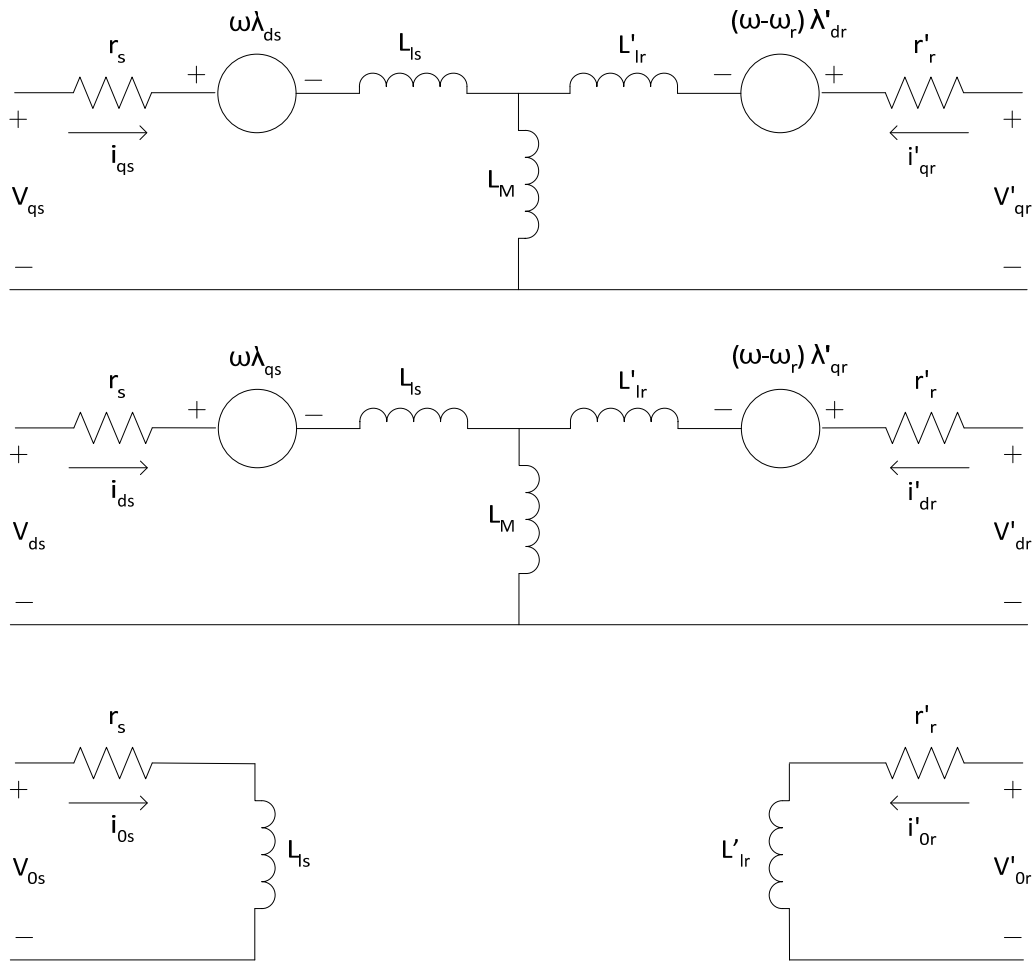


Figure 4.4: Equivalent circuits for a 3-phase, symmetrical induction machine in the  $qd0$  reference frame.

The electromechanical torque developed in the rotor winding corresponds to the rotor mechanical power over its mechanical speed. Equation 4.30 shows that the electromechanical torque can be expressed in terms of  $q$ -axis and  $d$ -axis currents and flux linkages, indicating that decoupled control of real and reactive power output of a DFIG may be feasible.

$$T_{em} = \frac{3P}{2} L_m (\lambda_{ds} i_{qs} - \lambda_{qs} i_{ds}) \text{ [Nm]} \quad (4.30)$$

#### 4.3.2 Modeling Approach: Use of Regulated Current Source instead of Detailed Device Models

The behavior of a DFIG control system to independently control the real and reactive power allows the use of a regulated current source in the dynamic model to represent the induction generator and power electronics. The main concern was to ensure that the model was suitably general and since the ultimate purpose of the model is use in load flow and dynamic stability studies, a highly detailed representation of the machine and converter is not necessary. This subsection presents the analysis behind the approximations of using a regulated current source representation instead of explicitly modeling the generator and power electronics. A simplified model of the device dynamics is adequate. The mechanical modeling of the system has also been considerably simplified, with a one-mass model being used to represent the numerous rotating masses (the turbine, gearbox, and generator). Let the wound rotor induction machine be represented in a synchronously rotating  $qd0$  reference frame as described above. The currents flowing in the stator are assumed to be balanced. These currents produce a resultant stator magnetic field which has a constant magnitude and is rotating at synchronous speed. Since the angular speeds of

the stator magnetic field and the  $qd0$  rotating frame are identical, the vector of the stator magnetic field is fixed with respect to the  $q$ - and  $d$ - axes of the  $qd0$  rotating frame. Let the  $d$ -axis of the reference frame be oriented so that it aligns with the vector of the stator magnetic field. Figure 4.5 illustrates the orientation and alignment of the stationary  $abc$  frame, the  $qd0$  frame, and the stator magnetic field at a particular time.

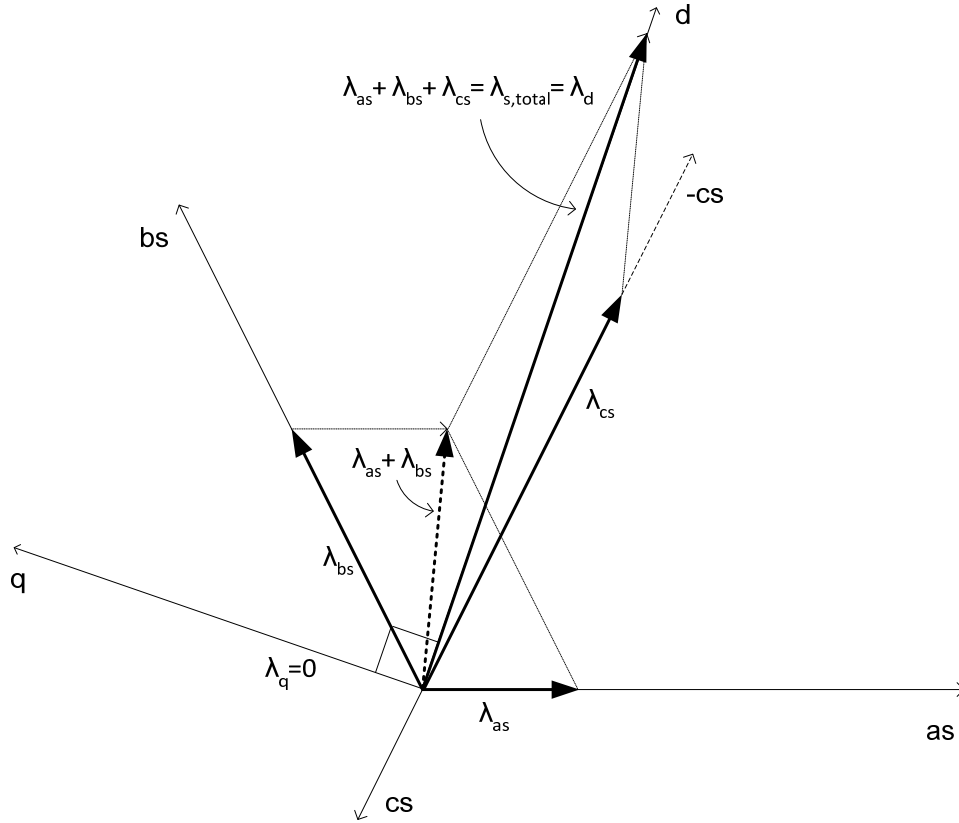


Figure 4.5:  $d$ -axis of a synchronously rotating  $qd0$  frame, aligned with the total stator magnetic field. Note that flux summation is in the vectorial sense.

Because of the alignment, the following results are obtained:

$$\lambda_{qs} = 0, \text{ and} \quad (4.31)$$

$$\lambda_{ds} = \lambda_{s,total} \quad (4.32)$$

Substituting Equations 4.31 and 4.32 into Equations 4.18 and 4.19, and assuming the winding resistive element  $r$  is negligible, the following relationships are obtained:

$$V_{qs} = \omega \lambda_{ds} = \omega \lambda_{s,total} = \text{constant} \quad (4.33)$$

$$V_{ds} = 0 \quad (4.34)$$

Equations 4.33 and 4.34 suggest that the speed voltage  $V_{qs}$  is time-invariant, and the voltage across the stator  $d$ -axis is negligible. The stator  $q$  and  $d$ -axis currents can be controlled using the rotor  $q$ - and  $d$ -axis currents. Using the stator and rotor flux equations given in Equations 4.24 and 4.25, and with  $\lambda_{qs} = 0$ , the stator  $q$ - and  $d$ -axis currents are given by:

$$i_{qs} = \left( -\frac{L_m}{L_{ls} + L_M} \right) i'_{qr} \quad (4.35)$$

$$i_{ds} = \left( \frac{\lambda_{ds} - L_m i'_{dr}}{L_{ls} + L_M} \right) \quad (4.36)$$

Inductance and flux quantities in Equations 4.35 and 4.36 are time-invariant, thus the stator  $q$ - and  $d$ -axis currents can be controlled by adjusting the rotor  $q$ - and  $d$ -axis currents appropriately. The real and reactive power in the stator windings is given by:

$$P_s = \frac{3}{2} (V_{ds} i_{ds} + V_{qs} i_{qs}) \quad (4.37)$$

$$Q_s = \frac{3}{2} (V_{ds} i_{qs} - V_{qs} i_{ds}) \quad (4.38)$$

Since the stator  $d$ -axis voltage is zero as derived in Equation 4.34, Equations 4.37 and 4.38 can be simplified as shown below:

$$P_s = \frac{3}{2} V_{qs} i_{qs} \quad (4.39)$$

$$Q_s = -\frac{3}{2} V_{qs} i_{ds} \quad (4.40)$$

The real and reactive power can be controlled by adjusting the stator  $q$ - and  $d$ -axis current. As shown in Equations 4.35 and 4.36, the stator  $q$ - and  $d$ -axis currents can be controlled by adjusting the rotor  $q$ - and  $d$ -axis currents. The stator real and reactive power is as follows:

$$P_s = -\frac{3}{2} \left( \frac{\omega \lambda_{ds} L_m}{L_{ls} + L_M} \right) i'_{qr} \quad (4.41)$$

$$Q_s = \left( \frac{\omega \lambda_{ds}}{L_{ls} + L_M} \right) (\lambda_{ds} - L_m i'_{dr}) \quad (4.42)$$

It is important to note that in a synchronously rotating reference frame, the quantities  $\omega$ ,  $\lambda_{ds}$ ,  $L_m$ , and  $L_{ls}$  are time-invariant. Thus, Equations 4.41 and 4.42 can be further simplified as follows:

$$P_s = k_{ps} i'_{qr} \quad (4.43)$$

$$Q_s = k_{qs1} - k_{qs2} \times i'_{dr} \quad (4.44)$$

where  $k_{ps}$ ,  $k_{qs1}$ , and  $k_{qs2}$  are the respective constants for the stator real and reactive power. Equations 4.43 and 4.44 clearly show that the stator real and reactive power can be independently controlled by the rotor  $q$ - and  $d$ -axis currents. Thus, the desired real power and reactive power output of a DFIG can be realized by the choosing the appropriate rotor  $q$ - and  $d$ -axis currents. Let us call these currents the reference rotor  $q$ - and  $d$ -axis currents, i.e.,  $I'_{qr}{}^{(ref)}$  and  $I'_{dr}{}^{(ref)}$ . These rotor reference currents can be generated by proportional integral controllers based on the difference between the measured and desired power quantities. Figure 4.6 illustrates how the reference rotor  $q$ - and  $d$ -axis currents are generated.

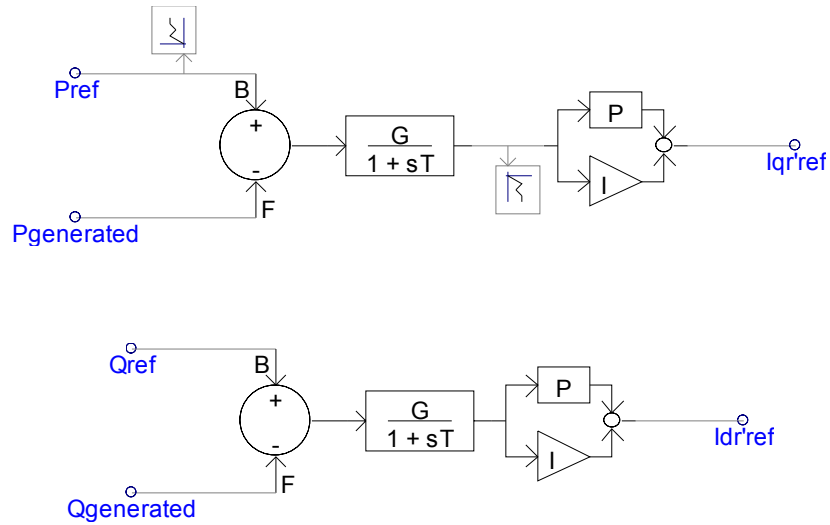


Figure 4.6: Rotor reference currents generated using proportional integral controller (based on the difference between measured and desired quantities).

Once these reference currents are obtained, they are transformed to the stationary  $abc$  frame. To summarize, the instantaneous  $abc$  current waveforms are obtained from the rotor's  $q$ - and  $d$ -axis currents through the inverse Park transformation and are fed into the three-phase current source. An alternative two-stage inverse transformation can be utilized as well, i.e., from the synchronously rotating  $qd0$  frame to the stationary  $\alpha\beta$  frame transformation, and from the stationary  $\alpha\beta$  frame to the stationary  $abc$  frame (the inverse Clarke transformation). Figure 4.7 illustrates the second method of transformation, i.e., a two-stage inverse transformation. This second method is the one used in the developed DFIG WPP model. These instantaneous currents in the  $abc$  stationary frame are then used as inputs to a current source block in the WPP model. The generator and converter have been successfully modeled using a regulated current source.

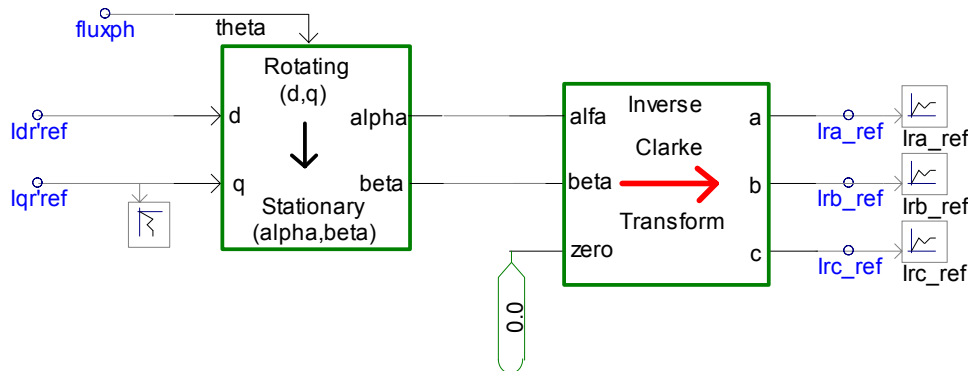


Figure 4.7: Rotor reference currents in the  $qd0$  frame are transformed into three-phase currents in the  $abc$  stationary frame.

### 4.3.3 Implementation of DFIG WPP Model in PSCAD/EMTDC

In an actual WPP, a local grid collects the output from each wind turbine into a single point of connection on the grid. As a WPP is usually made up of several identical machines, it is a reasonable approximation to parallel all the turbines into a single equivalent large turbine behind a single equivalent impedance. The rated power rating of the single equivalent wind turbine is equal to the combined rated power ratings of all wind turbines. The model described in this chapter is consistent with this “equivalencing” approach developed by the Wind Generator Modeling Group (WGMG) of the Western Electricity Coordinating Council. The single turbine equivalent

impedance represents “an average” turbine within a WPP. Thus, the collective behavior of the WPP seen from the point of interconnection is the main objective of the observation. The characteristic of individual turbines are not represented. Electrical disturbances within the collector system and underground cables interconnecting individual wind turbines cannot be analyzed. Also, there is a potentially significant variation in the equivalent impedance for the connection to each wind turbine. The single machine equivalent assumes that all the machines generate the same power output at the same time. This implies the assumption that the geographic dispersion of the farm is small enough that the wind speed profile over it is uniform.

The model developed is a simplified generic model intended for bulk power system studies where a detailed representation of a wind turbine generator is not required. The model is intended for transient stability analysis of grid disturbances. The actual device dynamics have been greatly simplified. To be specific, the very fast dynamics involved with the control of the generator-converter have been modeled as algebraic approximations of their response. This makes the generator-converter dynamics instantaneous. Simplified turbine mechanical controls along with blade aerodynamic characteristics are included in the model. This subsection presents the engineering assumptions, detailed structure, and data for each of the component models necessary to represent a DFIG-based wind turbine or WPP. Data from the Taiban Mesa wind power plant in New Mexico (rated at 204 MW, composed of 136 GE 1.5-MW DFIG turbines) has been used to develop this wind power plant model.

#### 4.3.3.1 Model Components

To develop a generic dynamic model of a DFIG WPP, each aspect of the functionality of a typical DFIG turbine must be represented. The DFIG WPP model developed herein is thus divided into four sub-systems to emulate these functions. They are summarized as follows:

- Generator-Converter sub-system: The generator-converter system is represented by a regulated current source. It injects three-phase currents into the power system in response to the control commands from the Converter Control sub-system.
- Converter Control sub-system: This sub-system consists of the Reactive Power Control and Real Power Control sub-systems. These subsystems emulate power electronics controllers in regulating real and reactive power.
- Wind Turbine sub-system: It is represented by a single-mass model and it determines the mechanical input power and the angular speed of the wind turbine based on the specified pitch angle.
- Pitch Control sub-system: The primary function of the pitch controller is to determine the desired blade pitch angle based on desired angular speed and real power.

The interaction between the device models is illustrated in Figure 4.8. A subsystems description of each is provided next.

#### *Generator-Converter Model*

In the DFIG WPP model, the combination of the wound-rotor induction generator and the power electronic controls are represented by a current regulated source as described earlier. The current source emulates the functionality of an actual DFIG wind turbine in controlling real and reactive power independently. The implementation of the three-phase current source is shown in Figure 4.9. The current source is connected to a power system at node VT. A multi-meter to measure real and reactive power and rms voltage during the simulation runtime are shown in the diagram. Additionally, three-phase voltage measurements indicated as  $V_{sA}$ ,  $V_{sB}$ , and  $V_{sC}$  are also taken. They represent stator terminal voltages.

To align the d-axis of a synchronous rotating frame of reference to the stator magnetic flux, the instantaneous angular position of the stator magnetic flux must be precisely known. The angular position is determined using the instantaneous three-phase stator voltages  $V_{sA}$ ,  $V_{sB}$ , and  $V_{sC}$ . The process is described below and illustrated in Figure 4.10. The instantaneous stator voltages  $V_{sA}$ ,  $V_{sB}$ , and  $V_{sC}$  are transformed into the stationary  $\alpha\beta$  domain

using the Clarke transform yielding  $V_{\alpha}$  and  $V_{\beta}$ . These voltages are smoothed to remove any voltage transients that might be present. The DFIG model is connected to a three-phase 34.5 kV system. The per-phase system peak voltage is 28.18 kV. The instantaneous phase a voltage is plotted in a bold line shown in Figure 4.11. The transformed voltage  $V_{\alpha}$  is identical to  $V_{sA}$ . This is as expected. The transformed voltage  $V_{\beta}$  lags  $V_{\alpha}$  by 90 degrees, also as expected.

The magnetic fluxes associated with  $V_{\alpha}$  and  $V_{\beta}$  are  $Flux\_Alpha$  and  $Flux\_Beta$  (see Figure 4.10). They are obtained by integrating  $V_{\alpha}$  and  $V_{\beta}$  respectively, since the electromotive force is proportional to the time rate of change of the flux, to become  $Flux\_Alpha$  and  $Flux\_Beta$ , respectively.

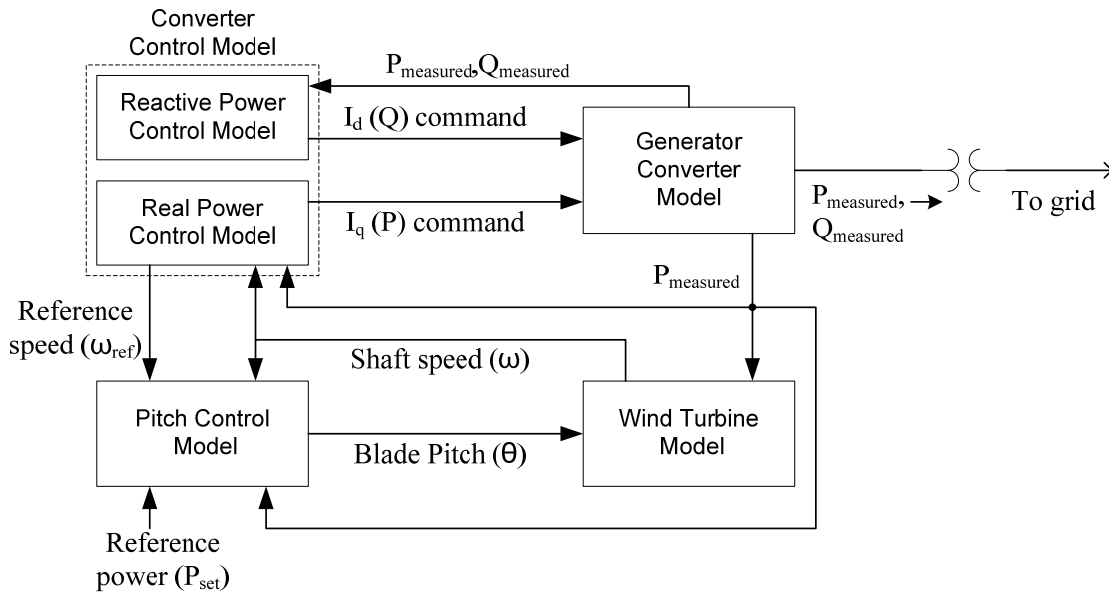


Figure 4.8: DFIG WPP model sub-systems.

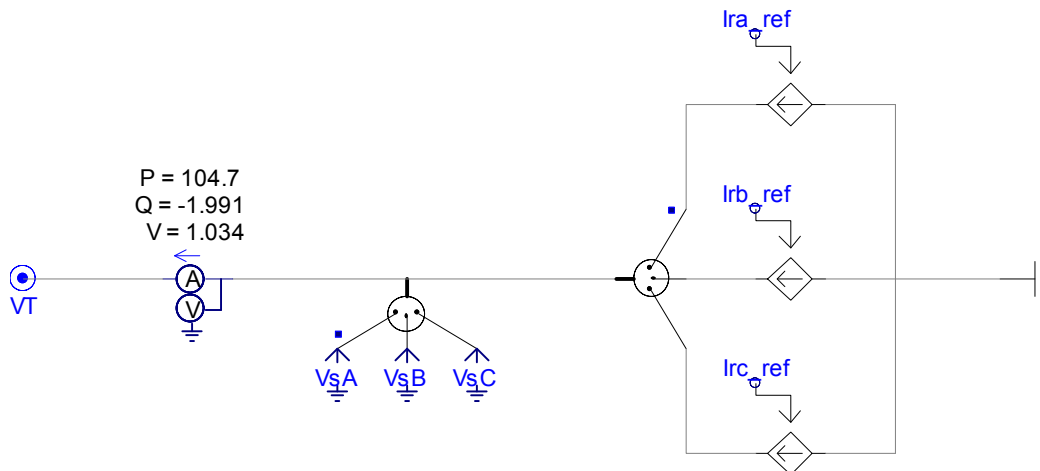


Figure 4.9: Regulated current source implemented in PSCAD/EMTDC.

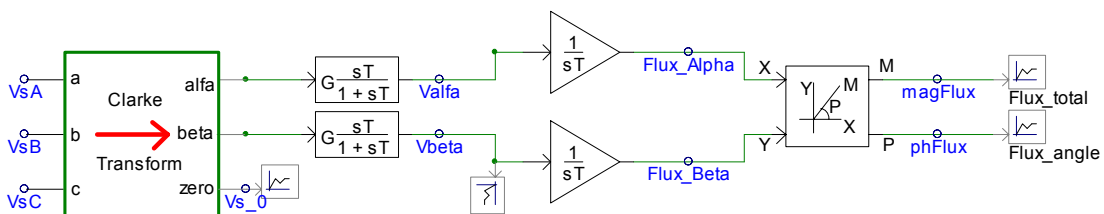


Figure 4.10: Stator flux magnitude and the instantaneous angular position are determined using the Clarke transform.

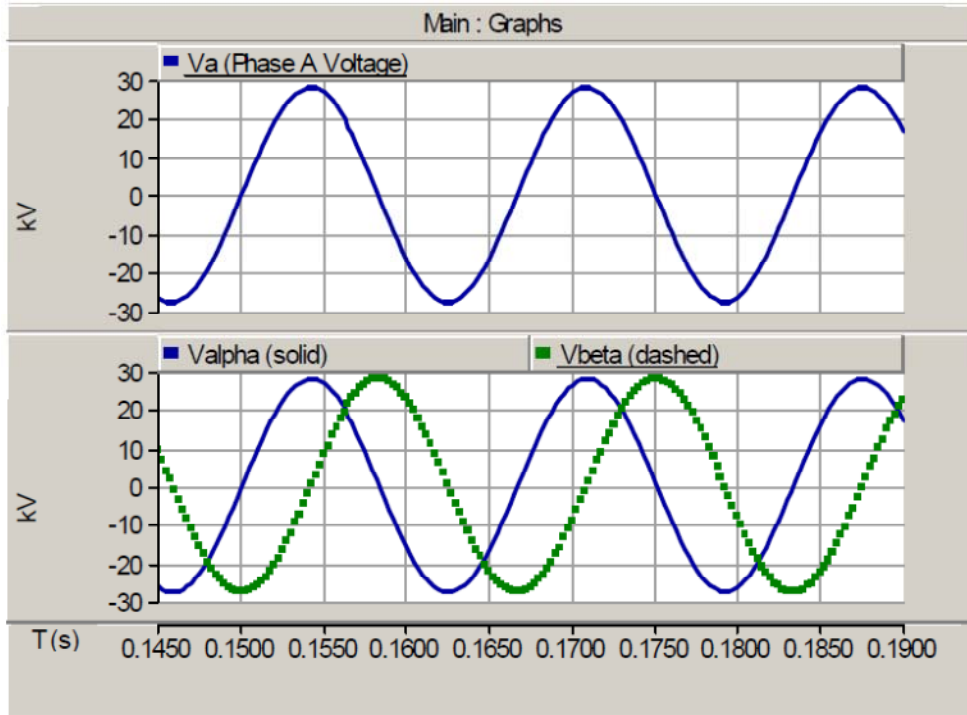


Figure 4.11: Instantaneous phase a voltage waveform and transformed voltage  $V_{\alpha}$  and  $V_{\beta}$  in the  $\alpha\beta$  domain.

Note that Flux Alpha and Flux Beta quantities are time-varying. The total magnitude of these fluxes and their instantaneous angular positions are given by:

$$\text{magFlux} = \sqrt{\text{Flux\_Alpha}^2 + \text{Flux\_Beta}^2} \quad (4.45)$$

$$\text{phFlux} = \text{atan} \frac{\text{Flux\_Alpha}}{\text{Flux\_Beta}} \quad (4.46)$$

The magnitude of the stator flux for this particular case is time invariant at 74.7 Wb. The actual magnitude of the flux is for illustration only and not important as it depends on a number of factors such as the stator resistance. The instantaneous flux position varies linearly from  $-\pi$  to  $\pi$  as shown in Figure 4.12.

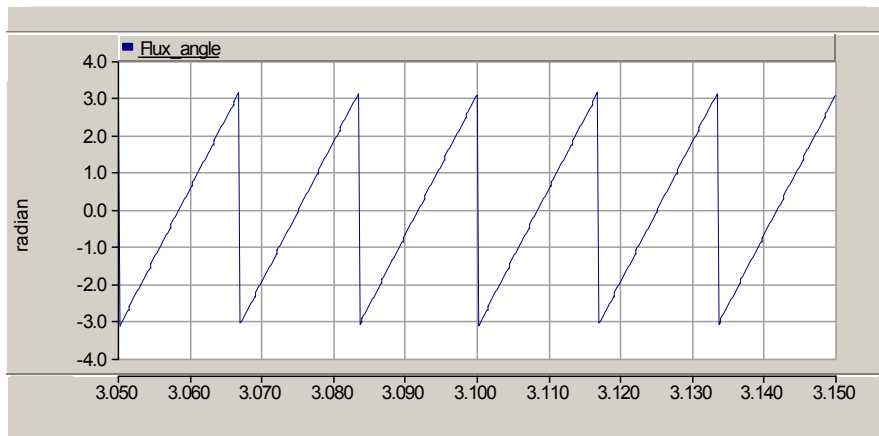


Figure 4.12: Instantaneous position of the stator magnetic flux.

With a precisely known position of the stator magnetic field, the  $d$ -axis of a synchronous rotating reference can be oriented as desired. The orientation of the frame is validated by transforming the flux and voltage components in the stationary  $\alpha\beta$  frame to the rotating  $qd0$  frame with its  $d$ -axis aligned along the total magnetic field. The instantaneous angular position used in the transformation is given in Equation 4.46. The stator flux in the  $q$ - and  $d$ -axis ( $Flux_q$  and  $Flux_d$ ) should then be zero and the time-invariant total magnetic flux obtained in Equation 4.45 (in this case 74.7 Wb) respectively. Similarly, voltages in the  $q$ - and  $d$ -axis should be peak system voltage and zero respectively. The simulation results confirm these expectations as illustrated in Figures 4.13 and 4.14.

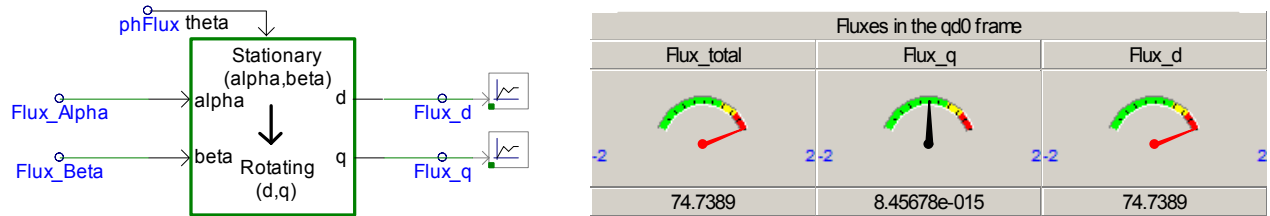


Figure 4.13: Fluxes in the  $qd0$  frame: The simulation results confirm the synchronously rotating frame is properly oriented as evidence by the magnitude of the fluxes in the  $q$ - and  $d$ -axis.

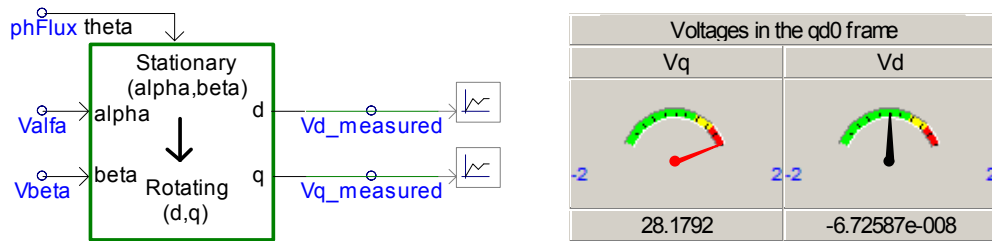


Figure 4.14: Voltages in the  $qd0$  frame: The simulation results confirm the synchronously rotating frame is properly oriented as evidence by the magnitude of the fluxes in the  $q$ - and  $d$ -axis.

The three-phase current source in the stationary  $abc$  frame can now be controlled using reference currents specified by the Converter Control subsystem in the  $qd0$  frame,  $I_d\_cmd$  and  $I_q\_cmd$ . A two-stage transformation is used as illustrated in Figure 4.15 below. Desired currents  $I_d\_cmd$  and  $I_q\_cmd$  in the synchronous rotating frame are transformed to the stationary  $\alpha\beta$  frame and finally to the stationary  $abc$  frame to become  $I_{ra\_ref}$ ,  $I_{rb\_ref}$ , and  $I_{rc\_ref}$ . These reference currents are injected to the grid through the current source model shown in Figure 4.9.

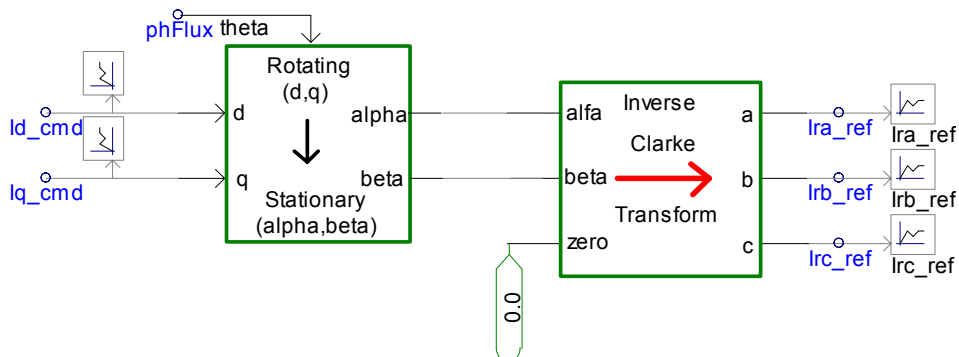


Figure 4.15: Reference currents for the regulated current source generated using a two-stage transformation.

### Converter Control Model

This model controls the active and reactive power to be delivered to the grid. The active and reactive power controls are independent of each other. The parameters and power signals for the active and reactive power control are per unit of the specified MW capacity of the WPP (specified on machine base MBASE).

### Reactive Power Control Model

The reactive power control module generates the desired  $d$ -axis current  $I_{d\_cmd}$  for the generator-converter sub-system. The desired  $d$ -axis current  $I_{d\_cmd}$  is obtained using a proportional integral controller shown in Figure 4.16. The difference between the actual (measured) reactive power ( $Q_{measured}$ ) and the desired or reference reactive power ( $Q_{genRef}$ ) is used to drive the PI controller. There are three modes of reactive power control - constant power factor, constant reactive power, and constant terminal voltage. The model described in this chapter implements the first two control modes only. The constant power factor control determines the desired reactive power  $Q_{PFdesired}$  required to achieve the desired constant power factor at the generator terminals ( $PF_{desired}$ ). The desired reactive power is given in Equation 4.47 and implemented as shown in Figure 4.17. It is then supplied to the PI controller directly as  $Q_{genRef}$  as shown in Figure 4.16. The constant reactive power mode is straightforward as the desired constant reactive power is supplied directly as  $Q_{genRef}$  in Figure 4.16.

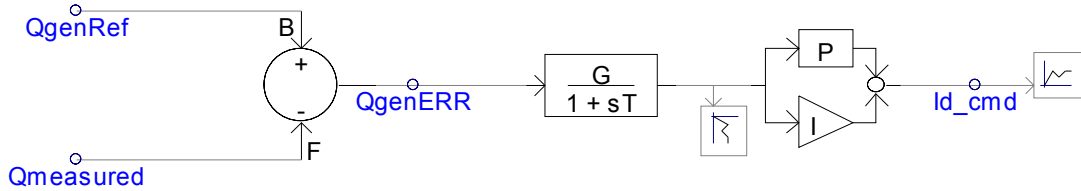


Figure 4.16: The desired  $d$ -axis current is generated using a proportional integral controller.

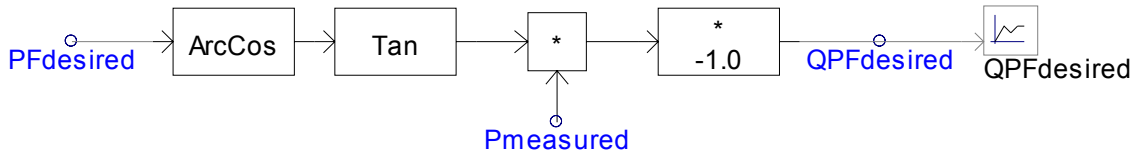


Figure 4.17: Calculation of the desired reactive power to achieve a constant power factor at the generator terminals.

$$Q_{PFdesired} = -P_{measured} \tan(\arccos(PF_{desired})) \quad (4.47)$$

### Real Power Control Model

This block controls the real or active power delivered to the grid. The non-linear power-speed characteristic based on the data supplied in Table 4.1 is shown in Figure 4.18. This characteristic is used to model the desired generator speed as a function of the power level. The input data used for this function are values of the desired speed at various levels of power output, with linear interpolation used between the specified values. The per-unitized measured real power is fed into this function. The obtained output is then the desired angular speed  $\omega_{Ref}$ . The desired angular speed  $\omega_{Ref}$  is then compared with the measured angular speed  $\omega$ , and the desired power  $P_{ord}$  is obtained through the use of a PI controller. This desired power  $P_{ord}$  is compared with the measured power  $P$  and fed through a PI controller to give desired  $q$ -axis current  $I_{q\_cmd}$ .

Table 4.1: Real power vs. rotor speed.

Real Power	Rotor Speed
pu	pu
0.00	0.688
0.08	0.689
0.16	0.690
0.20	0.780
0.40	0.980
0.60	1.120
0.74	1.198
0.87	1.199
1.00	1.200

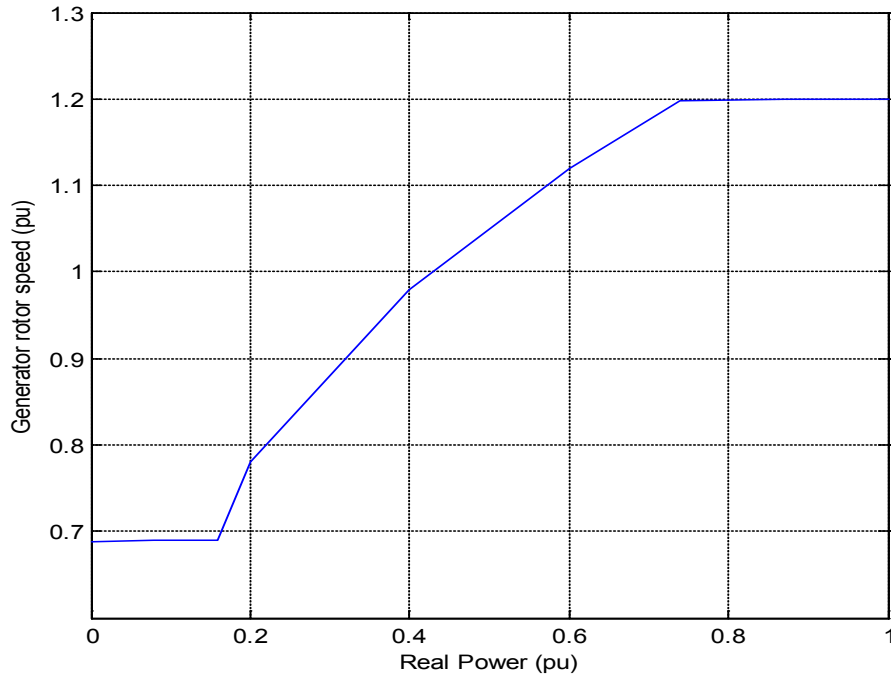


Figure 4.18: Non-linear power-speed characteristic of generator.

#### Wind Turbine Mechanical Model

This model calculates the instantaneous shaft speed  $\omega$  of the wind turbine generator. For this purpose, it uses data about the pitch angle, wind speed, and real power. Parameters and power signals are per unit (pu) on the rated power capacity specified for the model. The wind turbine, the induction generator, and all moving mechanical parts have been lumped together into a single mass for simplification. The rotor performance of a wind turbine is usually characterized by its power coefficient  $C_p$ .  $C_p$  is the fraction of the power available in the wind that can be extracted by the rotor. A  $C_p$  curve is a graph of  $C_p$  versus wind speed for a fixed blade pitch. A wind turbine thus has various  $C_p$  curves for various pitch angles which characterize the given turbine. The model includes a simplified aerodynamic model to estimate the  $C_p$  curve using the current and initial pitch angles. Equation 4.48 below represents this aerodynamic model.

$$\Delta P = K_{aero} \theta (\theta - \theta_0) \quad (4.48)$$

where  $\Delta P$  is the incremental real power,  $K_{aero}$  is the aerodynamic gain factor,  $\theta$  is the pitch angle of the turbine blades, and  $\theta_0$  is the initial pitch angle. The aerodynamic gain factor  $K_{aero}$  has been given a default value of 0.007 determined from the analysis of one set of  $C_p$  curves. The initial pitch angle  $\theta_0$  is calculated below:

$$\theta_0 = \frac{\text{Theta2}}{0.75} \left( 1 - \frac{1}{V_{windpu}^2} \right) \quad (4.49)$$

Equation 4.49 assumes that the blade pitch is  $0^\circ$  at the rated wind speed and  $\text{Theta2}$  degrees at twice rated wind speed. The value of  $\text{Theta2}$  supplied is  $26^\circ$ .  $V_{windpu}$  is the velocity of the wind in per unit of the rated wind velocity (13 m/s). The aerodynamic power extractable from the incident wind is given by the expression:

$$P_{wind} = \frac{1}{2} \rho A C_p V_{wind}^3 \quad (4.50)$$

Where  $\rho$  is the density of the air,  $A$  is the area swept by the turbine blades perpendicular to the incident wind,  $C_p$  is the power coefficient of the wind turbine, and  $V_{wind}$  is the velocity of the incident wind. Converting Equation 4.500 into per unit using MW capacity and rated wind speed as bases:

$$P_{windpu} = V_{windpu}^3 \quad (4.51)$$

Equation 4.48 represents the amount of power that is to be subtracted from the maximum power extractable from the wind to give the actual mechanical power delivered by the wind turbine to the generator. For wind speeds below rated, the pitch control model generates a zero pitch angle. This causes  $\Delta P$  in Equation 4.48 to become zero. Thus, the entire power extractable from the wind is delivered as mechanical power to the generator. For wind speeds above rated, the pitch control model generates a negative pitch angle and Equation 4.49 gives a positive value of larger magnitude. These combine to give a net positive value of  $\Delta P$  to be subtracted from the maximum extractable power from the wind. The positive value is controlled in such a way as to keep the output of the generator at a constant set value (usually the rated MW capacity) for wind speeds higher than rated speed (13 m/s). Thus, the Real Power vs. Wind-Speed Curve obtained is as follows:

- Below rated wind speed : Real Power generated in per unit is  $P_{pu} = V_{windpu}^3$
- Above rated wind speed : Real Power generated in per unit is  $P_{pu} = 1$

Thus, the power generated at wind speeds below rated is proportional to the power available in the wind. This curve is shown below in Figure 4.19. Equation 4.52 is used to find the instantaneous shaft speed  $\omega$ . In transient stability studies, this is the fundamental equation that determines rotor dynamics. The speed of the rotating stator magnetic field  $\omega_{syn}$ , also called the synchronous speed, is set to  $2\pi 60 = 377$  rad/s.

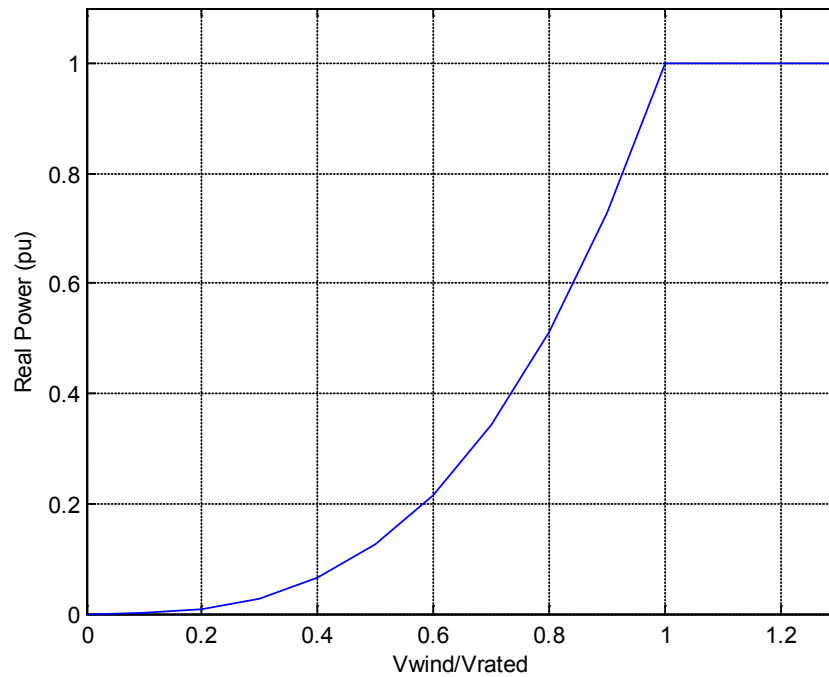


Figure 4.19: Real Power vs Wind Speed Curve.

$$P_{mechpu} - P_{elec pu} = \frac{2H}{\omega_s} \omega_{pu} \frac{d^2 \delta}{dt^2} \quad (4.52)$$

$$\therefore \frac{d\delta}{dt} = \int \frac{(P_{mech} - P_e) \omega_s}{2H \omega_{pu}} \quad (4.53)$$

We also use the relation:

$$\omega = \omega_s + \frac{d\delta}{dt} \quad (4.54)$$

#### Pitch Control Model

This model ensures that for wind speeds lesser than the rated speed, the pitch of the blades is kept at zero degrees. Above the rated speed, it keeps the pitch at a fixed value. The variable  $P_{set}$  fixes the percentage of the rated MW capacity that is required to be generated by the wind farm. It is usually kept fixed at 1 pu. The values of the constants and limits are very important in this block to ensure that the pitch remains zero at lesser wind speeds. Therefore, the pitch depends on both the instantaneous wind turbine generator speed as well as the real power output of the wind turbine. The pitch control model is shown below in Figure 4.20.

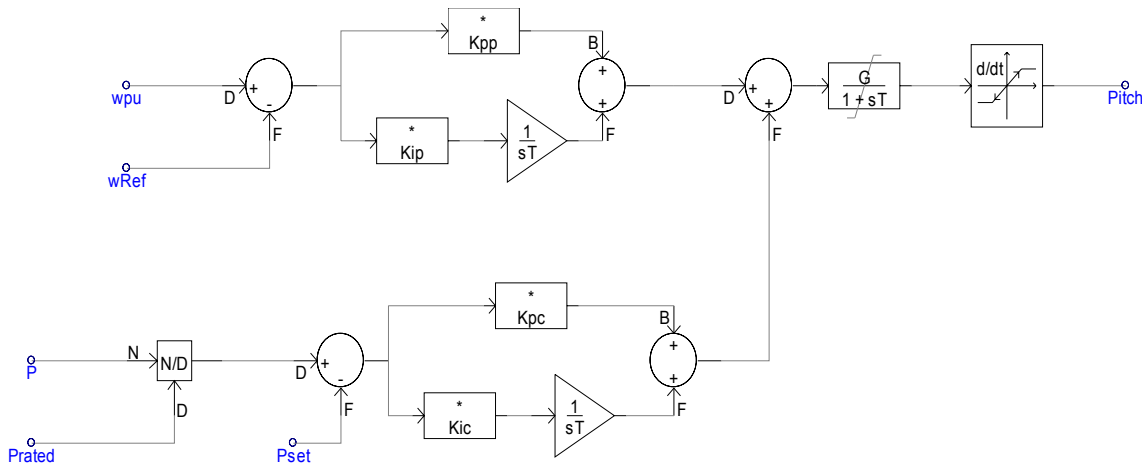


Figure 4.20: Pitch control sub-system.

#### 4.3.4 Model Development Summary

In summary, the theory behind DFIGs has been explained, the modeling approach has been elaborated, and the time-domain WPP model developed using the approach has been described in detail in this section. The next two sections describe the performance of this model and its validation using real-world data.

### 4.4 Three-Phase Model: Steady-State Performance

The development of the time-domain DFIG WPP model ("time-domain model") described in the previous chapter required individual testing of each of the sub-models to check if they were operating as expected. This testing was carried out and the results from each sub-model were satisfactory. The next step was to assemble the sub-models into the complete time-domain model. To test the complete time-domain model, it was connected to an ideal source (infinite bus) in order to study its performance under steady-state and quasi-steady-state conditions (implying changing reactive power demand and/or wind speed, but no short-circuit conditions on the system) as shown in Figure 4.21.

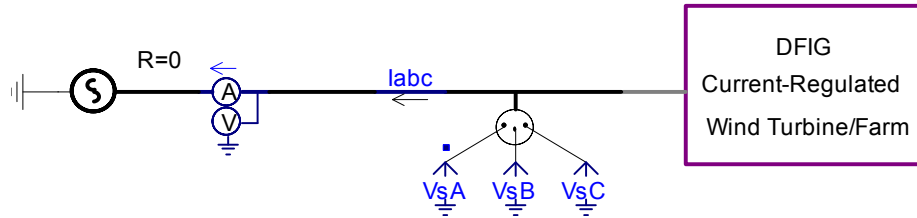


Figure 4.21: Time-domain WPP Model Connected to Ideal Voltage Source

The following questions about the time-domain model's performance needed to be answered:

- Does the  $qd0$ -domain real and reactive power calculation method used by time-domain model give results that can be verified using the phasor-domain calculation method?
- Does the wind power curve of the time-domain model approximate that of a real world DFIG WPP of similar power rating?
- Does the controller achieve the extraction of the maximum extractable power at rated wind speed?
- Can the controller be set to extract a fraction of the maximum extractable power (e.g., 80% of maximum extractable power instead of 100%) without affecting controller operation?
- How does the controller respond to a change in wind speed from rated wind speed to a speed above rated speed and also to a speed below rated speed?
- Does the reactive power controller achieve the demanded reactive power output?
- Is the reactive power control decoupled from real power control? Does changing the reactive power demand cause a change in real power output?

The  $qd0$ -domain computation used to calculate the real and reactive power was validated first. The model was then subjected to tests to determine if the performance of the model conformed to that of a real-world DFIG WPP, and the results are presented. They show that the model performed as expected.

#### 4.4.1 Method of Computing Real and Reactive Power in the $qd0$ Frame with Validation

For the purpose of calculating the real and reactive power flow out of the time-domain model into the infinite bus, we transform the available three-phase voltage and current data to the  $qd0$ -domain and then we make use of equations in the  $qd0$  frame of reference. The voltage and current data are extracted from the model and processed using a script developed in MATLAB. We shall first validate the real and reactive power calculations in the  $qd0$ -domain by comparing the results obtained from these calculations with those obtained from calculations in the steady-state phasor domain. For the comparison process we run the time domain model with parameter values shown in Table 4.2 below. The current data is then extracted from the model for calculation purposes.

- $V_{source}$  is the fixed voltage of the ideal voltage source (infinite bus) connected to the time-domain DFIG WPP model.
- $P_{rated}$  is the rated capacity of the WPP in MW. This is the real power that the WPP is expected to supply to the infinite bus at rated wind speed.
- $Q_{genRef}$  is the reactive power demanded from the WPP (the reactive power that the WPP is expected to supply to the infinite bus).
- $V_w$  is the velocity of incident wind. The rated wind speed for the time-domain model is 13 m/s (a more detailed discussion on the rated wind speed is presented later in this section).

Table 4.2: Parameter Values for Time-Domain Model.

$V_{source}$ kV rms LL	$P_{rated}$ MW	$Q_{genRef}$ MVAR	Wind Speed m/s
138	204	20	13

Note that since both real power and reactive power are flowing from the WPP to the infinite bus, the signs of both will be the same (positive). The phasor-domain calculations and the  $qd0$ -domain calculations for real and reactive power are discussed in the following subsections.

#### 4.4.1.1 Calculations in the Phasor Domain

Instantaneous three-phase voltage and current waveforms from the infinite bus connected to the time-domain WPP model are extracted. Per-phase real and reactive power is computed in the phasor domain. The total three-phase power is the sum of individual phase real and reactive power. Figure 4.22, Figure 4.23, and Figure 4.24 show normalized voltage and current waveforms for each phase. For each phase, voltage and current waveforms are shown in per-unit of their rated values for easy comparison. The voltage in each phase is seen to lead the current.

Phase A:

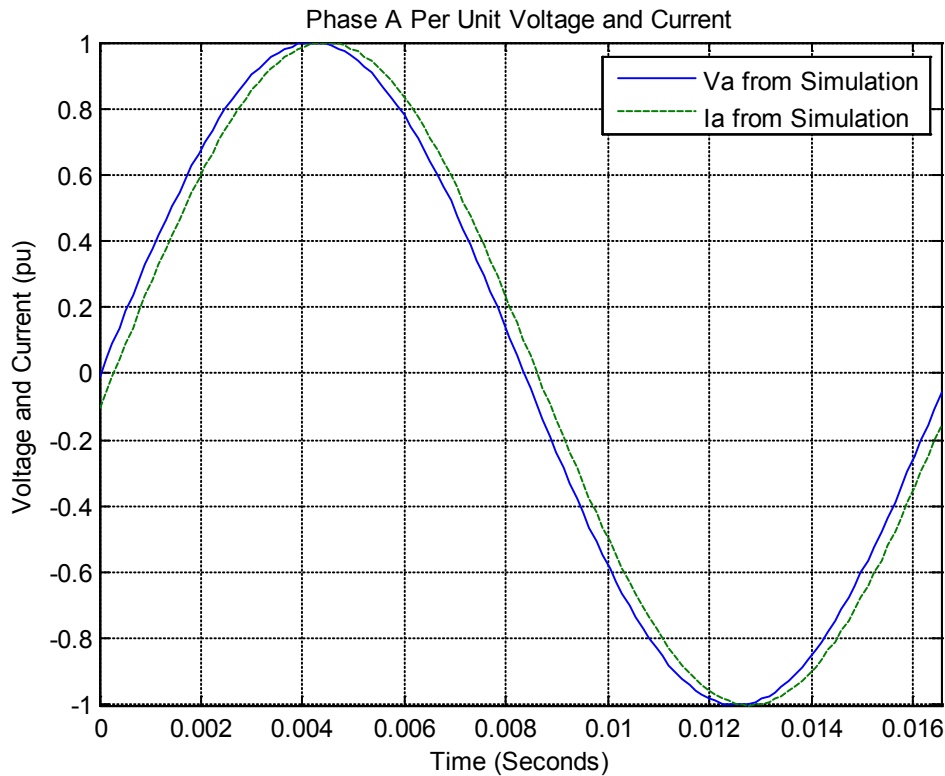


Figure 4.22: Phase A per unit voltage and current.

Here,

$$V_{rms} = 79.67 \text{ kV}$$

$$I_{rms} = 857.52 \text{ A}$$

$$V_{phase} - I_{phase} = +5.59^\circ$$

This gives us:

$$\therefore \text{Real Power} = V_{rms} \times I_{rms} \times \cos(V_{phase} - I_{phase}) = 68 \text{ MW}$$

$$\therefore \text{Reactive Power} = V_{rms} \times I_{rms} \times \sin(V_{phase} - I_{phase}) = 6.66 \text{ Mvar}$$

Phase B:

Here,

$$V_{rms} = 79.67 \text{ kV}$$

$$I_{rms} = 857.51 \text{ A}$$

$$V_{phase} - I_{phase} = +5.585^\circ$$

$$\text{Real Power} = 67.99 \text{ MW}$$

$$\text{Reactive Power} = 6.65 \text{ Mvar}$$

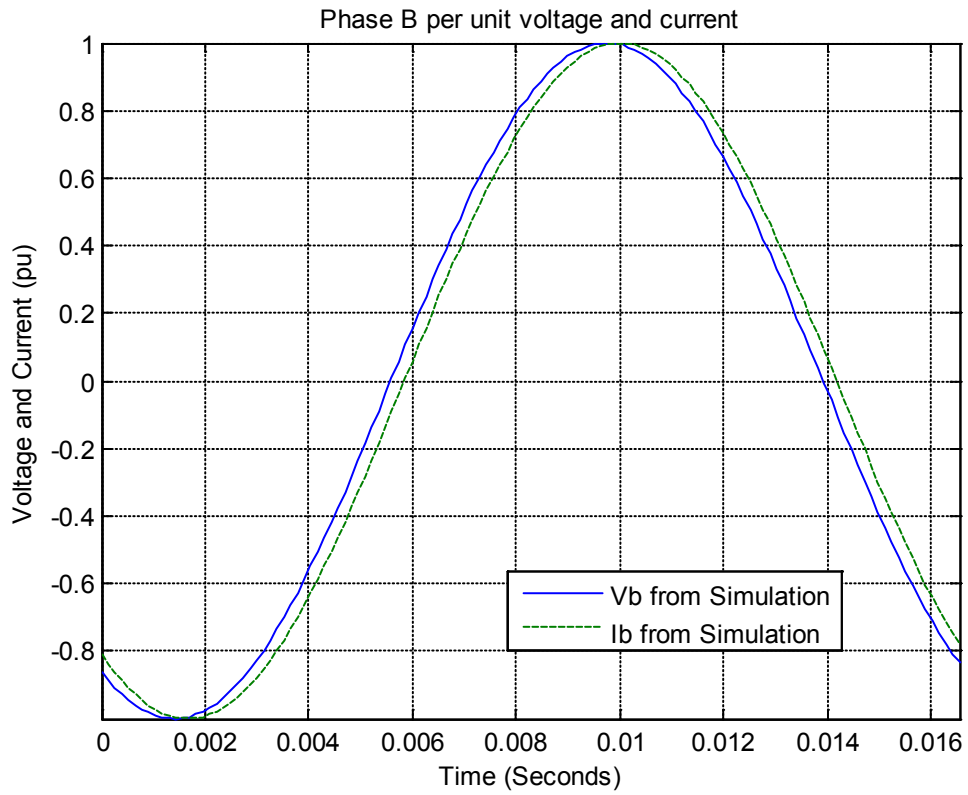


Figure 4.23: Phase B per unit voltage and current.

Phase C:

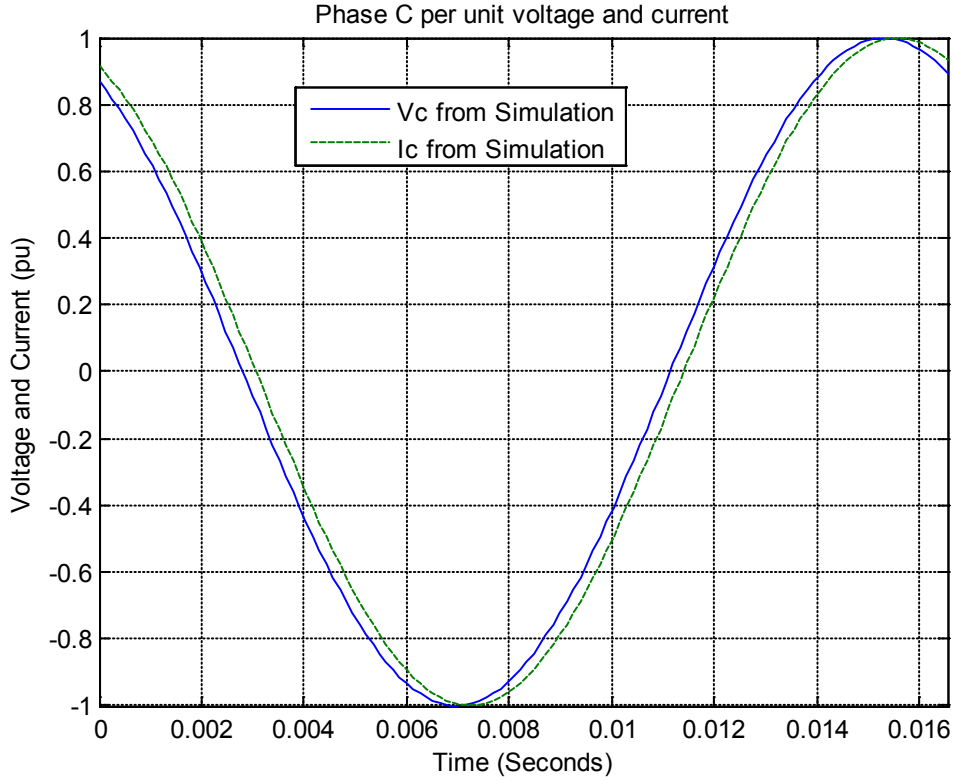


Figure 4.24: Phase C per unit voltage and current.

Here,

$$V_{rms} = 79.65 \text{ kV}$$

$$I_{rms} = 857.31 \text{ A}$$

$$V_{phase} - I_{phase} = +5.58^\circ$$

$$\text{Real Power} = 67.96 \text{ MW}$$

$$\text{Reactive Power} = 6.64 \text{ Mvar}$$

Thus, the total three-phase power supplied to the grid is given by:

$$\text{Total Real Power} = 68 + 67.99 + 67.96 = \mathbf{203.95 \text{ MW}}$$

$$\text{Total Reactive Power} = 6.66 + 6.65 + 6.64 = \mathbf{19.95 \text{ Mvar}}$$

The real and reactive power outputs from this calculation match the reference (desired) outputs. The calculations in the  $qd0$  domain are verified in the next subsection and the real and reactive power results are expected to be identical to the results from the phasor-domain calculations.

#### 4.4.1.2 Calculations in the $qd0$ Reference Frame

The following calculations are carried out in Matlab. The voltage  $V_{abc}$  and current  $I_{abc}$  extracted from the time-domain model are converted from values on the stationary  $abc$  frame to equivalent values on the rotating  $qd0$  reference frame. This is done using the Park Transform shown below:

$$T_{qd0} = \frac{2}{3} \begin{bmatrix} \cos\theta_q & \cos(\theta_q - 120^\circ) & \cos(\theta_q + 120^\circ) \\ \sin\theta_q & \sin(\theta_q - 120^\circ) & \sin(\theta_q + 120^\circ) \\ \frac{1}{2} & \frac{1}{2} & \frac{1}{2} \end{bmatrix} \quad (4.55)$$

where  $\theta_q$  is the angle measured from the positive stationary  $a$ -axis to the rotating  $q$ -axis. The transformation equations used are [54]:

$$\overline{V_{qd0s}} = \overline{T_{qd0}} \cdot \overline{V_{abcs}} \quad (4.56)$$

$$\overline{I_{qd0s}} = \overline{T_{qd0}} \cdot \overline{I_{abcs}} \quad (4.57)$$

The real and reactive power in the stator are calculated using Equations 4.37 and 4.38 in the previous section. They are reproduced below.

$$P_s = \frac{3}{2} (V_{ds} i_{ds} + V_{qs} i_{qs}) \quad (4.58)$$

$$Q_s = \frac{3}{2} (V_{ds} i_{qs} - V_{qs} i_{ds}) \quad (4.59)$$

The results obtained for real and reactive power are:

**Total Real Power = 204 MW**

**Total Reactive Power = 19.9856 Mvar**

Based on these values, the error between the phasor-domain and  $qd0$ -domain calculation methods is less than 0.2%. This validates the use of the power calculation method using the  $qd0$  reference frame.

#### 4.4.2 Wind Power Curve

The rated wind speed of the turbines used in the WPP is 13 m/s. This means that when the wind-speed is 13 m/s, the WPP generates the rated real power (204 MW). The cut-in speed for the turbines is 6 m/s. This is the minimum speed required for the wind turbine to start generating power. The wind turbine cut-out speed is 20 m/s. This is the speed above which damage can occur to the turbine and hence, when the wind speed is above cut-off, the turbine is shut down by the application of brakes. In this section, we evaluate the wind turbine over the gamut of its wind speed range. The expected power outputs for a DFIG WPP over different speed ranges is tabulated below in Table 4.3.

*Table 4.3: Real power output for various wind speed ranges.*

Wind Speed Range	Real Power Generated by Turbine
Below cut-in speed	Zero output power
Between cut-in and rated speeds	Power generated is maximum extractable from the wind
Between rated and cut-out speeds	Power generated is the rated output of the wind plant
Above cut-out speed	Zero output power

For wind speeds greater than or equal to the rated speed, the DFIG WPP should give a constant power output, which is the rated power. This is accomplished by the pitching of the turbine blades when the wind speed goes above rated speed. The maximum pitch has been limited to 30 degrees because for pitch angles above this value the  $C_p$  curve of the turbine causes the aerodynamic power extractable from the wind to be less than the rated value. Also, values of pitch above 30 degrees would be required only for wind speeds above 20 m/s, which is the cut-off speed. This may be seen in Table 4.5. The turbine is not run above cut-out speed, although theoretically it can be accomplished in the simulation, the turbine would be turned out of the wind and brakes would be applied if a similar situation occurred in real life. The time-domain model is run with the set of parameters shown below in Table 4.4. All these parameters are held constant throughout the simulation. The time-domain model is run with wind speed equal to 6 m/s. The generated real power  $P$ , generated reactive power  $Q$  and the pitch angle are

measured and tabulated in Table 4.5. The maximum available power from the wind is also calculated and tabulated for comparison with the generated real power. The wind speed is varied from 6 m/s to 20 m/s in steps of 1m/s and the above process is repeated after each simulation.

*Table 4.4: Time-Domain Model Parameters for Wind Power Curve.*

$V_{source}$ kV rms LL	$P_{rated}$ MW	$Q_{genRef}$ MVAR
138	204	20

*Table 4.5: Power generated for various wind speeds*

<i>Wind Speed</i> m/s	$P_{measured}$ MW	<i>Extractable <math>P_{aero}</math></i> MW	$Q_{measured}$ MVAR	<i>Pitch angle</i> degrees
6	20.38	20.06	19.99	0
7	31.85	31.85	19.99	0
8	47.54	47.54	20.38	0
9	67.69	67.69	19.99	0
10	92.85	92.85	19.98	0
11	123.59	123.59	19.99	0
12	160.45	160.45	19.98	0
13	204	204	19.99	0
14	204	254.79	19.98	8.81
15	204	313.38	19.99	14.07
16	204	380.33	19.98	18.47
17	204	456.19	19.99	22.31
18	204	541.52	19.98	25.76
19	204	636.88	19.99	28.92
20	204	742.83	19.99	31.86

From Table 4.5, it is seen that the experimental results from the time-domain model closely match the theoretical results for aerodynamic power extractable from the wind, for wind speeds below rated speed. This shows that the real power controller is functioning optimally. The reactive power is held virtually constant, verifying that a change in the real power output does not cause a change in reactive power output. This hints that the real power and reactive power control are decoupled, but this can only be confirmed if the reactive power controller is shown to have no effect on real power output. The real power and pitch are plotted versus the wind speed in Figures 4.25 and 4.26.

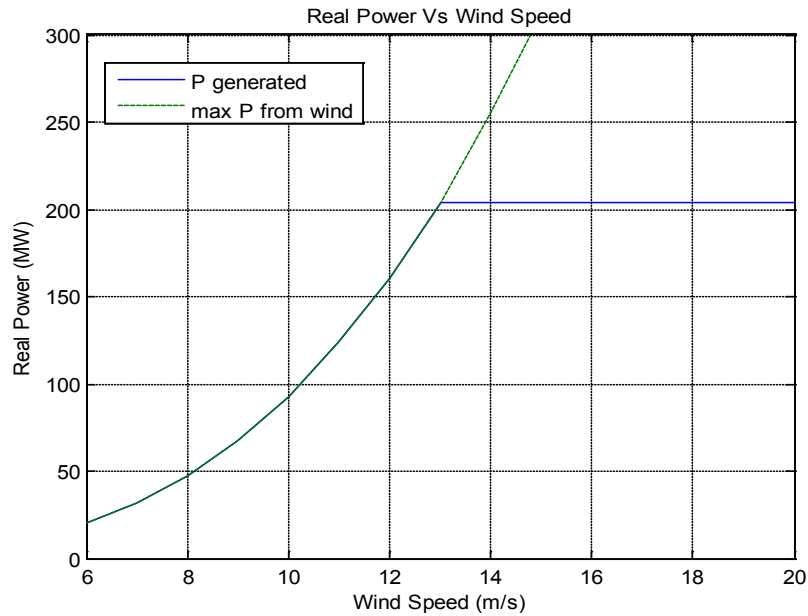


Figure 4.25: Real Power (MW) vs. Wind Speed(m/s) curve.

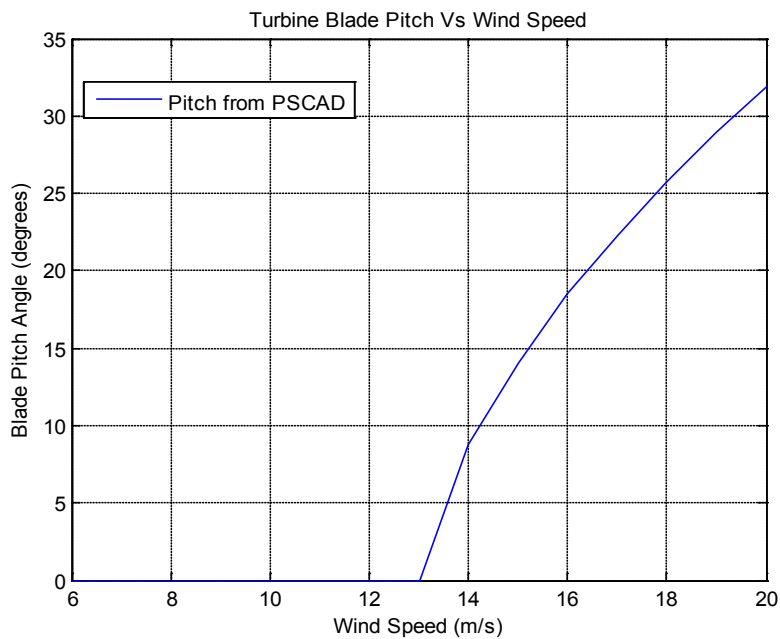


Figure 4.26: Pitch Angle (degrees) vs. Wind Speed (m/s) curve.

#### 4.4.3 Reactive Power Control and Less-Than-Maximum Power Output

In this section, the effects change in reactive power demand on the performance of the time-domain model is observed while keeping the wind speed at the rated value of 13 m/s. The ability of the controller to extract less than the aerodynamic extractable power from the wind (governor action) is also examined. The source voltage and wind speed parameters are held constant throughout the simulation in this section. To simulate governor action and thus, change the amount of maximum real power extractable from the wind, the value of the parameter  $P_{set}$  is changed in the pitch control model (see previous section). This parameter can be changed only at the beginning of the simulation; hence, true governor action cannot be simulated. Changes later on in the simulation are observed to have no effect on the output.

Table 4.6: Parameters held constant.

$V_{source}$ kV rms LL	Wind Speed m/s
138	13

Two cases are simulated. For the first case (Case P-1, where “P” stands for Performance Test),  $P_{set}$  is set equal to 1 pu, corresponding to 100% of extractable power being extracted, which causes the WPP to generate real power equal to the its rated MW capacity which is 204 MW. With the WPP operating at this rated power output, the reactive power demand parameter  $Q_{genRef}$  is changed in the Reactive Power Control Model (see previous section). This case is used to determine if the reactive power controller is working correctly and is achieving the output of demanded reactive power. Also, if the reactive power controller’s operation is shown to have no effect on the real power output, we can confirm that the real power and reactive power controllers are indeed decoupled. The output for this case is shown in Figure 4.27.

For the second case (Case P-2),  $P_{set}$  is set equal to 0.8 pu, corresponding to 80% of extractable power being extracted. The expected power output of the WPP is 163.2 MW (80% of 204 MW). The reactive power demand is changed during the run. This case is used to determine if the change in  $P_{set}$  produces the expected result, and if the change in reactive power (while  $P_{set}$  is set to less than unity) is different from when  $P_{set}$  is unity. The output for this case is shown in Figure 4.28.

Cases P-1 and P-2 are shown in Table 4.7 below. In the table, the parameter values for changes made to reactive power demand (while wind speed is held constant) are shown for both cases. During simulation, a steady-state is reached at 80 seconds. For each case, the required reactive power is then changed from its initial to final value in Table 4.7 at time  $t=90s$ . The results are shown below in Figures 4.27 and 4.28.

Table 4.7: Parameters for Time-Domain Model for Reactive Power Control Test: Real Power Setpoint and Reactive Power Demand.

Case	$P_{set}$ pu (MW)	Initial $Q_{genRef}$ MVAR	Final $Q_{genRef}$ MVAR
P-1	1 (204)	0	-10
P-2	0.8 (163.2)	0	10

In Figure 4.27, the real and reactive power variation during a change in reactive power demand is shown. The reactive power demand is changed from 0 Mvar to -10 Mvar at time  $t=90s$ . The wind speed (and hence the demand real output power) is kept constant. It can be seen that the change in reactive power demand causes the reactive power controller to change the reactive power output to the desired value, and it eventually achieves this value at time  $t=180s$ . The active power output remains unchanged during the change in reactive power, suggesting that the real and reactive power controllers are decoupled. In case P-2, the value of  $P_{set}$  is set to 0.8 pu, and the real power output from Figure 4.28 shows that this is correctly achieved. Again, the change in reactive power from 0 Mvar to 10 Mvar at  $t=90s$  is shown to have no effect on the real power output. The behavior of the real and reactive power controllers remains decoupled. The figures show that the simulation result from the time-domain model matches the theoretical result. For a given constant wind speed,  $P_{set}$  must not be set to such a value so as to try and generate power beyond the maximum power extractable from the wind at that fixed speed. For the above cases, 13 m/s was the fixed wind speed. Change in reactive power had no effect on the real power output in either case, and the reactive power controller was observed to be working as expected.

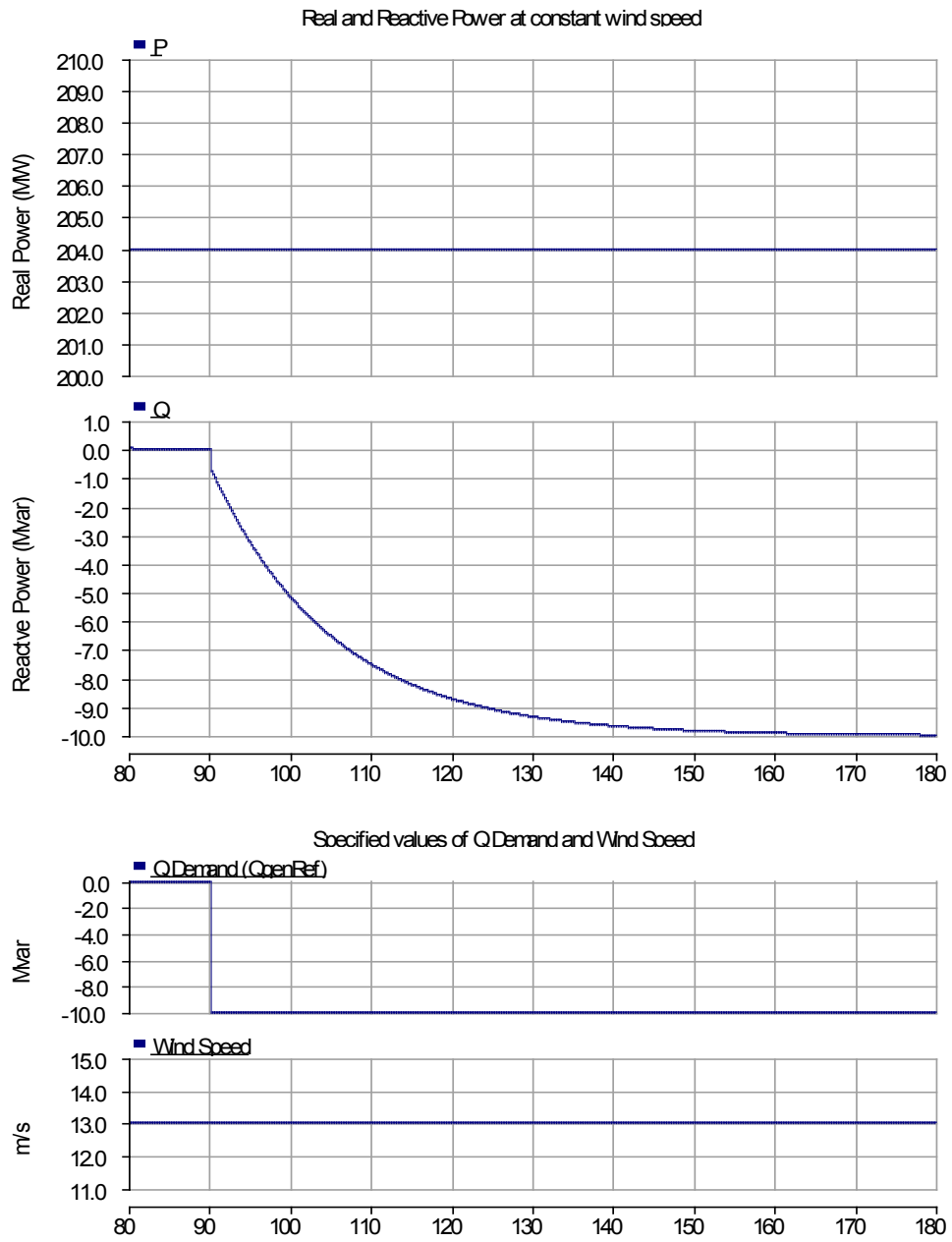


Figure 4.27: Case P-1: Real and Reactive Power Output.

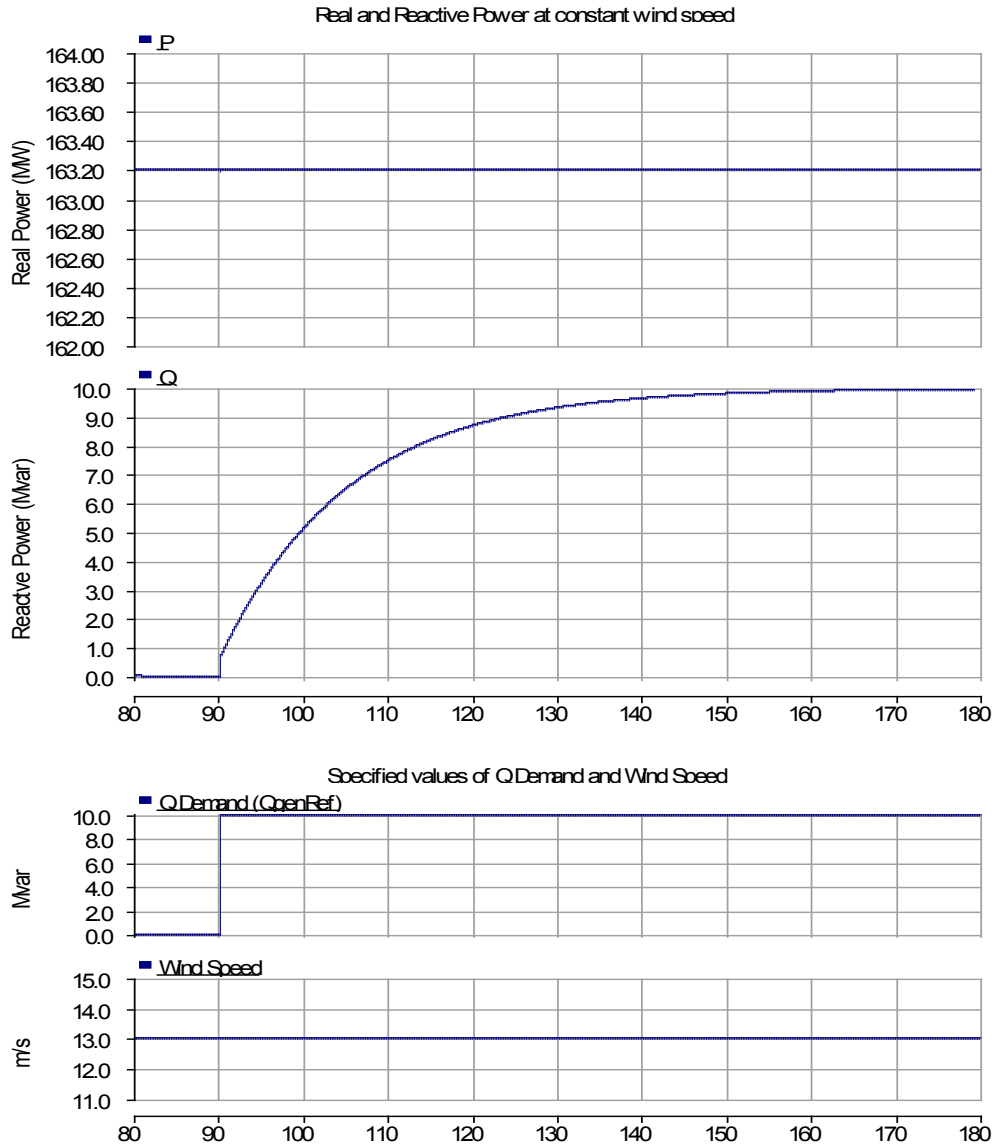


Figure 4.28: Case P-2: Real and Reactive Power Output.

#### 4.4.4 Changes in Wind Speed

In this section, the reactive power demand is kept constant,  $P_{set}$  is set to unity and the wind speed is varied. The time-domain model should maintain values as shown in Table 4.5. The initial and final values are set according to Table 4.8 and 4.9. Steady-state is reached at 80 seconds. Once steady-state is achieved, a disturbance in wind speed can be applied. The simulation results are shown in Figures 4.29 and 4.30. The lower part of each figure shows the changes in control values, while the upper part shows the changes in output real and reactive power.

Table 4.8: Parameters Which Remain Constant for Wind Speed Change Test.

$V_{source}$ kV rms LL	$P_{rated}$ MW	$Q_{genRef}$ MVAR	Wind Speed m/s
138	204	0	13

Table 4.9: Parameters for Time-Domain Model for Reactive Power Control Test.

Case	Initial $V_{wind}$ m/s	Final $V_{wind}$ m/s	New Power Output MW
P-3	13	16	204
P-4	13	11	123.59

Figure 4.29 depicts Case P-3 wherein the real and reactive power variation during an increase in wind speed is shown. In the time-domain model, the wind speed is changed from 13 m/s (rated) to 16 m/s (above rated) at time  $t=90$ s. The demanded reactive output power is kept constant. Observe that the change in wind speed caused the real power controller in the time-domain model to change the real power output to a higher-than-rated value only briefly (a few seconds) before the output is once again lowered to rated real power. This is as expected, and the behavior of the model is consistent with that of real-world DFIG WPPs.

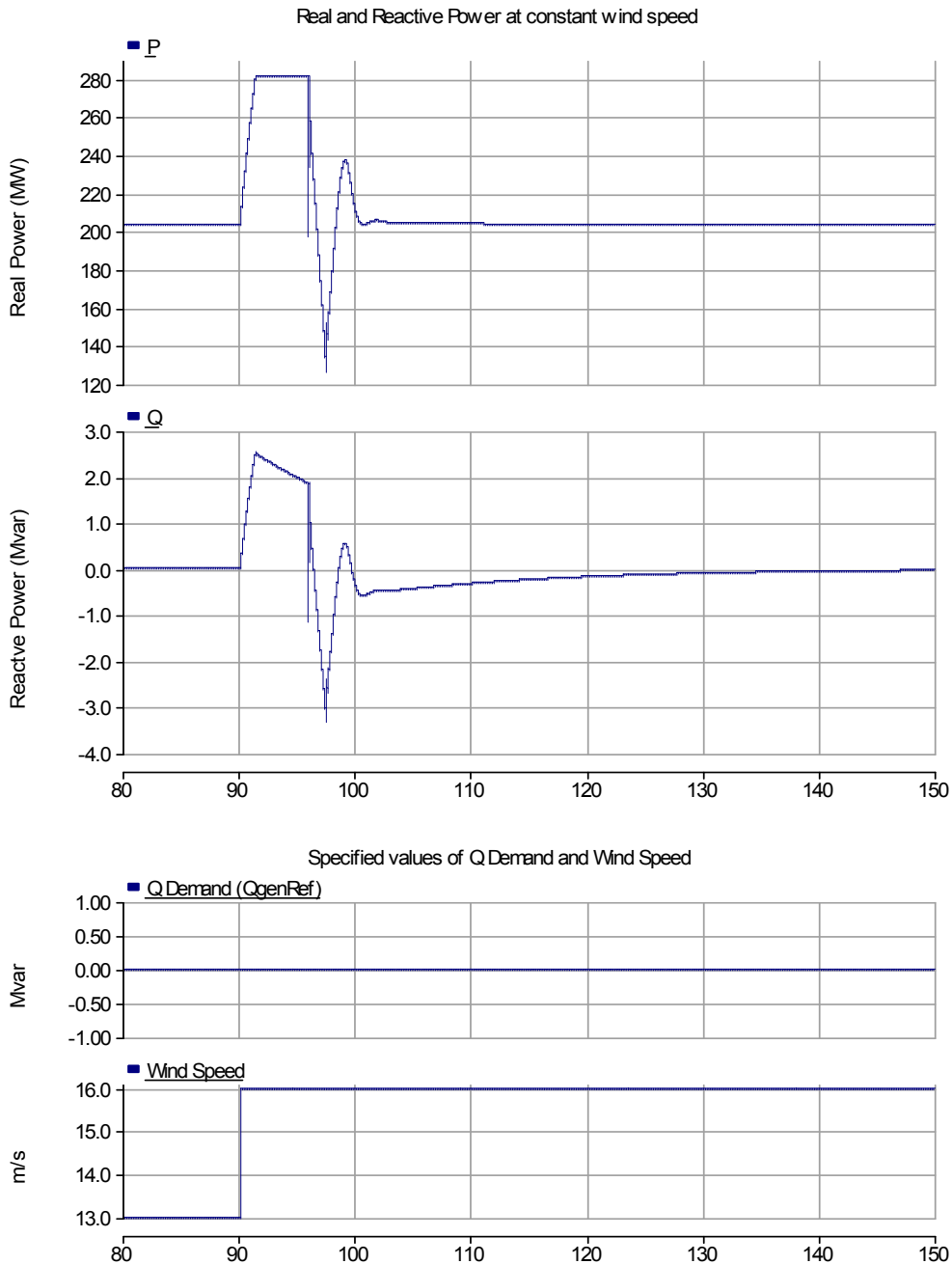


Figure 4.29: Case P-3: Effect of change in wind speed to higher than rated.

Figure 4.30 depicts Case P-4 and shows the change in real and reactive power output when the wind speed drops from 13 m/s (rated) to 11 m/s (below rated). The simulation of the time-domain model shows that the real power output changes from rated power to maximum extractable power at 11 m/s i.e.,  $123.59 \text{ MW} = 204 \left(\frac{11}{13}\right)^3 \text{ MW}$ .

Reactive power output shows the same behavior as in Figure 4.29. This too is similar to the behavior of real-world DFIG WPPs. The reactive power output in both cases remains (relatively) unchanged during the change in reactive power, showing a variation that is an order of magnitude smaller than the real power variation. This suggests that the real and reactive power controllers are indeed decoupled.

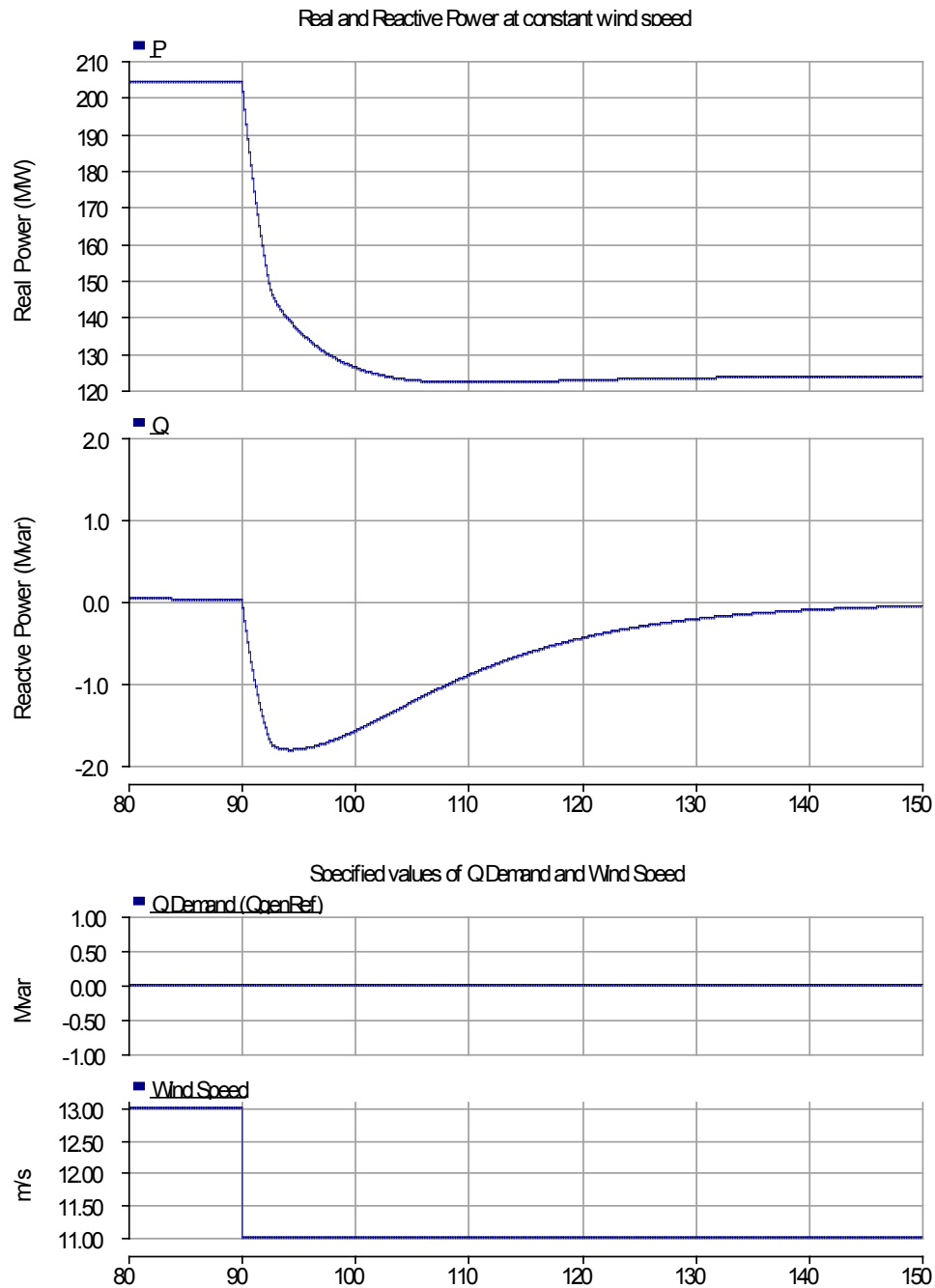


Figure 4.30: Case P-4: Effect of change in wind speed to lower than rated.

#### 4.4.5 Model Performance Summary

Some basic questions about the performance of the time-domain model have been addressed in this section. The model was shown to provide a good approximation of real-world DFIG WPP behavior during steady-state and quasi-steady-state operation. The claim made in the previous section that the real and reactive power could be

controlled independently has also been verified. The next step is to study the time-domain DFIG WPP model's response during fault conditions. The validation of the model using available fault data from an actual WPP is described in the next section.

## 4.5 Three-Phase Model: Validation Using Field Data

This section describes the validation of the time-domain DFIG WPP model developed in PSCAD/EMTDC. The aim of the validation process is to demonstrate that the time-domain model does indeed behave like a real-world DFIG WPP, especially during fault conditions. The validation process showed that the time-domain model results matched the real-world results closely during steady-state and dynamic stability conditions. The validation process and the results are discussed in the following subsections. The data used for validation has been obtained from field data recorders at the point of interconnection of the aforementioned Taiban Mesa wind power plant.

### 4.5.1 Introduction to the Validation Process

For the purpose of validating real and reactive power response during a fault event, it is necessary to include a model of the collector system. The collector system model is connected at the WPP terminals to form a combined collector and WPP model. A variable voltage source capable of inputting unbalanced voltages into the combined collector and WPP model is used to replace the infinite bus.

Three fault cases are used to test the time-domain DFIG WPP model. For each case, actual data for three-phase voltages and currents at the bus where the collector system is connected to the grid has been provided in the data from the real-world WPP. Also, in each case, the reactive power demand was set to zero, but the real power (dependent on the wind speed) was set to a different constant value. To validate if the time-domain model is accurate, the three-phase actual voltage data is fed into the time-domain model using the variable voltage source and the resulting three-phase currents at the bus are extracted from the time-domain model. The extracted current data is compared with the actual current data and to see if they match closely, a MATLAB script developed for the purpose is used to calculate the real and reactive power flows at the bus, using:

- the actual three phase voltage and current data to get one real and reactive power dataset (dataset 1), and,
- the three-phase voltage and extracted current from the time domain simulation to get another real and reactive power dataset (dataset 2).

The MATLAB script uses the  $qd0$ -domain calculation method described earlier to calculate real and reactive power flows through the bus from the voltage and current at the bus. The real and reactive power datasets 1 and 2 are plotted and compared by visual inspection. If the match between the two datasets is good, the model is considered to be validated. A flowchart detailing the validation process is shown in Figure 4.31. The time-domain model was successfully validated using this process.

### 4.5.2 Collector System

A WPP is connected to the grid through a collector system, which typically consists of the following passive elements:

- Individual generator transformers (usually pad-mounted units at the base of each turbine) that step up voltage from the below 1-kV level at the generator to medium-voltage levels (34.5 kV is typical).
- Medium-voltage underground cables connecting the turbine rows.
- Medium-voltage overhead lines from the turbine rows to the main substation.
- Step up transformer(s) at the main substation that raise the voltage to transmission levels.

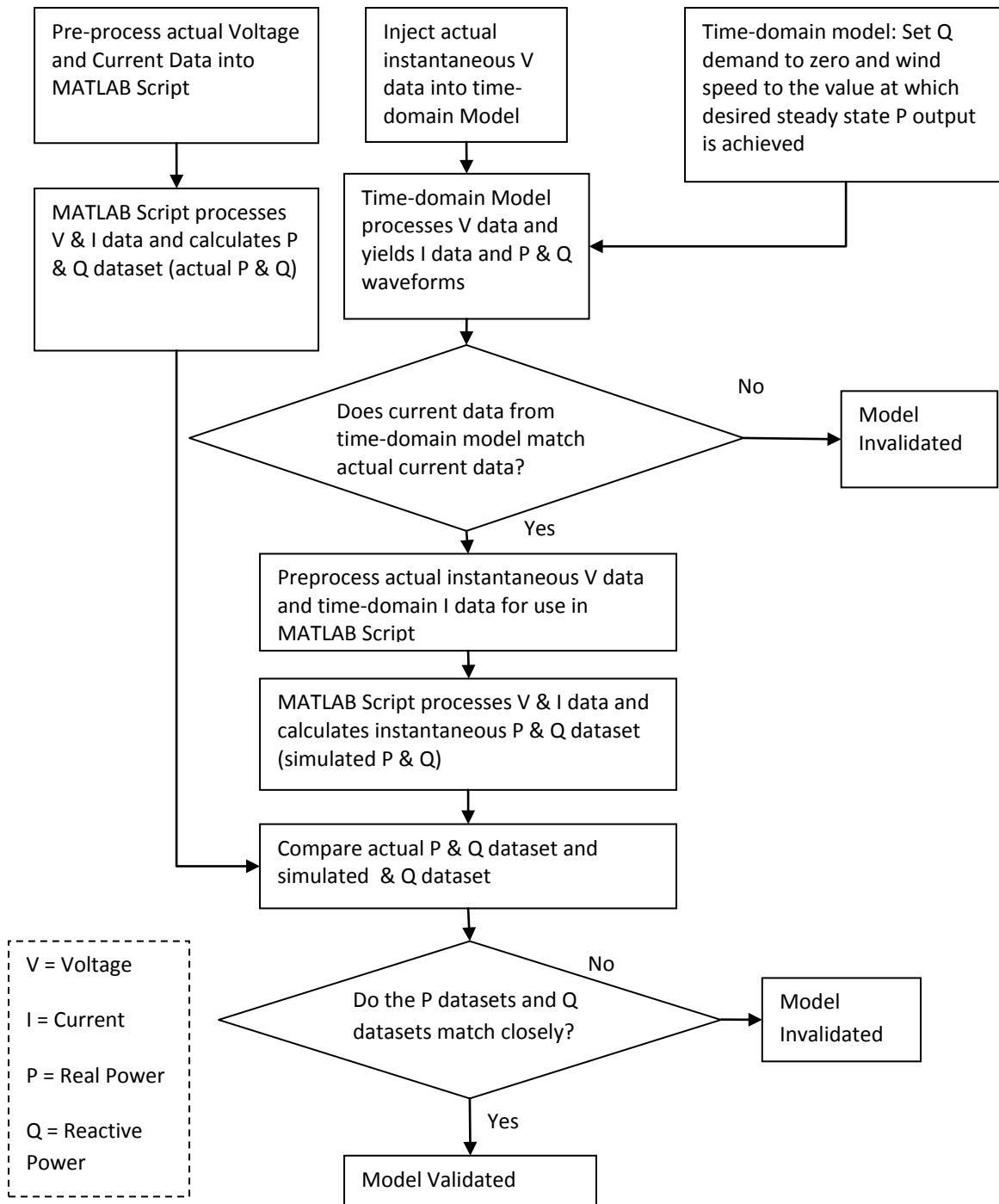


Figure 4.31: Validation Procedure Flowchart.

Reactive power compensation may be provided at the main substation. A transmission line connects the collector system to the grid. The point where the collector system connects to the grid is known as the Point of Interconnection or POI. To accurately model the behavior of the DFIG WPP during fault conditions, the collector system was included in the time-domain model. For the time-domain model, the unit transformers were lumped and modeled as one transformer, and the cables connecting the turbine rows were also lumped and modeled as one impedance element. The collector system model is shown in Figure 4.32. This approximation as lumped element is done since the DFIG WPP model represents an entire multi-turbine wind farm as a single machine, and the collector system has to be connected to the terminals of this single machine.

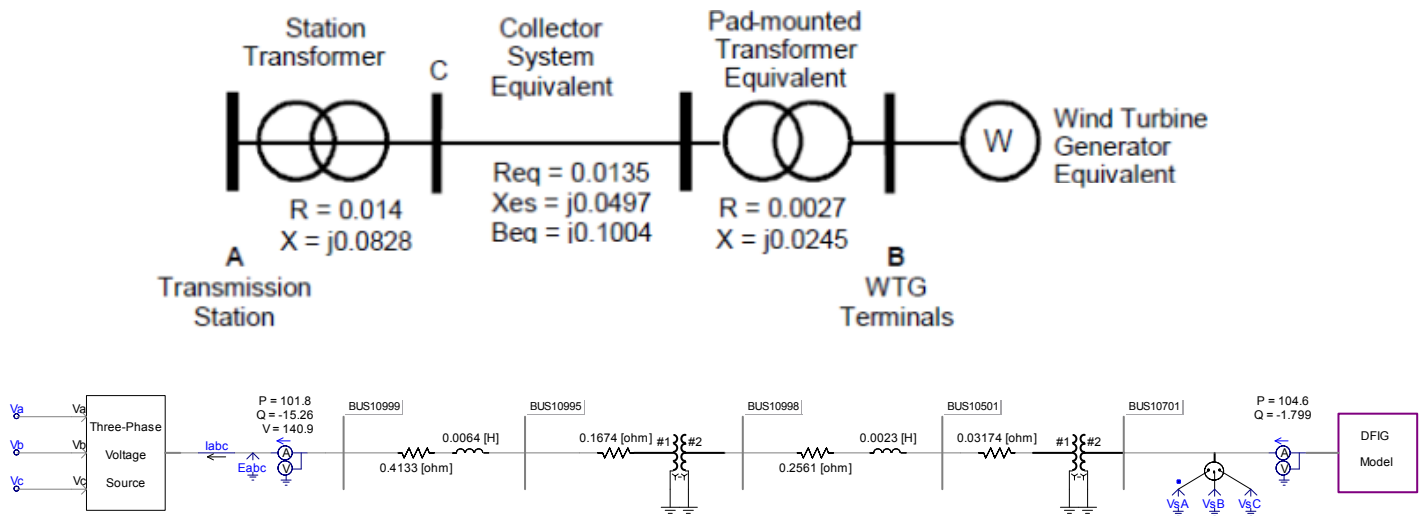


Figure 4.32: Collector System Schematic & Time-Domain Model Collector System.

### 4.5.3 Steady-State Validation: Pre-Fault

Before assessing the time-domain model's performance during fault conditions, the steady-state performance of the model has to be evaluated. The steady-state behavior of the time-domain model should match that of the actual real-world DFIG WPP from which the data has been obtained. As mentioned before, the actual data contains three-phase voltage and currents at the POI bus for three different fault conditions. The pre-fault voltage and current data for a short time interval (approximately 25 ms) is also available for each case. This pre-fault data represents the steady-state voltages and currents at the POI. Comparison of the actual pre-fault data with the pre-fault data from the time-domain simulation can thus be used to validate the steady-state performance of the time-domain model. The MATLAB script mentioned earlier was used to process the pre-fault voltage and current data and get real and reactive power flows. All three cases were used for the validation.

The results from the time-domain model matched the results calculated from the actual data in each case and the model was validated. The first stage of the validation was to calculate the pre-fault real and reactive power for each phase in the phasor-domain using one cycle of pre-fault voltage and current from the actual data. This gave us an initial estimate to compare the time-domain model output with. For each phase, one cycle of pre-fault data was extracted. The current and voltage waveforms were inspected to see if current lags or leads the voltage, and the phase angle between the two waveforms was determined. Next, the RMS values of voltage and current were determined by finding the peak values of the waveforms and dividing by the square root of two. This calculation requires us to assume that there are no harmonic distortions in the current and voltage waveforms. While this assumption is true here since the system is in steady-state, a more general and reliable method of calculating magnitude and phase of a signal is to perform a Fast-Fourier Transform (FFT) on it.

Results from the FFT method were compared to those from the phasor-domain method and were found to be almost identical. Steady-state real and reactive power was calculated using the RMS values of voltage and current and the phase difference between the two waveforms. The three-phase real power is the summation of the real powers of each phase and the three-phase reactive power is the summation of the reactive powers of each phase. Since the system is in steady state and the voltages are balanced, one phase data is sufficient to perform the calculations, as the real and reactive power contribution from each phase is identical.

#### 4.5.3.1 Case V-1 (Validation Case 1)

For Case V-1, one cycle of the steady state voltage and current for phase a is shown in Figure 4.33. The figure shows that the current waveform is leading the voltage waveform by 8.96 degrees. We can employ the same phasor domain

calculations and the same sign convention used in the previous section to determine the real and reactive power magnitude and direction of power flow. The sign convention used in the previous section is to consider real and reactive power flowing out of the WPP model to be positive and into the WPP model be negative. In Figure 4.32, it can be seen that the ammeter direction is such that current into the grid is considered positive.

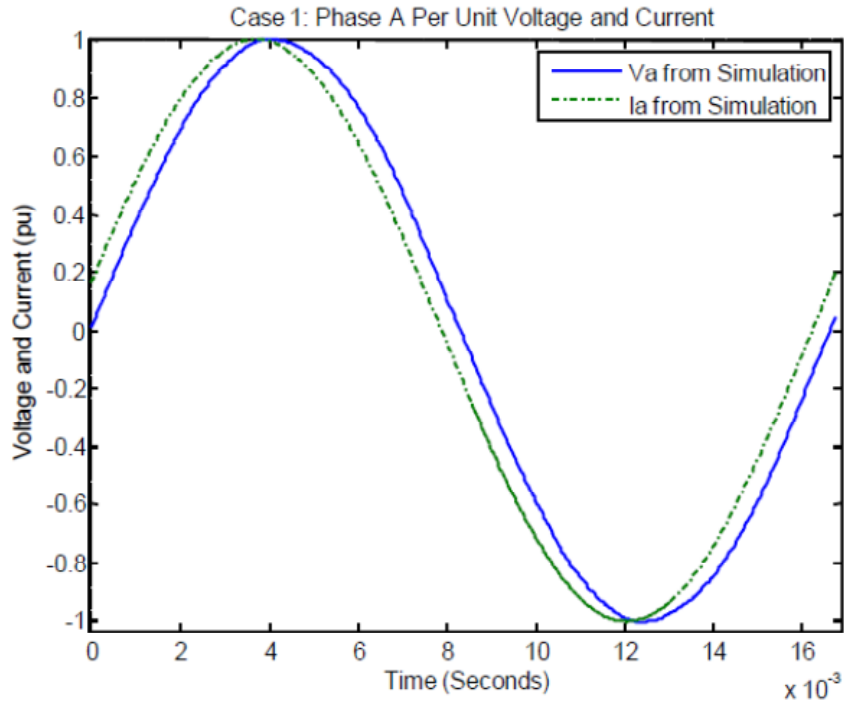


Figure 4.33: Case V-1: One cycle of pre-fault voltage and current data for phase A.

The calculations for phase *A* may be performed as follows:

$$V_{rms} = 80.74 \text{ kV}$$

$$I_{rms} = 559.38 \text{ kA}$$

$$V_{phase} - I_{phase} = -8.96^\circ$$

$$\text{Real Power} = V_{rms} \times I_{rms} \times \cos(V_{phase} - I_{phase}) = 44.61 \text{ MW}$$

$$\text{Reactive Power} = V_{rms} \times I_{rms} \times \sin(V_{phase} - I_{phase}) = -7.03 \text{ Mvar}$$

Since the voltages and currents are balanced in steady state, we can assume that the contribution to real and reactive power from phases B and C is the same as that from phase *A*. The three-phase real and reactive power output for case 1 can be calculated as:

$$\text{Three - Phase Real Power} = 3 \times 44.61 \text{ MW} = 133.84 \text{ MW}$$

$$\text{Three - Phase Reactive Power} = 3 \times -7.03 \text{ Mvar} = -21.10 \text{ Mvar}$$

Since the voltages and currents are balanced in steady state, we can assume that the contribution to real and reactive power from phases B and C is the same as that from phase *A*. The three-phase real and reactive power output for Case V-1 can thus be calculated as shown above. Once an estimate of the real and reactive power in

phasor-domain was obtained, the next stage of the validation was to use the MATLAB script to convert the actual data and time-domain model output data to the  $qd0$ -domain, process the data to find real and reactive power flows and plot them overlaid on one another. The results in Figures 4.34 and 4.35 show that the results from the actual data and the time-domain model match each other closely, as well as matching the estimate from the phasor-domain. The steady state operation of the time-domain is thus validated for Case V-1.

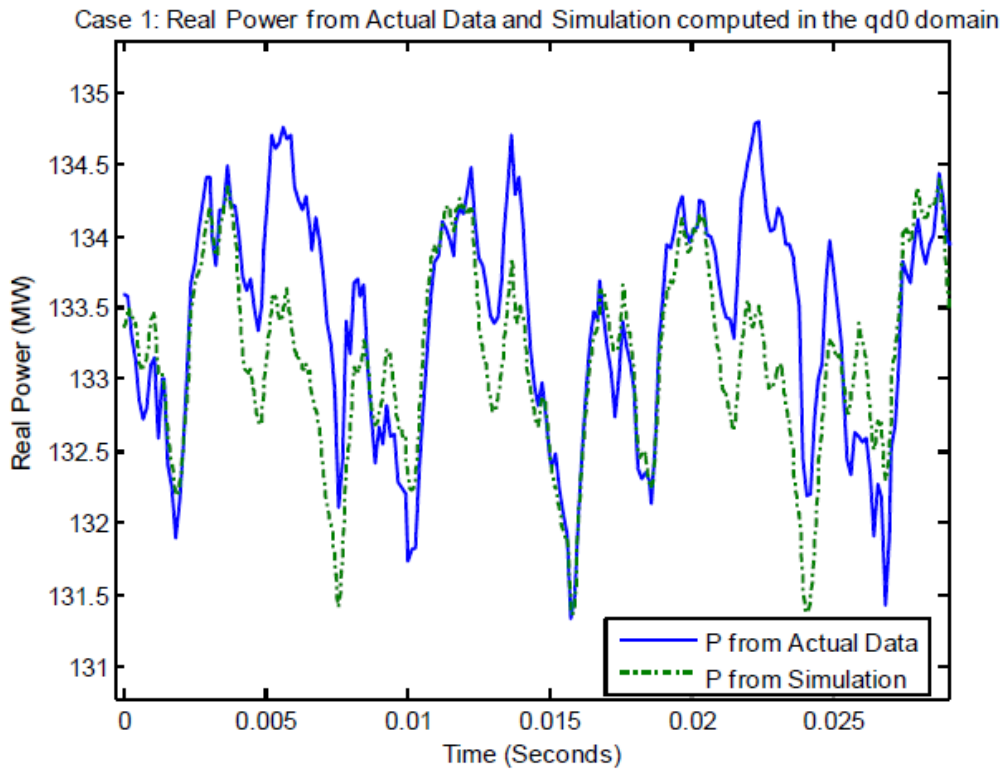


Figure 4.34: Case V-1: Real Power Comparison: Actual vs. Time Domain Model

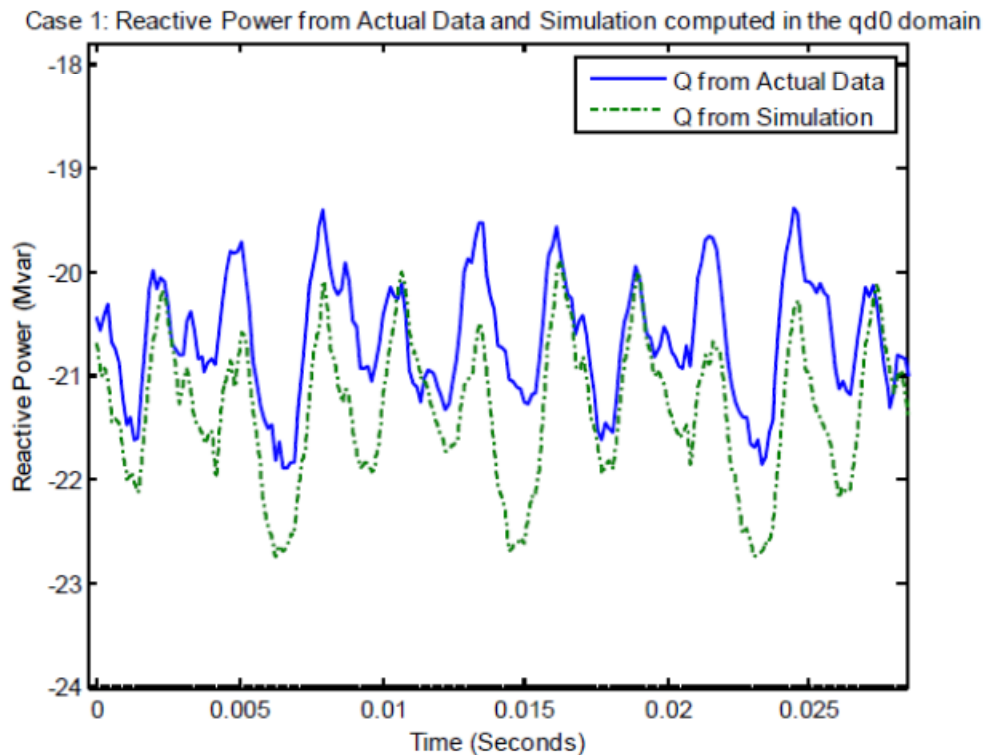


Figure 4.35: Case V-1: Reactive Power Comparison: Actual vs. Time Domain Model.

#### 4.5.3.2 Case V-2 (Validation Case 2)

A similar analysis as for Case V-1 was carried out for Case V-2. One cycle of steady state voltage and current data is shown in Figure 4.36. The calculations in phasor-domain for phase *A* were as follows:

$$V_{rms} = 81.85 \text{ kV}$$

$$I_{rms} = 477.20 \text{ A}$$

$$V_{phase} - I_{phase} = -6.59^\circ$$

$$\text{Real Power} = V_{rms} \times I_{rms} \times \cos(V_{phase} - I_{phase}) = 38.8 \text{ MW}$$

$$\text{Reactive Power} = V_{rms} \times I_{rms} \times \sin(V_{phase} - I_{phase}) = -4.48 \text{ Mvar}$$

The three-phase real and reactive power output for case 1 can once again be calculated as:

$$\text{Three - Phase Real Power} = 3 \times 38.8 \text{ MW} = 116.4 \text{ MW}$$

$$\text{Three - Phase Reactive Power} = 3 \times -4.48 \text{ Mvar} = -13.45 \text{ Mvar}$$

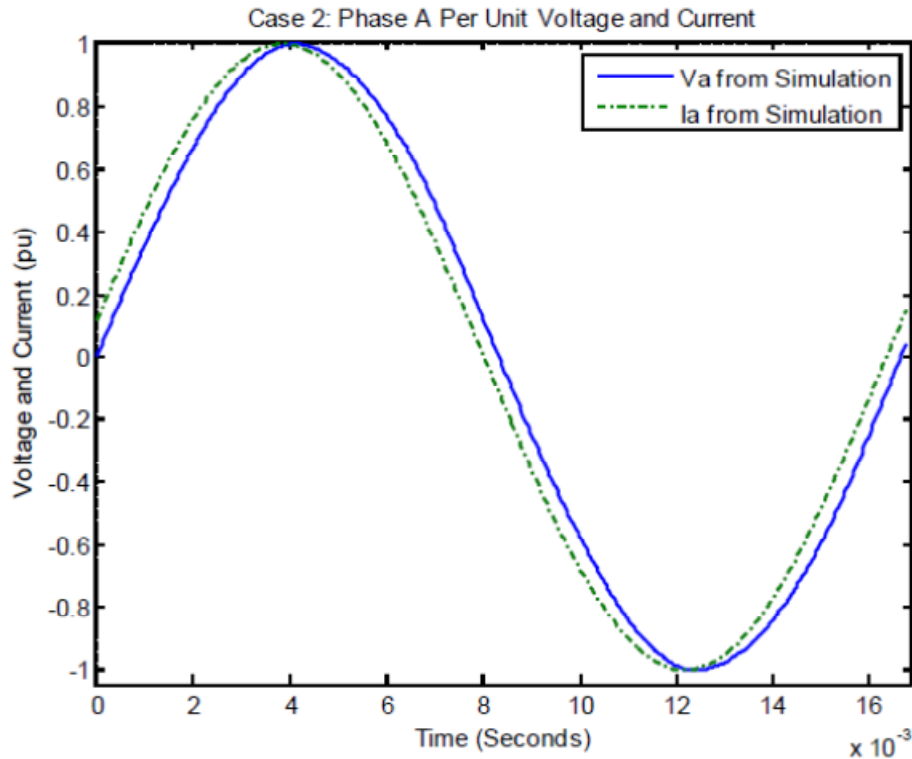


Figure 4.36: Case V-2: One cycle of pre-fault voltage and current data for phase A.

Once again, the MATLAB script was used to convert the actual data and time-domain model output data to the *qd0*-domain, process the data to find real and reactive power flows, and plot them overlaid on one another. The results in Figures 4.37 and 4.38 show that the results from the actual data and the time-domain model match each other closely, as well as matching the estimate from the phasor-domain. The steady-state operation of the time-domain is thus validated for Case V-2.

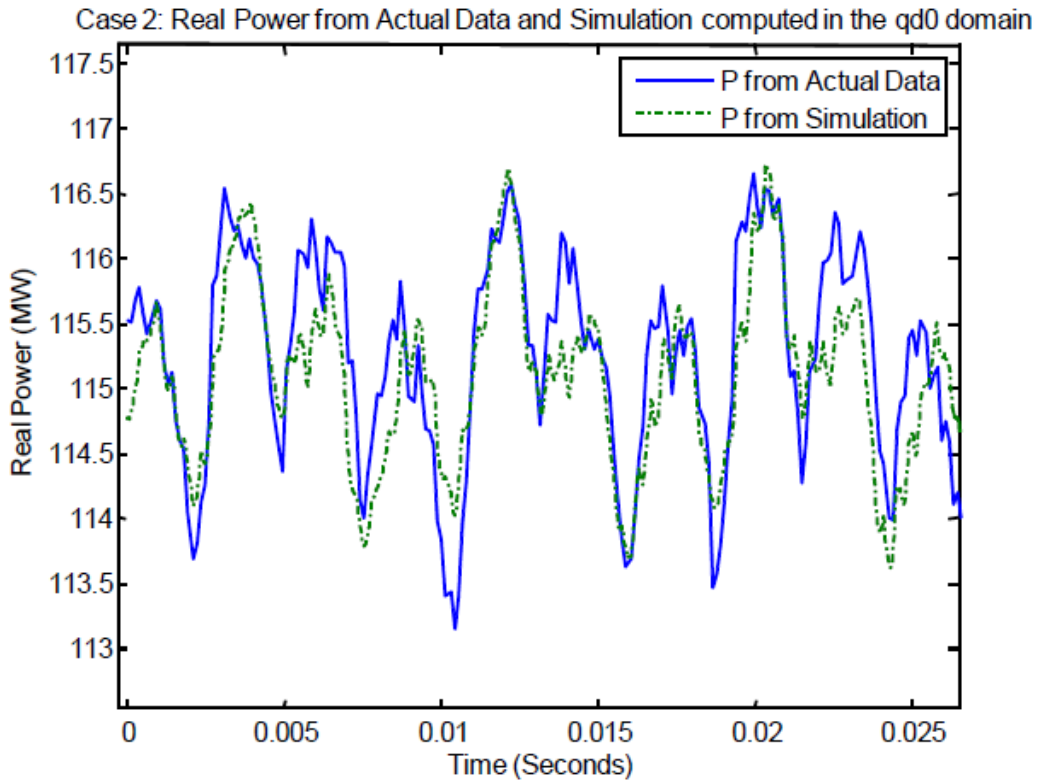


Figure 4.37: Case V-2: Real Power Comparison: Actual vs. Time Domain Model.

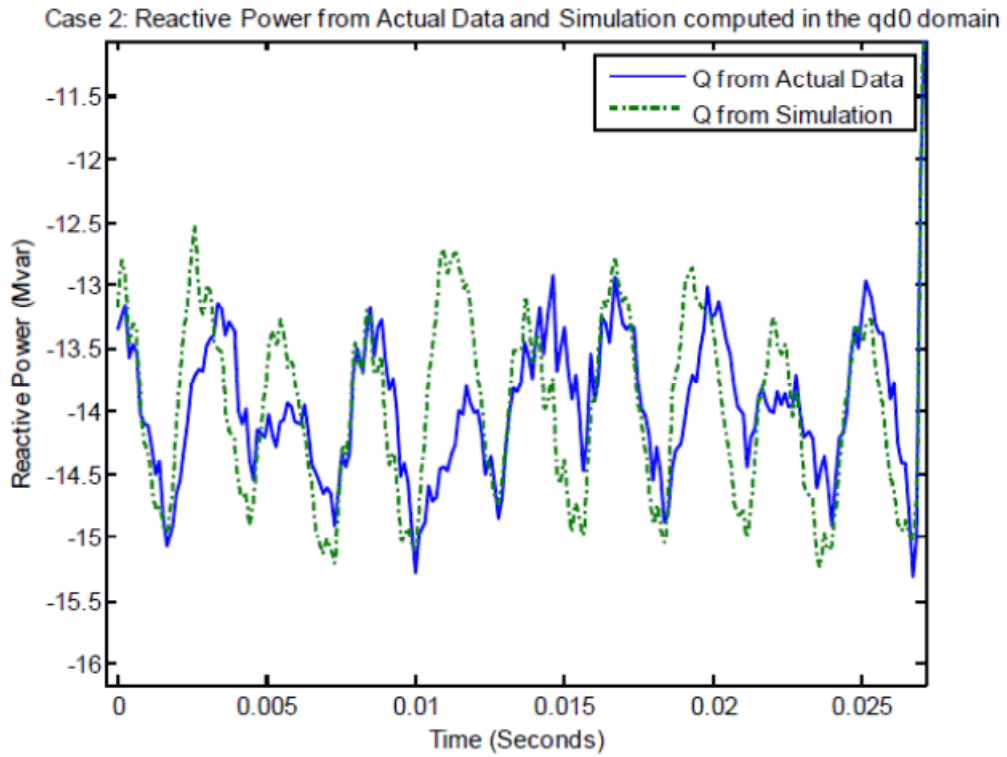


Figure 4.38: Case V-2: Reactive Power Comparison: Actual vs. Time Domain Model.

#### 4.5.3.3 Case V-3 (Validation Case 3)

A similar analysis as for Case V-1 and Case V-2 was carried out for Case V-3. One cycle of steady-state voltage and current data is shown in Figure 4.39. The calculations in phasor-domain for phase *A* were as follows:

$$V_{rms} = 81.77 \text{ kV}$$

$$I_{rms} = 426.94 \text{ A}$$

$$V_{phase} - I_{phase} = -8.56^\circ$$

$$\text{Real Power} = V_{rms} \times I_{rms} \times \cos(V_{phase} - I_{phase}) = 34.52 \text{ MW}$$

$$\text{Reactive Power} = V_{rms} \times I_{rms} \times \sin(V_{phase} - I_{phase}) = -5.20 \text{ Mvar}$$

The three-phase real and reactive power output for case 1 can once again be calculated as:

$$\text{Three - Phase Real Power} = 3 \times 34.52 \text{ MW} = 103.57 \text{ MW}$$

$$\text{Three - Phase Reactive Power} = 3 \times -5.20 \text{ Mvar} = -15.59 \text{ Mvar}$$

Once again, the MATLAB script was used to convert the actual data and time-domain model output data to the qd0-domain, process the data to find real and reactive power flows and plot them overlaid on one another. The results in Figures 4.40 and 4.41 show that the results from the actual data and the time-domain model match each other closely, as well as matching the estimate from the phasor-domain. The steady state operation of the time-domain is thus validated for Case V-3.

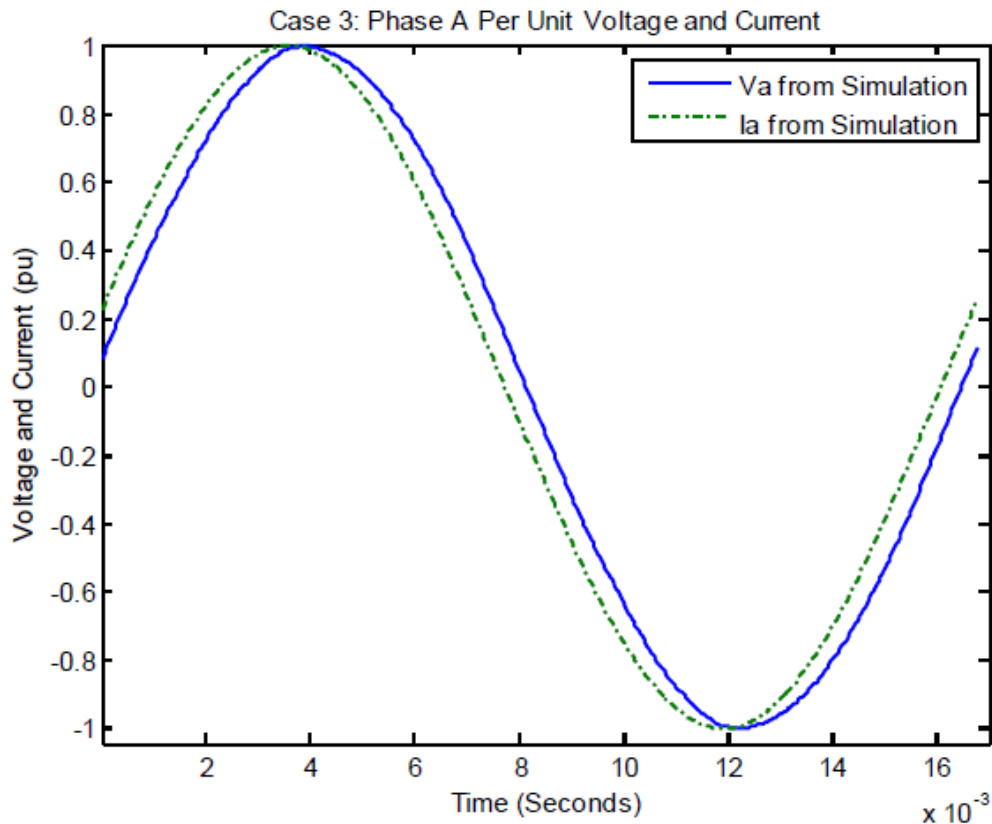


Figure 4.39: Case V-3: One cycle of pre-fault voltage and current data for phase A.

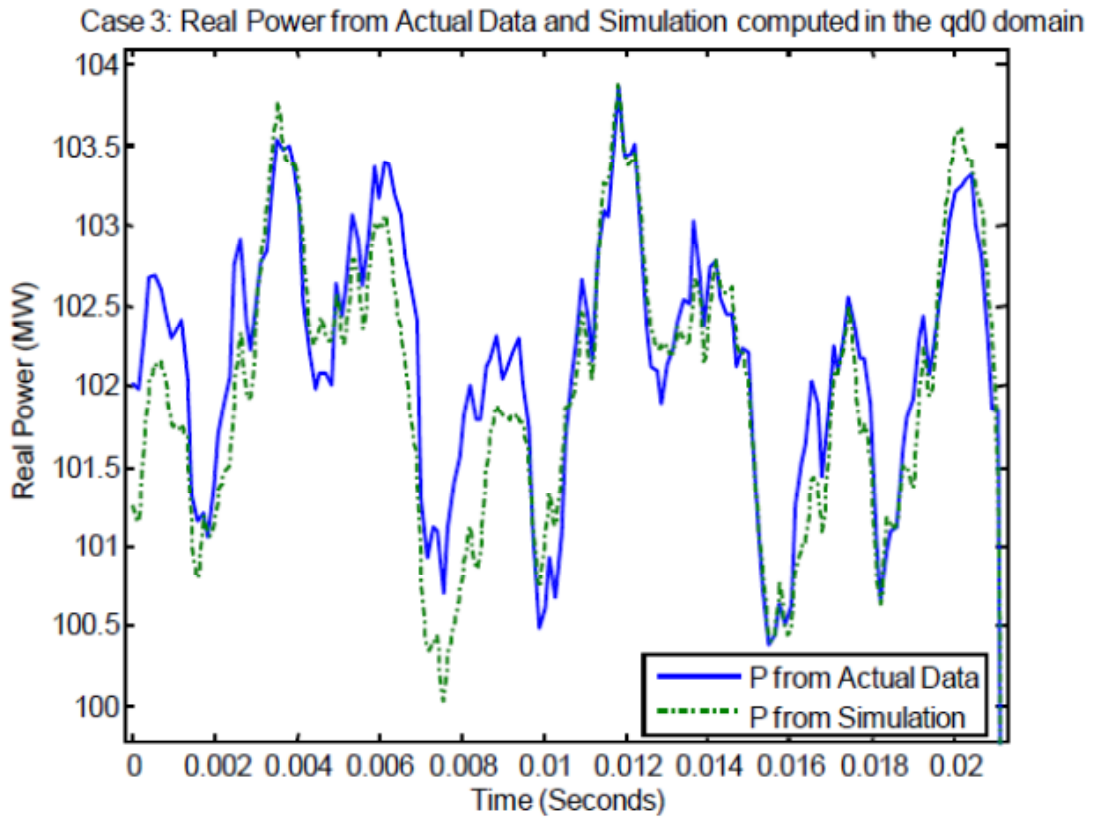


Figure 4.40: Case V-3: Real Power Comparison: Actual vs. Time Domain Model.

For each of the three cases, the real power and reactive power values generated from the actual data and the data extracted from the time-domain model match closely. They also match with the values obtained from phasor-domain calculations. Since the model has been validated for steady-state (pre-fault) operation for each of the three cases, we can conclude that the model is functioning correctly in steady state and we can move on to testing the operation of the model during the fault time for each of the three cases.

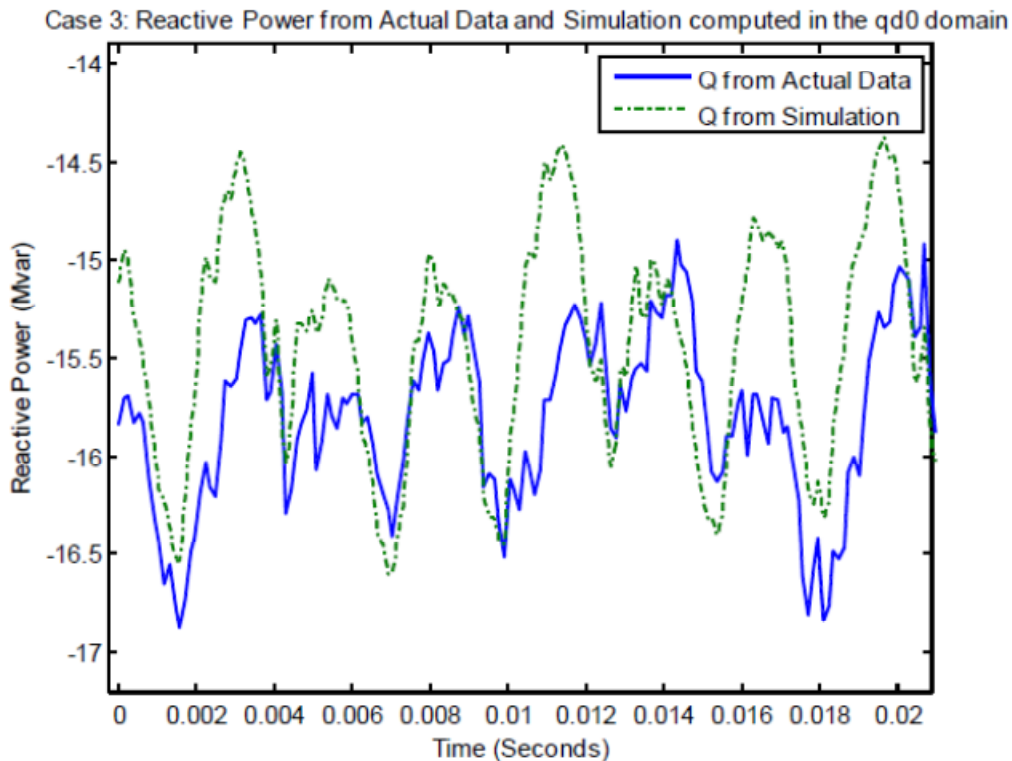


Figure 4.41: Case V-3: Reactive Power Comparison: Actual vs. Time Domain Model.

#### 4.5.4 Dynamic Performance

To evaluate the dynamic performance of the time-domain model during fault conditions, the validation process shown in flowchart in Figure 4.31 is used. The process is repeated for all of the three fault cases. The fault voltage and current waveforms for phase A for one case (Case V-2) are shown in Figures 4.42 and 4.43. It can be seen that the voltages from the actual data and the time-domain model are identical; this shows that the voltage data is being inputted correctly. It was necessary to remove the DC component from the actual voltage data before inputting it to the time-domain model, in order to avoid excessive numerical oscillations. The currents match closely but are not exactly identical; this may be due to the fact that the time-domain model is a considerably simplified model of a real-world WPP. The matching is close enough to allow us to proceed with the validation. The other two phases for Case V-1 and also all three phases for Cases V-2 and V-3 yielded results in which the matching between actual data and time-domain model data was very close.

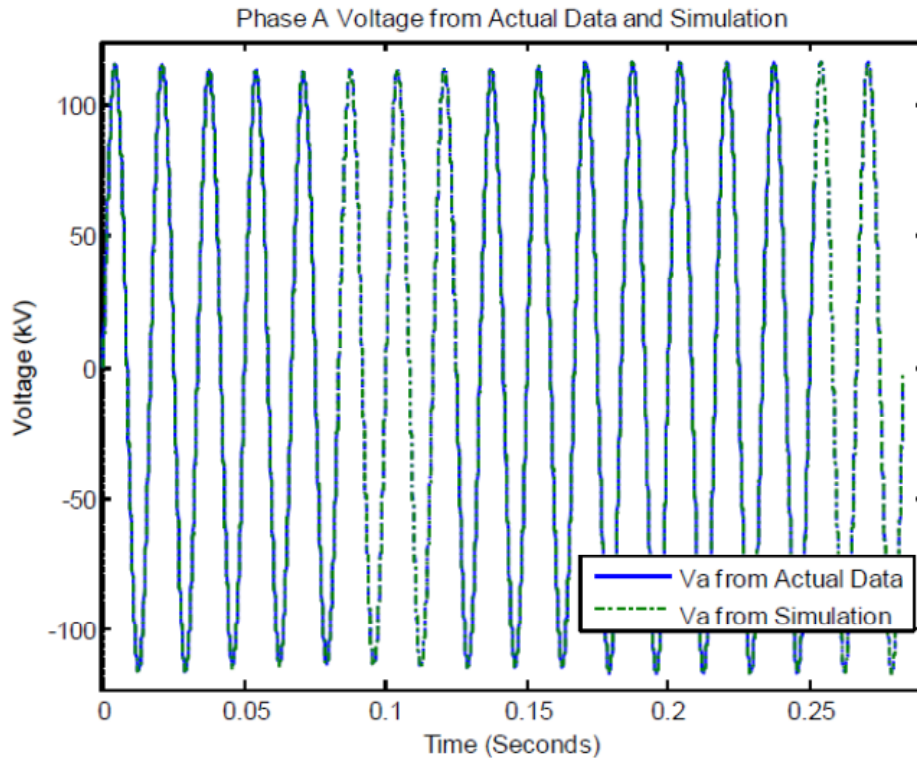


Figure 4.42: Case V-2: Voltage Comparison for Phase A during Fault.

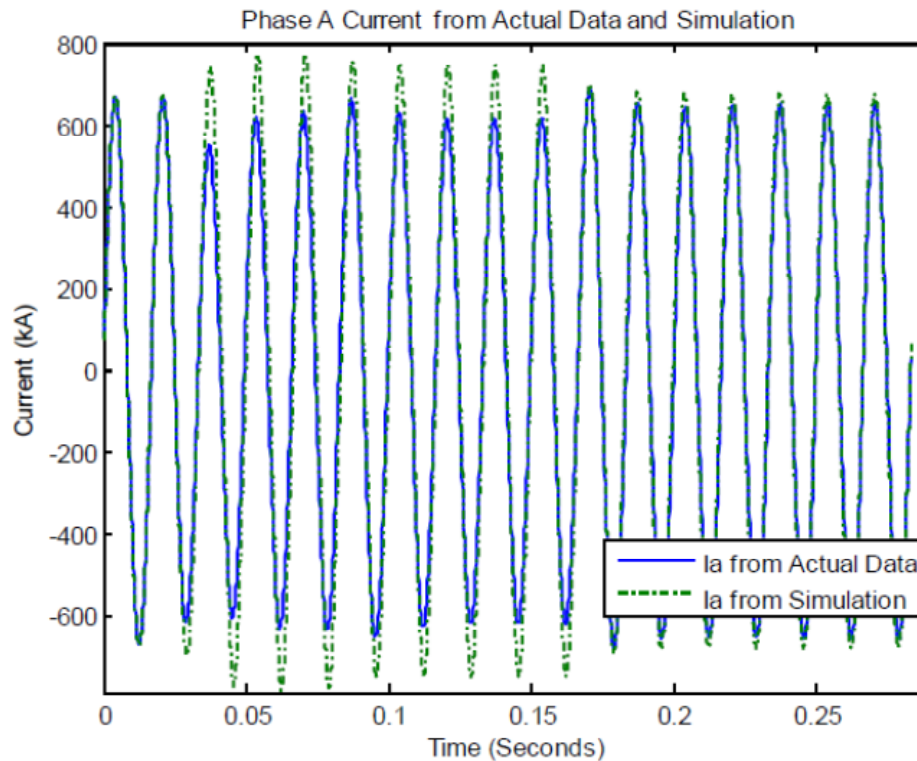


Figure 4.43: Case V-2: Current Comparison for Phase A during Fault.

The next step was to generate the real and reactive power datasets 1 and 2 referred to in Figure 4.31 and plot them together in order to compare the closeness of the match. The results are shown for Case V-1 in Figure 4.44, Case V-2 in Figure 4.45 and Case V-3 in Figure 4.46. The results show a close match, both in magnitude and phase, for each case. The model is therefore validated for dynamic studies and can be used for fault analysis, since it provides a good approximation of the behavior of an actual WPP under steady state and fault conditions.

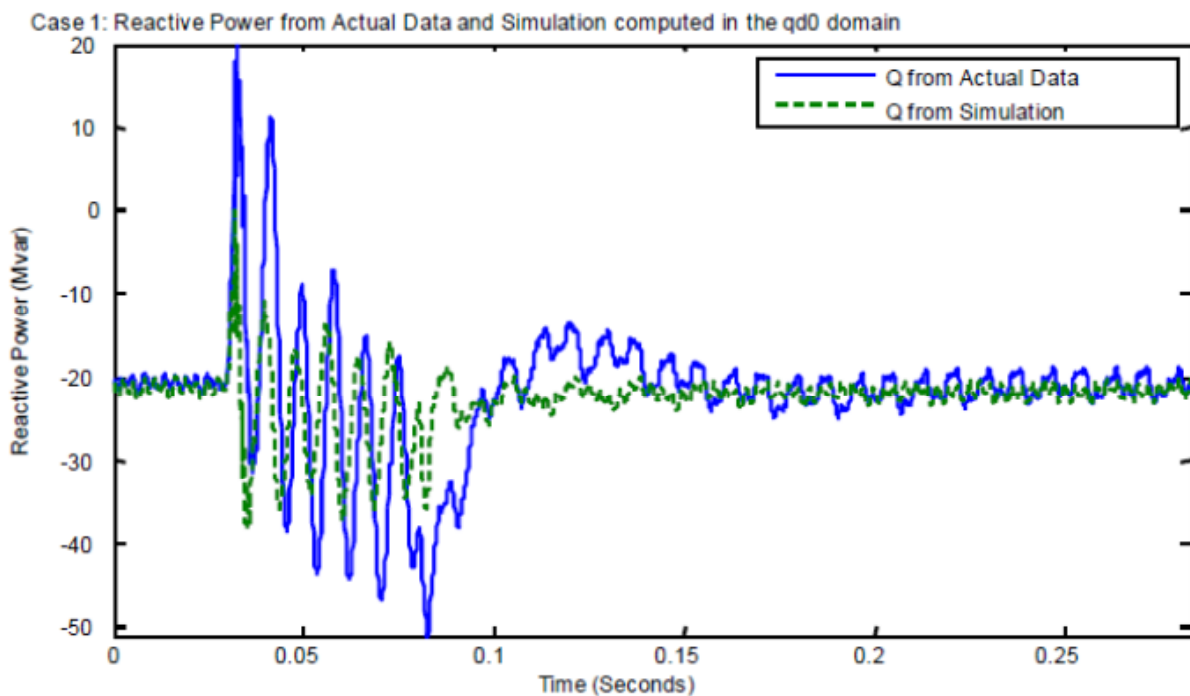
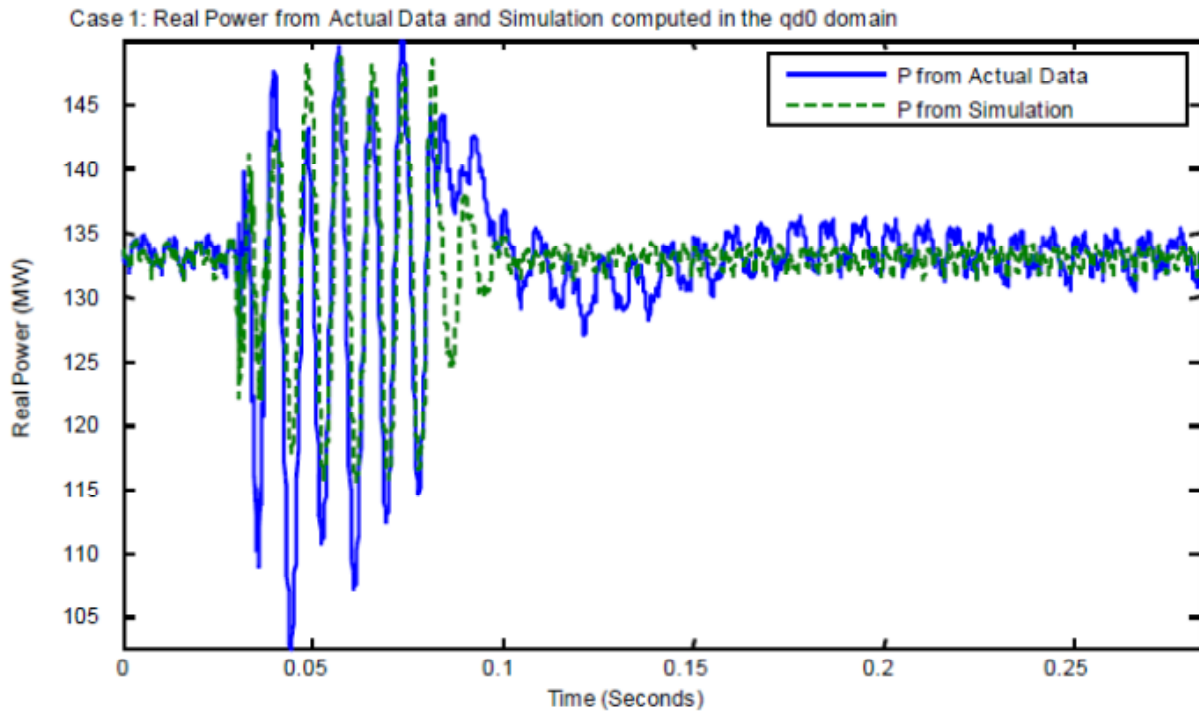


Figure 4.44: Case V-1: Comparison between actual and simulation-based real power and reactive power during fault condition.

While the matching is very close, the real and reactive power waveforms from the actual data and the simulation are not exactly identical. There are some small discrepancies between the real and reactive power plots obtained from the datasets 1 and 2. One example of such a discrepancy may be seen in the real plot for Case V-2. In this plot, the power output for both datasets is very similar for the first half of the fault duration, but halfway through the fault the phase difference between the real power waveforms abruptly increases and remains at the increased level till the fault time ends. This discrepancy (and the other ones that may be seen in the plots for each case) may be due to the simplifications made to the time-domain model in order to preserve its generic nature, since the induction generator itself is not explicitly modeled, and neither is the power electronic converter.

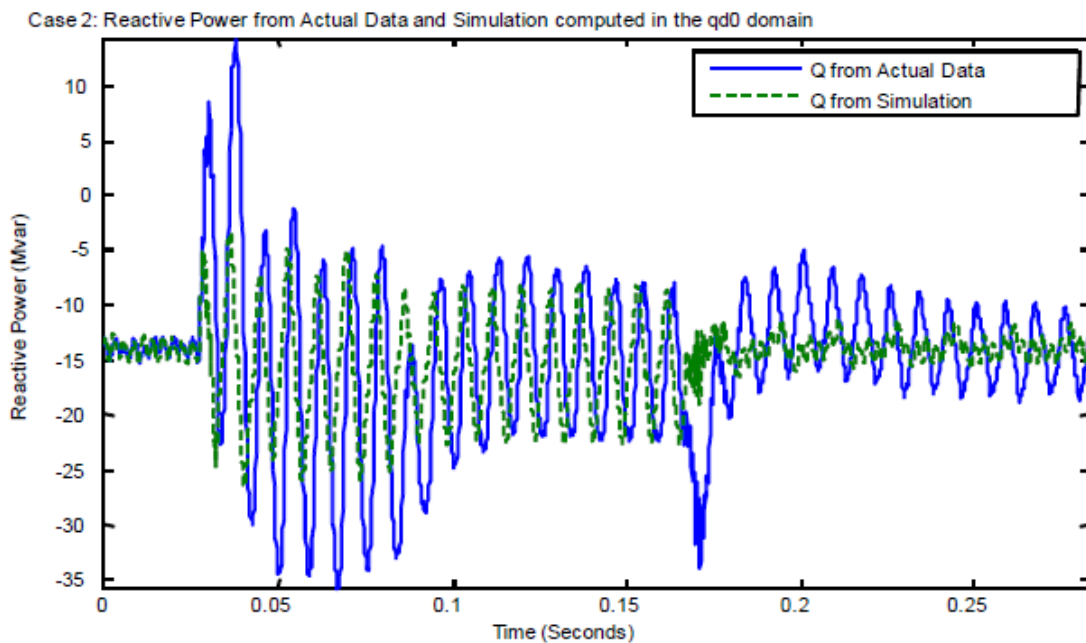
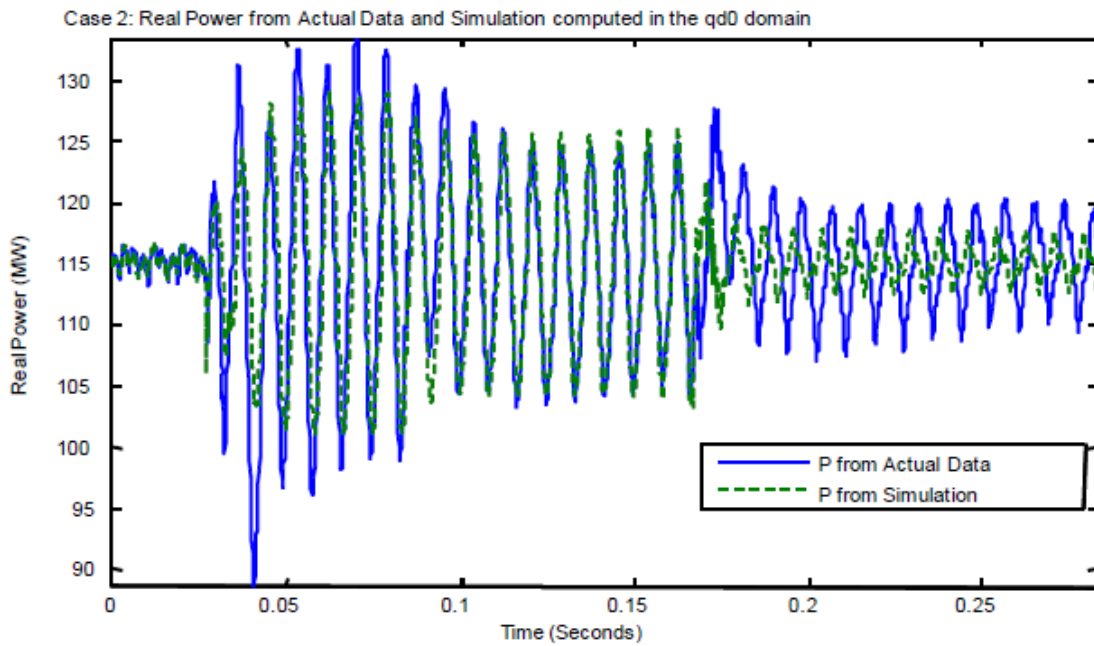


Figure 4.45: Case V-2: Comparison between actual and simulation-based real power and reactive power during fault condition.

Tuning of the parameters of the PI controllers present in the time-domain model has an impact on the appearance of the waveforms from dataset 2 (simulation). In particular, the proportional gain for the PI controller responsible for setting the q-axis current ( $I_q$  cmd) is critical. This is discussed in the following subsection.

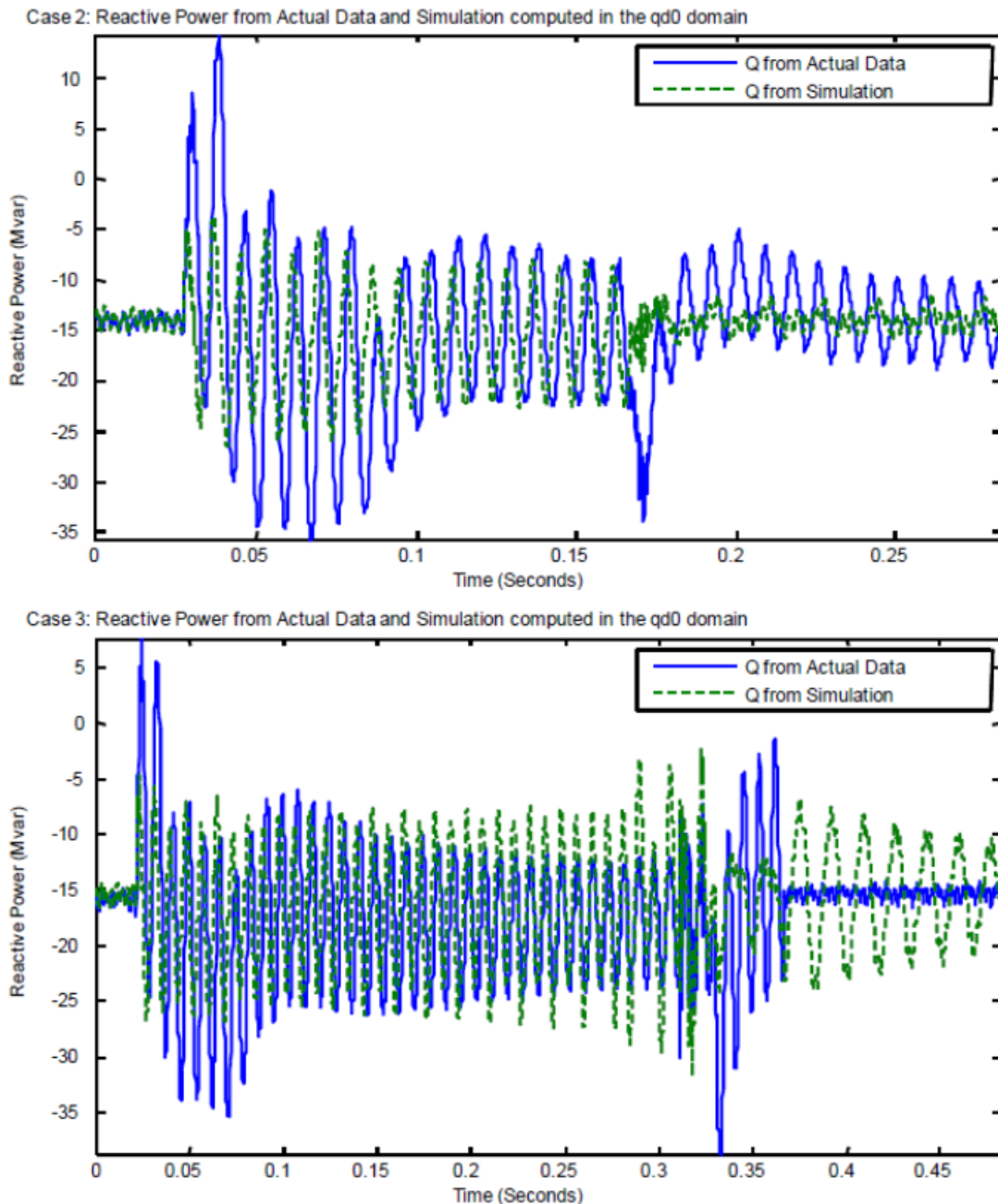


Figure 4.46: Case V-3: Comparison between actual and simulation-based real power and reactive power during fault condition.

#### 4.5.4.1 Effect of Proportional Gain on q-axis Current PI Controller

The value of the proportional gain setting on the q-axis current PI controller had a pronounced impact on the real power output from the time-domain model. As an example, we can consider the fault data from Case V-2. With a relatively low value of gain ( $K=2$ ), the output response was relatively damped as can be seen in Figure 4.47. In this case, the real power output from the time-domain model does not show as wide of a range of variation as does the real power calculated from the actual data. A high value of gain is necessary to improve the response of the controller and match the output from the actual data. Figure 4.48 shows the improvement in matching when the gain is increased to a high value. The high value of gain finally used ( $K = 25000$ ) was arrived at by trial and error, and provides good matching for all three fault cases.

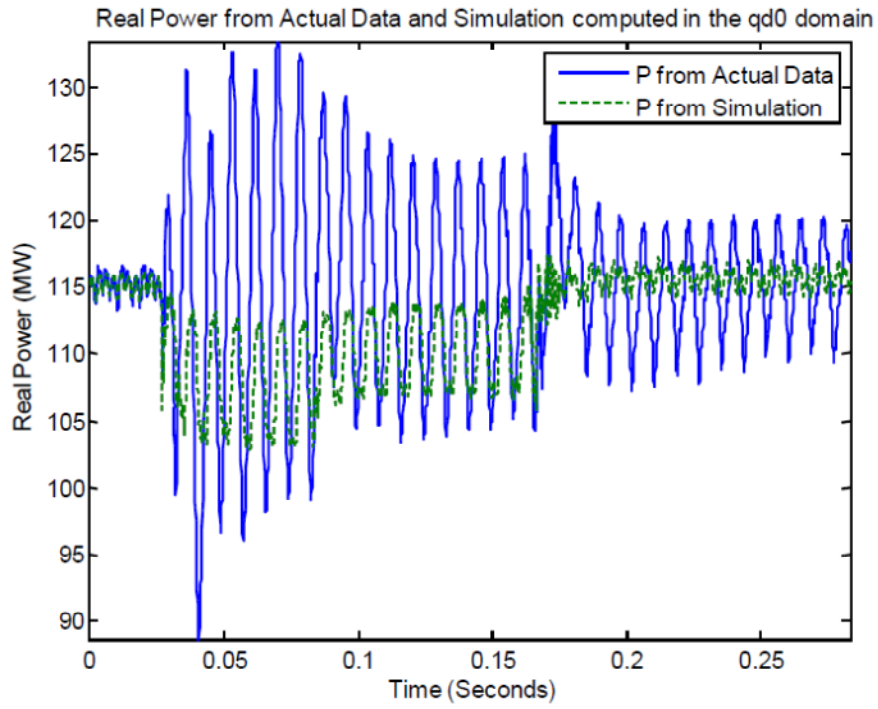


Figure 4.47: Case V-2: Comparison between actual and simulation-based real power during fault condition (controller gain  $K = 2$ ).

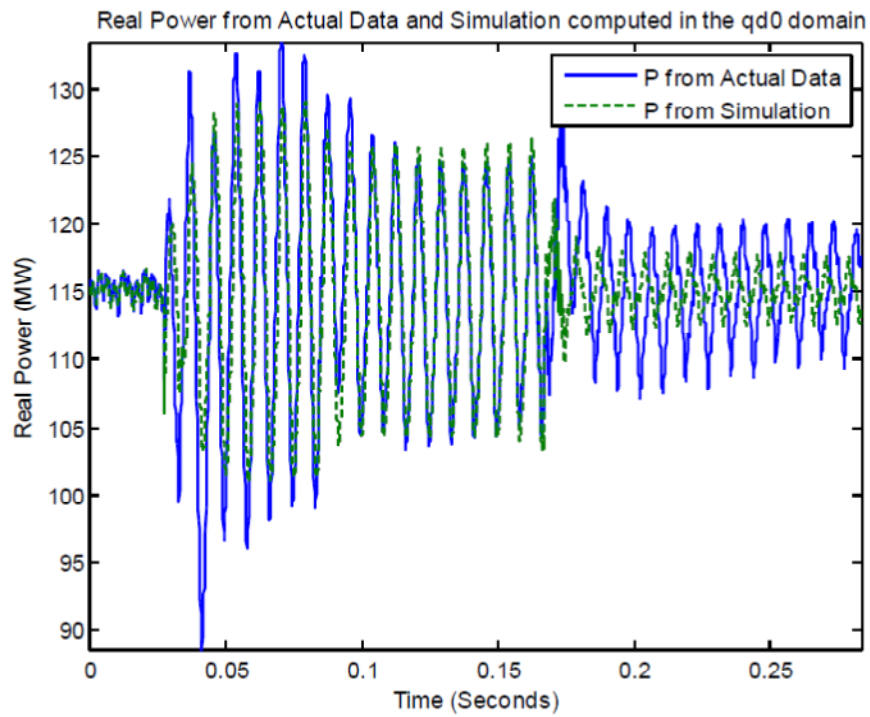


Figure 4.48: Case V-2: Comparison between actual and simulation-based real power during fault condition (controller gain  $K = 25000$ ).

## 4.6 Summary

The development, testing, and validation of a time-domain model of a DFIG WPP have been discussed in this chapter. The development of this model is part of an effort to develop generic manufacturer-independent wind turbine models capable of being used for power systems studies. To maintain generality, various approximations and simplifications have been used in the modeling process. The individual DFIGs of a WPP have been lumped into one large generator, and the collector system connecting them has also been simplified into an equivalent representation containing only series-connected transformers and impedances. The mechanical modeling has also been simplified, with all the rotating masses of the WPP being represented by an equivalent one-mass model. The induction generator, power electronic converter, and controls have been modeled using an equivalent regulated current source model. Despite all the simplifications, the developed time-domain model performs admirably, and is able to approximate the behavior of a real-world WPP in both steady state and fault conditions.

Aspects of the theory behind DFIG technology have also been discussed in this chapter, and the necessary mathematical foundation has been presented. The theory behind flux-vector control of induction machines is discussed. The decoupling of real and reactive power control, and the extraction of maximum extractable power from the wind, are the defining aspects of DFIG technology, and a discussion of these concepts is also presented. The modeling procedure has been discussed in detail, with the salient points being the development of sub-models for the generator, converter, mechanical turbine, and pitch control, the theory behind the operation of these sub-models, and the combination of these sub-models into a complete time-domain DFIG WPP model.

The validation of the time-domain model is also described. Initially, to check if the performance of the model is similar to that of a real-world WPP, a series of tests was performed with the model connected to an infinite bus. Once the model was validated for basic steady state operation, validation for three fault cases was performed. The model performed correctly as expected, and the validation process was considered successful. The time-domain model, having been validated, may be used for power systems studies incorporating wind power plants. There are some important points emerging from the validation that must be noted:

- The wind speed may change during a fault event, and if the wind speed is assumed to be constant during the fault, the validation results may not show a perfect match.
- Unlike a conventional power plant that typically is comprised of a single synchronous generator, wind power plants consist of hundreds of wind turbines with identical relay settings. In the post-fault scenario, some of the turbines may trip offline and stay offline. The pre-fault and post-fault generation levels will thus be different. The validation must consider this fact.
- A fault far away from the wind power plant usually creates a relatively smaller voltage sag at the POI, and the model described here is more likely to succeed in replicating this type of event. A nearby fault creates a large voltage sag, and it is harder to validate the model with this type of event.
- A large frequency change created by loss of generation or load is usually more difficult to validate, while a short event and shallow frequency sag is usually easier to validate using this model.
- The exact timing of the fault has a significant impact on the accuracy of the validation, due to impact of the timing on the severity of the fault.
- Unbalanced faults are usually harder to simulate and validate.

## 5. DFIG (Type 3) Wind Turbine Generators: Single-Machine Detailed Model

### 5.1 Introduction

In the last chapter, it has been shown that a model using current source representation for DFIG turbines is adequate for faults occurring outside the wind power plant. However, to model a wider variety of faults (such as faults internal to the wind power plant) and wind power plant and turbine protection, a more detailed representation of a DFIG turbine, with electrical machine and power electronics explicitly modeled, is necessary, especially to demonstrate the DC bus dynamics and protection of power semiconductor devices which may require the use of a “crow-bar” to limit the DC bus currents during a fault. In this chapter, we describe the development of such a detailed, single-machine DFIG turbine model. The model described here is an evolution of the fixed-speed (Type 1) and variable-slip (Type 2) models described in previous chapters. It incorporates many of the same subsystems as those models, while power electronic converters for decoupled real and reactive power control and maximizing of extraction of power from the wind.

### 5.2 Model Development

Wind turbines are complex electromechanical devices and incorporate a large number of controls. In order to tackle complexity, wind turbines can be thought of as a collection of subsystems which can be modeled individually. The individual subsystem models can then be assembled into a complete wind turbine model. From a modeling standpoint, a full converter PMA wind turbine consists of the following mechanical and electrical subsystems:

- Aerodynamic model for rotor;
- Mechanical two-mass model for drivetrain;
- Reference power calculation block;
- Pitch controller;
- Induction generator model;
- Rotor-side converter;
- Grid-side inverter;
- Unit transformer and grid representation.

The interaction between each of the components listed above determines the wind turbine model’s steady-state and dynamic response. Modeling of the aerodynamics and mechanical drivetrain is based on the differential and algebraic equations that describe their operation. Reference power is currently calculated based on wind speed, though in the future it will be calculated based on rotor speed. The pitch controller currently utilizes both power and rotor speed inputs, though it too will be modified in the future to only use rotor speed as input. The same induction generator model (available in PSCAD/EMTDC) as described in previous chapters 2 and 3 has been modified to serve the purposes of this model. The machine-side converter and grid-side inverter are modeled explicitly using diode and IGBT models supplied in PSCAD/EMTDC. Details for each of the subsystems are presented in the following subsections.

#### 5.2.1 Aerodynamic and Mechanical drivetrain models

The aerodynamic and mechanical drivetrain models for the DFIG turbine are identical to the ones presented in Chapter 2. No changes are necessary; the models described in Chapter 2 for fixed-speed (Type 1) are perfectly suitable for application to Type 3 turbines as well.

### 5.2.2 Reference power calculation

The reference power calculation is based on user-defined wind speed, as shown in Figure 5.1. Wind speed is per unitized based on rated wind speed, cubed and multiplied by rated power (2 MW) to get output power. If user-defined wind speed exceeds rated wind speed (13 m/s), output power is fixed to 2 MW.

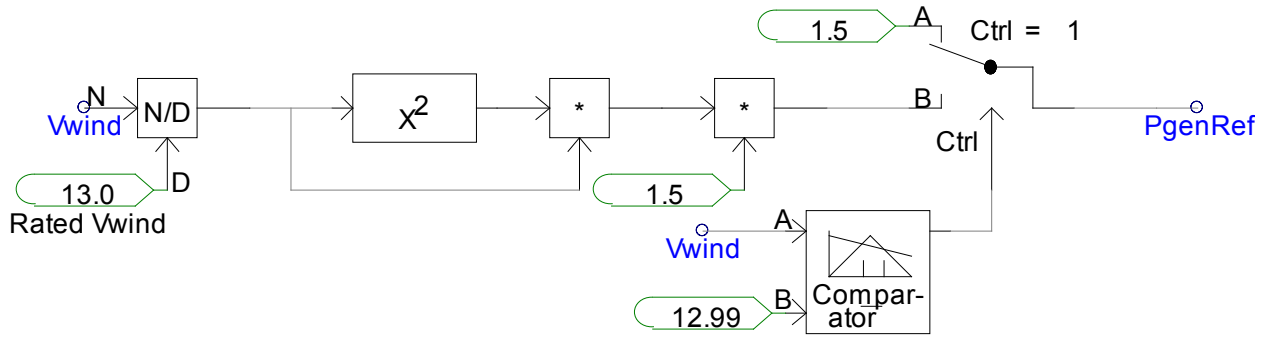


Figure 5.1: Reference power calculation

### 5.2.3 Pitch control block

The pitch control block (Figure 5.2) changes blade pitch angle at higher than rated wind speeds to spill excess power. Thus, power output is maintained at rated value even though wind speed exceeds rated wind speed. In this particular implementation, reference power is per unitized and converted to reference speed based on look-up table. A multiplier after the lookup table (Figure 5.3) is included to maintain stability. The reference speed and actual speed are compared and error drives upper PI controller. Reference power and actual power are also compared and error drives the lower PI controller. PI controller outputs are summed and hard-limited to generate the pitch angle signal. The pitch angle signal is active only when wind speed is close to rated, and otherwise is fixed at zero.

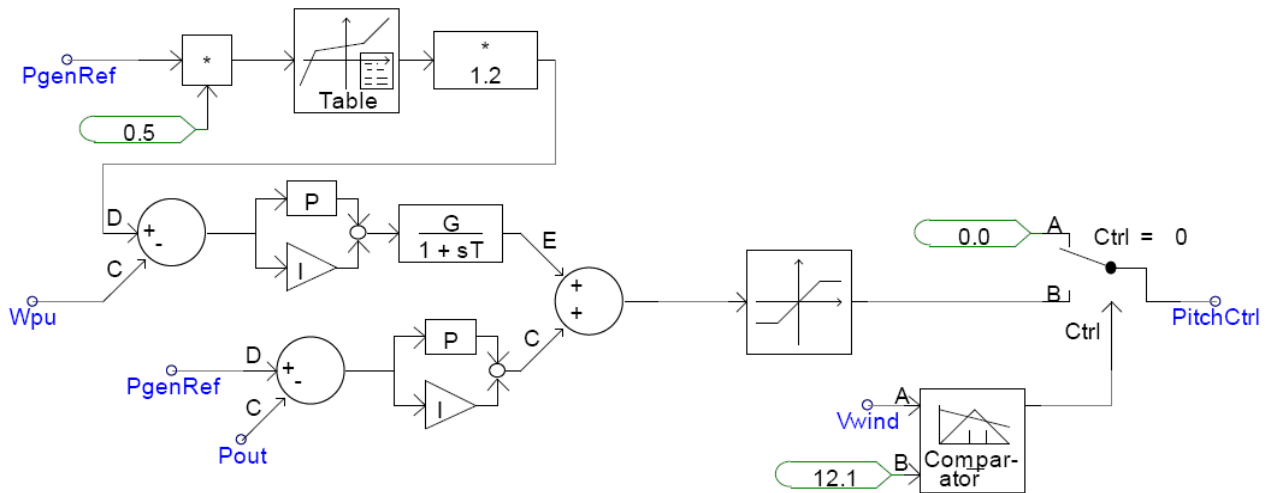


Figure 5.2: Pitch controller.

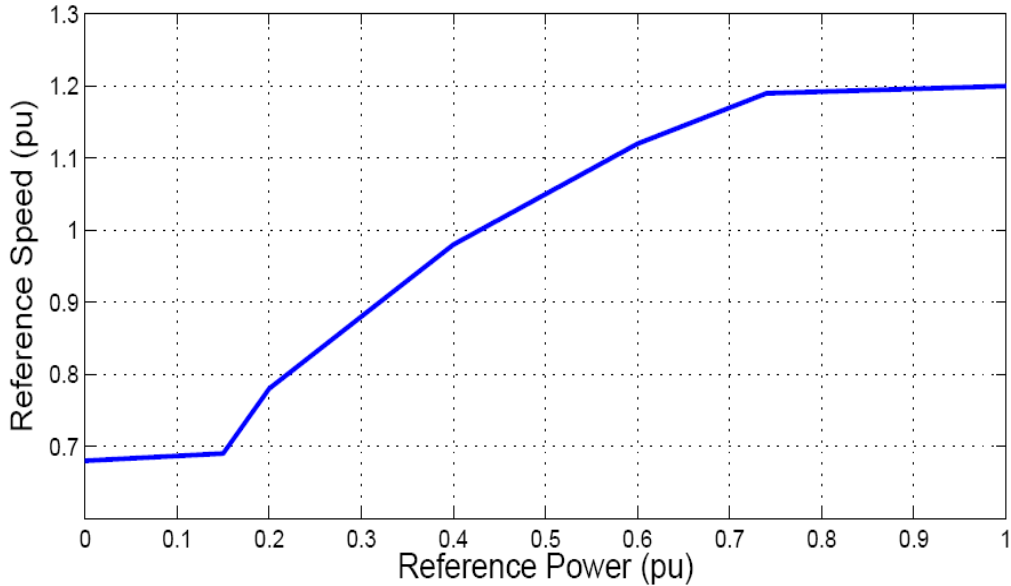


Figure 5.3: Rotor speed lookup table.

#### 5.2.4 Induction generator

DFIG wind turbines employ wound-rotor induction machines, for which models are readily available in most power system modeling softwares. The platform of choice to implement the model was PSCAD/EMTDC, and the in-built wound-rotor induction machine model was used. Alternatively, if the modeling platform does not offer a built-in model, users may develop third or fifth-order algebraic models for induction machines based on the literature available [45]. The type, ratings, and parameters of the induction generator used for this model are given in Appendix A.

#### 5.2.5 Rotor and grid side converter control for DFIG

The rotor-side converter of the DFIG is connected to the grid-side converter through a DC link capacitor. Assuming that the grid-side converter maintains a constant DC-link voltage, the role of the rotor side converter is to inject rotor frequency (variable) currents into the rotor circuit in such a manner as to achieve decoupled active and reactive power control. Since the converter operates in a stator-flux  $qd0$ -reference frame, the rotor current is decomposed into an active power ( $q$ -axis) and a reactive power ( $d$ -axis) component. With change in wind speed, slip changes and thus the frequency of rotor currents [45, 55]. Actual active power ( $P_{gen}$ ) is compared with the set point value ( $P_{genref}$ ) which is determined by the wind speed. A PI controller is used, as seen in Fig. 5.4, to generate the required value of  $q$ -axis rotor current  $I_{qr}$ . Similarly, for reactive power, a PI controller is used to generate the required  $d$ -axis rotor current  $I_{dr}$  [28]. The proportional gain ( $K_p$ ) and integral gain ( $K_i$ ) constants for the PI controller are determined using the Ziegler-Nichols method [56]. These values of  $I_{qr}$  and  $I_{dr}$  are transformed back into the  $abc$  frame to obtain the required value of rotor currents. Also seen in Fig. 5.4 is a hysteresis controller used to generate the switching sequence for the IGBT switches in the rotor-side converter. Required rotor currents obtained in  $abc$  frame are thus generated by using hysteresis control. Figures 5.5, 5.6, 5.7 and 5.8 show the implementation of the converter and controls in PSCAD/EMTDC.

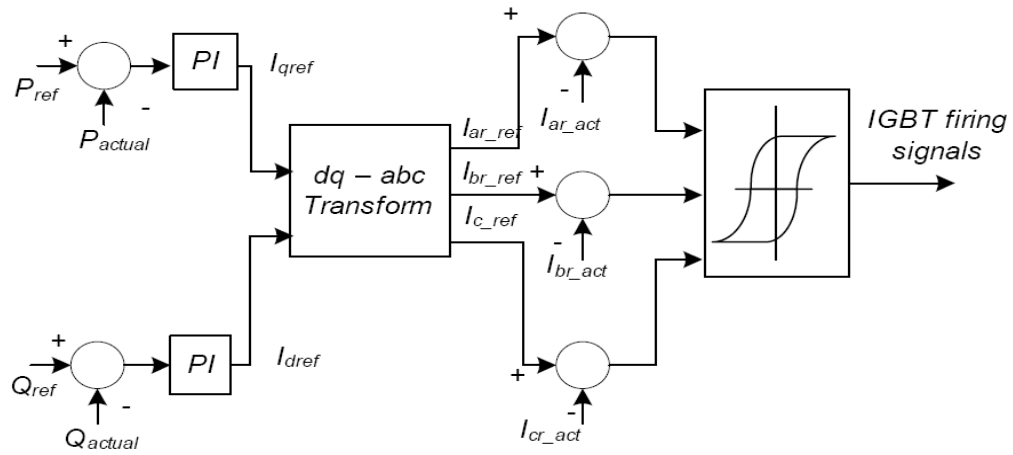


Figure 5.4: Rotor-side converter control.

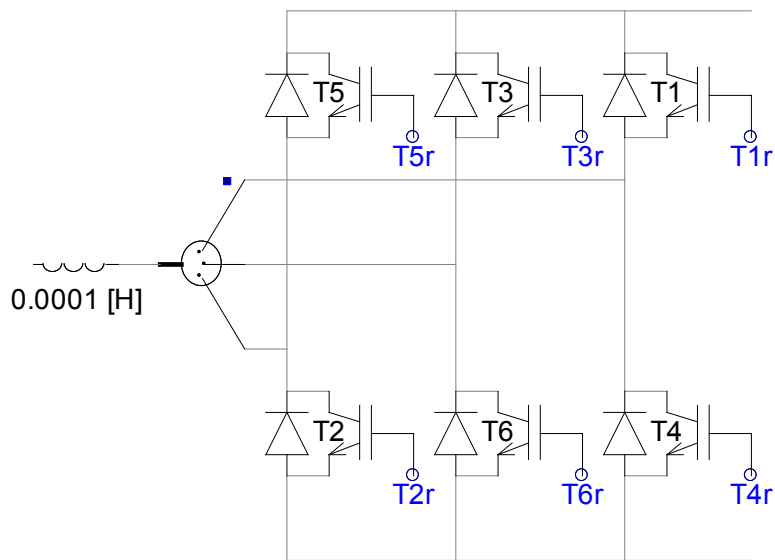


Figure 5.5: Rotor-side converter in PSCAD/EMTDC (current controlled VSI).

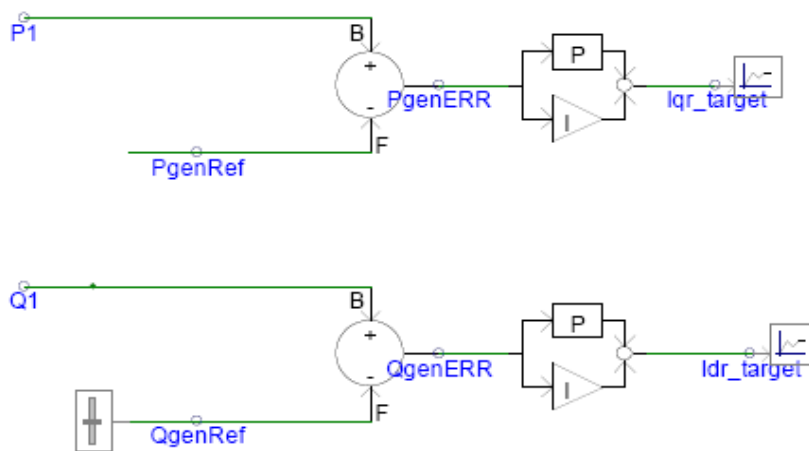


Figure 5.6: Real and reactive power errors drive q- and d-axis current controllers respectively.

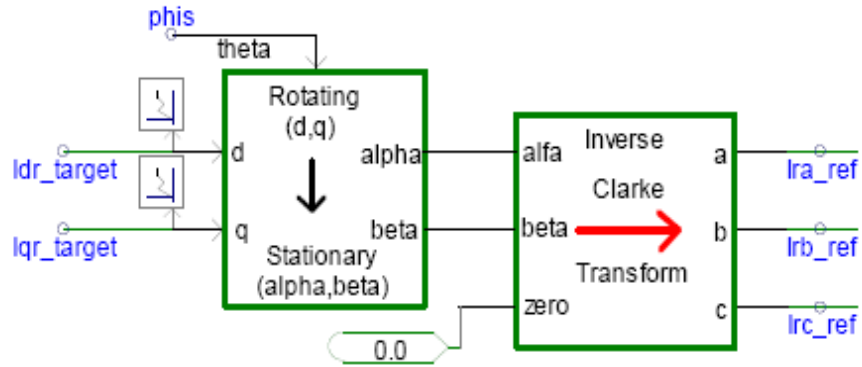


Figure 5.7: Currents are converted from dq0 domain to abc domain.

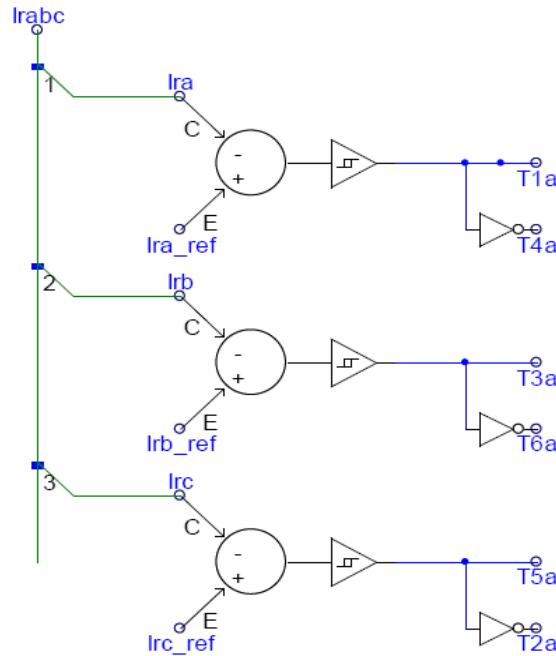


Figure 5.8: Hysteresis control for firing pulses.

The grid side converter is responsible for balancing power injected into the DC link capacitor versus active power exchanged with the grid [45, 55]. The converter at the grid side is controlled in a manner so as to achieve constant link voltage across the DC link capacitor. A relation between the DC link voltage and the  $qd0$ -axis stator currents and stator voltages is used to model the control and firing circuit for the grid-side converter. Field-oriented control, using Clarke and Park transforms, is used to obtain the actual  $qd0$ -axis stator currents and stator voltages. The desired  $qd0$  voltages to keep the DC link voltage constant, are obtained by comparing the actual value of the DC link voltage. PI controller is used to obtain the desired values of the stator voltages in  $qd0$  frame. The proportional gain ( $K_p$ ) and integral gain ( $K_i$ ) constants for the PI controller were determined using the Ziegler-Nichols method. These desired  $qd0$  voltages are then transformed to  $abc$  frame by applying the inverse Park-Clarke transforms to fire the IGBTs. Fig. 5.9 shows the block diagram for the grid-side converter control circuit and the inverse Park-Clarke transform. Figures 5.10 and 5.11 show the implementations of the inverter and controls in PSCAD/EMTDC.

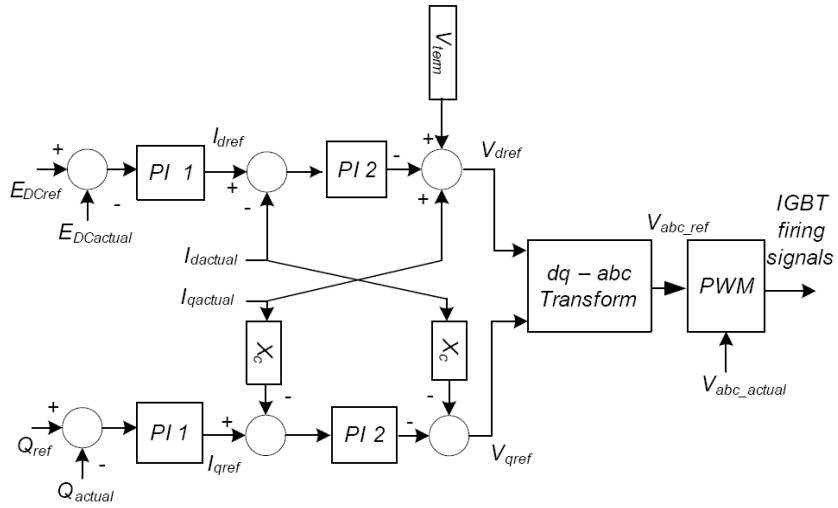


Figure 5.9: Grid-side converter control.

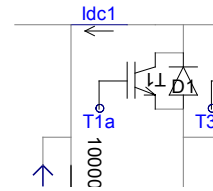


Figure 5.10: Grid-side converter in PSCAD/EMTDC.

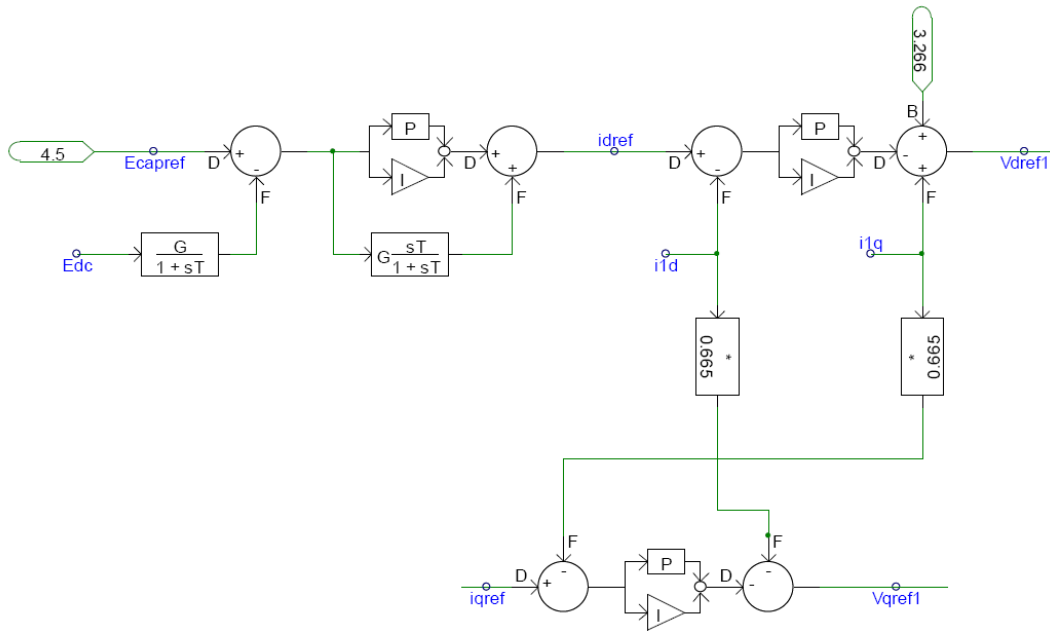


Figure 5.11: Grid-side inverter controls in PSCAD/EMTDC.

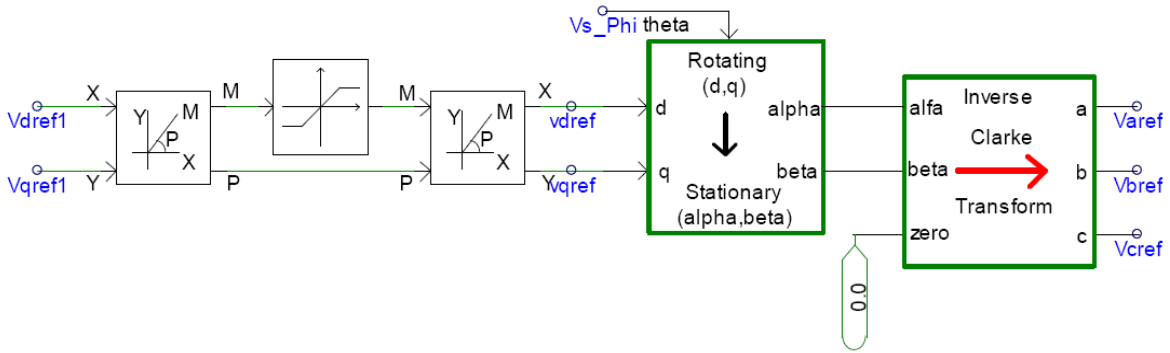


Figure 5.12: Voltages are converted from dq0 domain to abc domain.

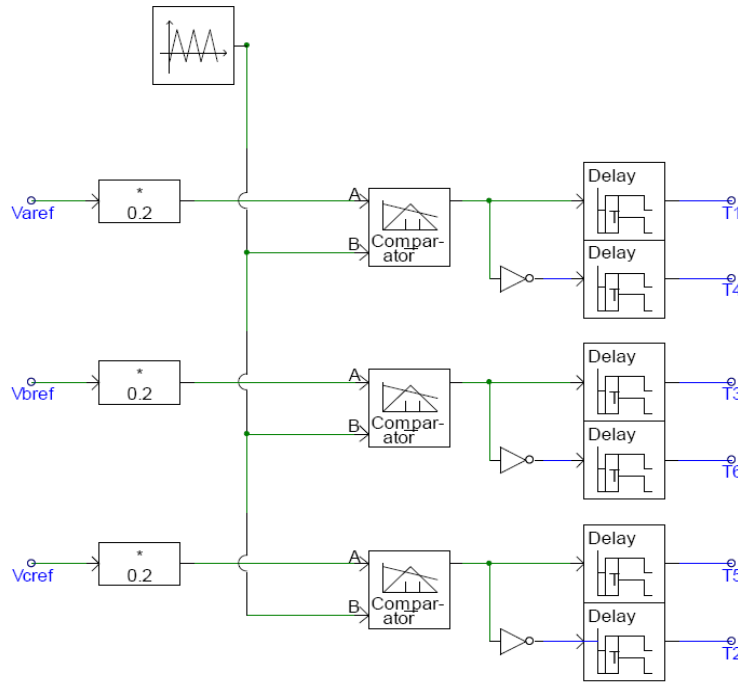


Figure 5.13: Sinusoidal PWM to generate firing signals.

### 5.2.5.1 Crowbar protection for rotor circuit

This model includes a “crowbar” circuit [57] that shorts the rotor windings of the induction generator in the event of detection of high currents in the rotor circuit. This protects the rotor-side converter from overcurrents. The implementation is shown in Figure 5.14. Signal CBAR goes high if overcurrent is detected (in our case, if rotor currents exceed 4 pu) and triggers the crowbar circuit.

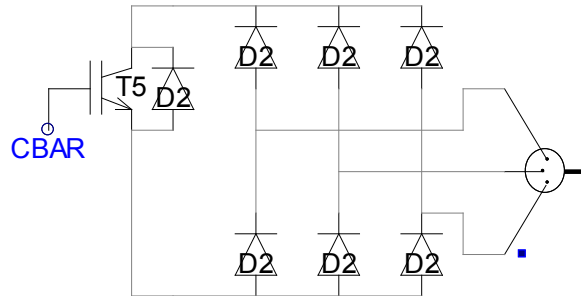


Figure 5.14: Crowbar for rotor circuit protection.

### 5.2.6 Unit transformer and grid representation

The unit transformer and grid are both modeled using in-built blocks supplied by PSCAD/EMTDC. The unit transformer is a wye-delta 2-MVA transformer with a primary voltage of 34.5 kV and a secondary voltage of 0.6 kV, and a per unit leakage reactance of 0.1 p.u. During the development and testing phase, the grid is represented by a 34.5-kV voltage source.

### 5.2.7 Complete model implemented in PSCAD/EMTDC

Figure 5.15 shows the complete model, not including the various control blocks, after all the individual subsystems have been assembled. Figure 5.16 shows the user controls that can be used to modify wind speed and reactive power demand. In the next section, the complete model testing is described.

## 5.3 Model Testing

The model testing phase is essential to evaluate the capabilities of the model. The model testing phase has three main objectives:

- To verify that desired wind turbine power curve is achieved;
- To demonstrate independent real and reactive power control;
- To demonstrate pitch controller action.

If the model is able to meet these objectives, we can use it with confidence as a platform for modeling more advanced controls, such as providing inertia and frequency response.

### 5.3.1 Power curve

The desired power curve is a cubic function of per unit wind speed (up to rated wind speed). Rated power is achieved at rated wind speed. Beyond rated wind speed, the desired power is flat at rated power. Thus, the curve has a sharp edge at rated wind speed. Figure 5.17 and Table 5.1 show the actual output of the simulation. From Figure 5.17, observe that the power output tracks the desired curve closely. The plot is obtained from a PSCAD/EMTDC simulation multi-run to ensure that the power output measured for each wind speed is the steady-state value. Thus, we can claim that that the first objective, that of achieving the desired power curve, is met.

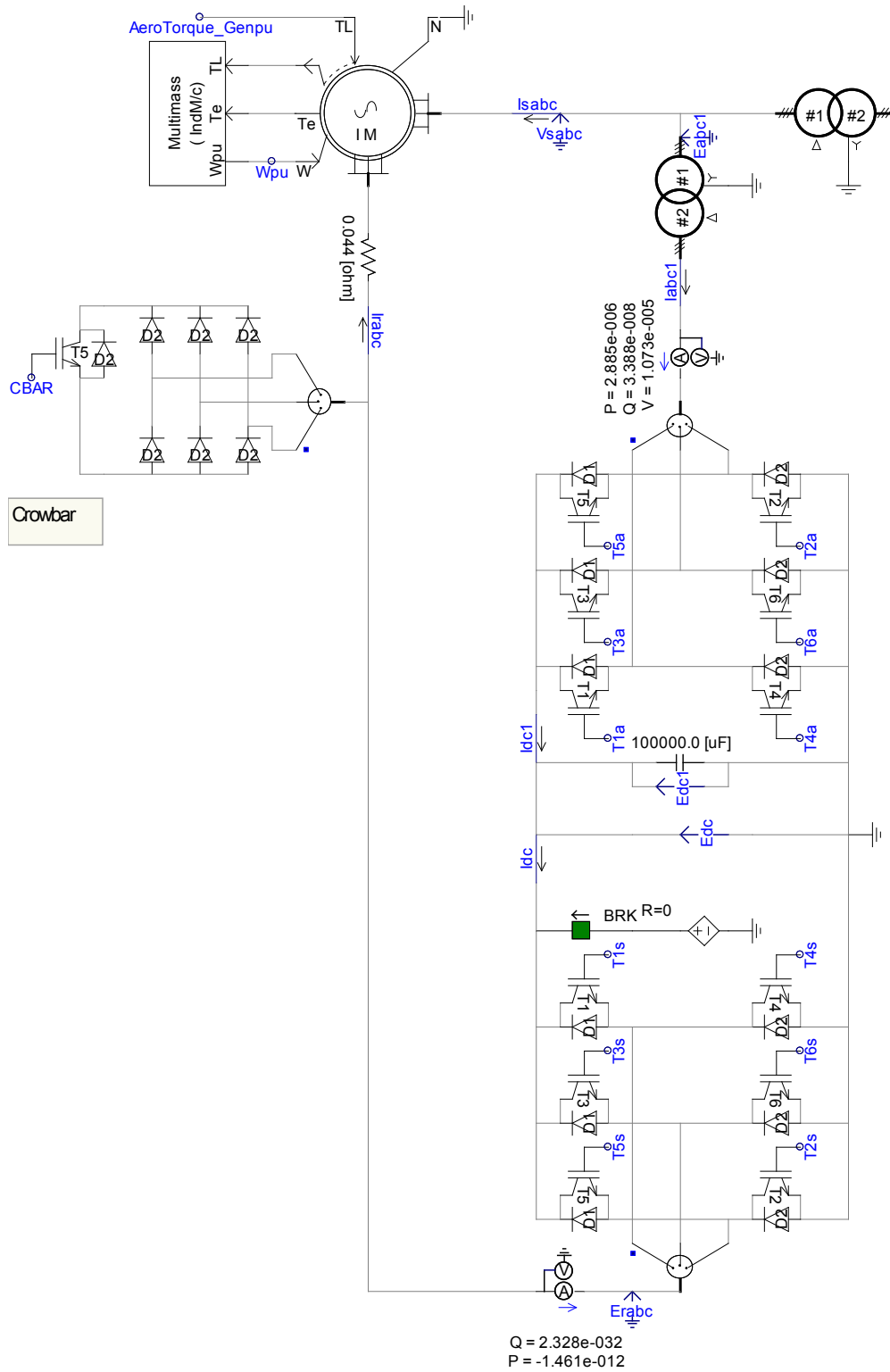


Figure 5.15: Complete model (not including controls and calculation blocks).

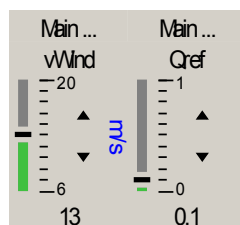


Figure 5.16: User inputs.

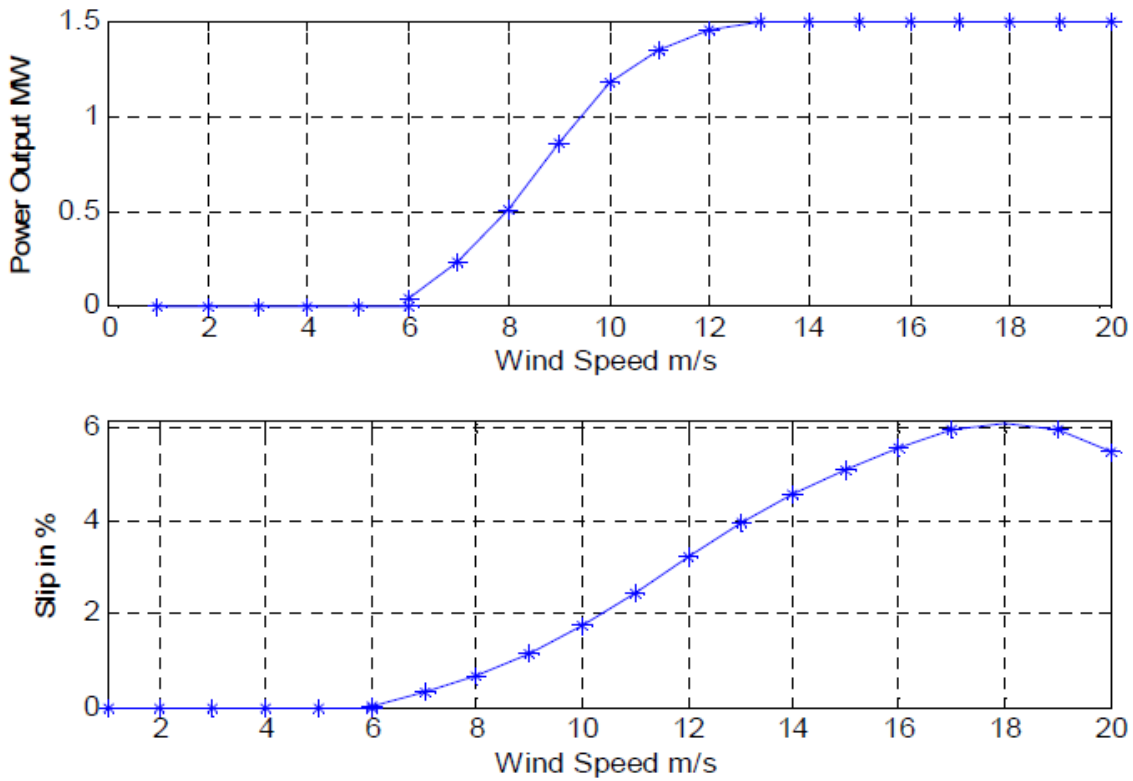


Figure 5.17: Power curve from simulation.

Table 5.1: Data for power curve and slip.

$V_{wind}$ m/s	Power Out MW	Slip %
6	0.035	-0.01
7	0.233	-0.32
8	0.501	-0.68
9	0.850	-1.16
10	1.181	-1.76
11	1.344	-2.44
12	1.451	-3.23
13	1.5	-3.96
14	1.5	-4.55
15	1.5	-5.08
16	1.5	-5.56
17	1.5	-5.95
18	1.5	-6.10
19	1.5	-5.97
20	1.5	-5.48

### 5.3.2 Independent real and reactive power control

To test if independent real and reactive power control has been achieved, four tests were carried out: real power drop, reactive power drop, real power rise, and reactive power rise. Each of these is modeled as a step change, i.e., at a particular instant, the simulation was paused and a step change was made to either the wind speed or reactive power demand. In the first test, a real power drop was simulated. The wind speed was changed from 14 m/s to 8 m/s at  $t=13s$ . The reactive power demand was set at 0.4 MVAR. The result is shown in Figure 5.18(a). The real power output drops and settles to the new value. Reactive power drops initially but recovers to the original value. In the second test, a reactive power drop was simulated. The result is shown in Figure 5.18(b). The wind speed

remains at 14 m/s throughout the run, but reactive power demand was changed from 0.4 MVAR to 0.0 MVAR at  $t=17$ s. The reactive power dropped, as expected. The real power output shows a slight perturbation but recovers to the original value. In the third test, a real power rise was simulated. The wind speed was changed from 8 m/s to 14 m/s at  $t=14$ s. The reactive power demand was set at 0.5 MVAR. The result is shown in Figure 5.18(c). The real power output rises and settles to the new value. Reactive power rises initially but recovers to the original value. In the fourth test, a reactive power rise was simulated. The result is shown in Figure 5.18(d). The wind speed remains at 13 m/s throughout the run, but reactive power demand was changed from 0.0 MVAR to 0.4 MVAR at  $t=11$ s. The reactive power rose, as expected. The real power output once again shows a slight perturbation but recovers to the original value.

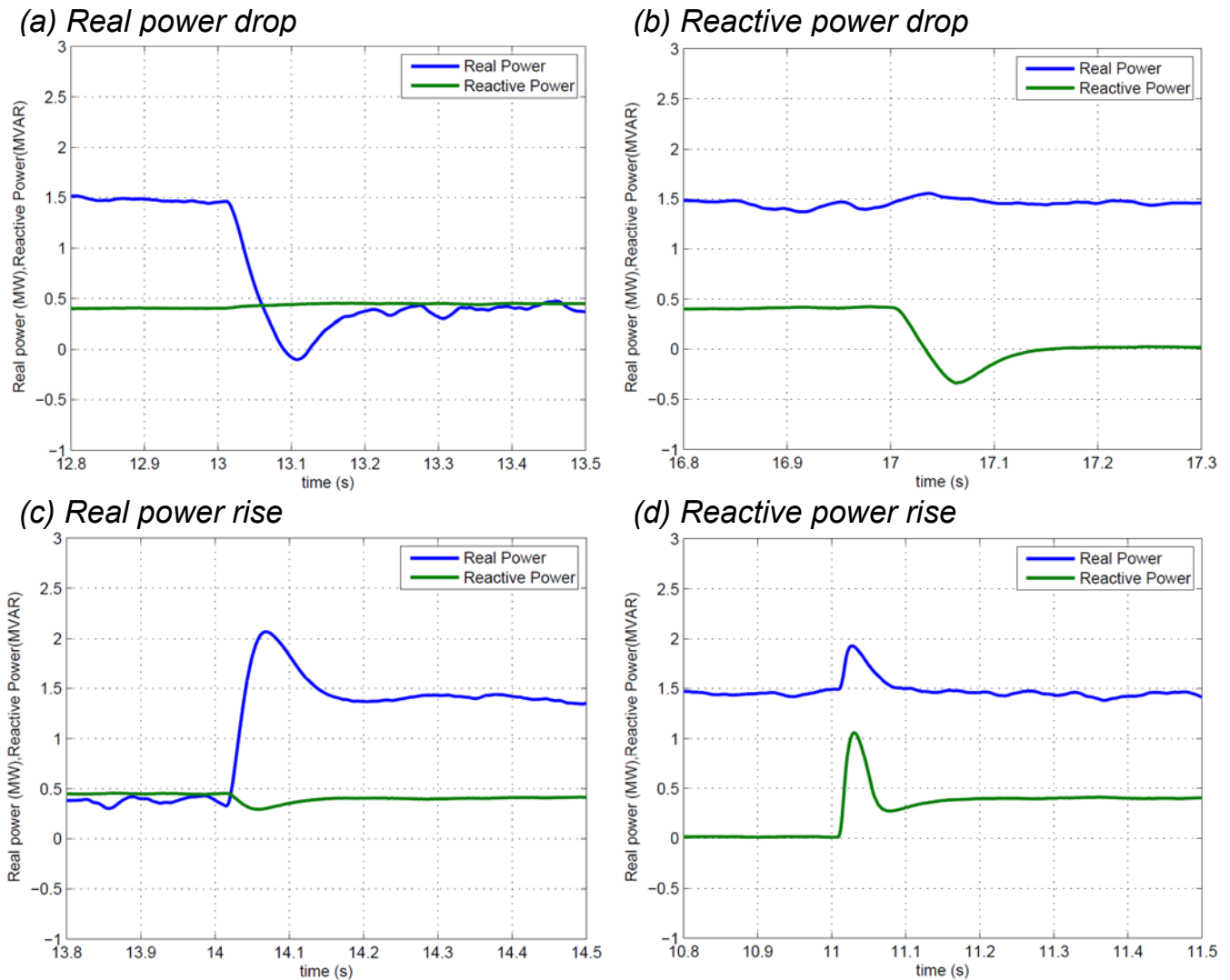


Figure 5.18: Test of decoupling of real and reactive power output for Type 3 turbine model.

Consider the real power drop shown in Figure 5.18(a). In this case, when wind speed drops suddenly, the pitch controller is de-activated, and the pitch angle moves quickly to zero. This is likely the cause for the overshoot observed in the power waveform. Within the wind turbine control system, the change in wind speed changes the  $P_{genref}$  value. At this instant, the error between  $P_{genref}$  and the actual power output becomes large, driving a change (reduction) in the value of  $q$ -axis current  $I_q$ . The  $d$ -axis current does not change since the reactive power set-point is not changed. This change in  $I_q$  leads to a corresponding change in the three-phase currents, leading to the desired change in the real power output. The reason the reactive power output briefly jumps is likely that the

decoupling technique is intended to work in steady-state rather than in the transient domain, and a surge in real power causes a rapid change in the flux linkages within the machine, which affect the reactive power. However, the reactive power controller detects this condition and corrects it. The results conclusively show that a change in either real power or reactive power demand does not affect the other quantity except momentarily. Based on the results of the testing, we can claim that the objective of independent real and reactive power control has been achieved.

### 5.3.3 Pitch control

A test was devised to evaluate pitch controller action. The wind speed changed from 11 m/s to 15 m/s at  $t=25s$ . The pitch angle was initially at 0 degrees (i.e., the pitch controller was inactive). From the results shown in Figure 5.19, it can be seen that the pitch controller becomes active when wind speed change occurs. This occurs due to new wind speed (15 m/s) being higher than rated. Eventually, the pitch angle settles close to -8 degrees, effectively spilling some excess power. The test shows that the pitch controller does indeed work in a stable fashion.

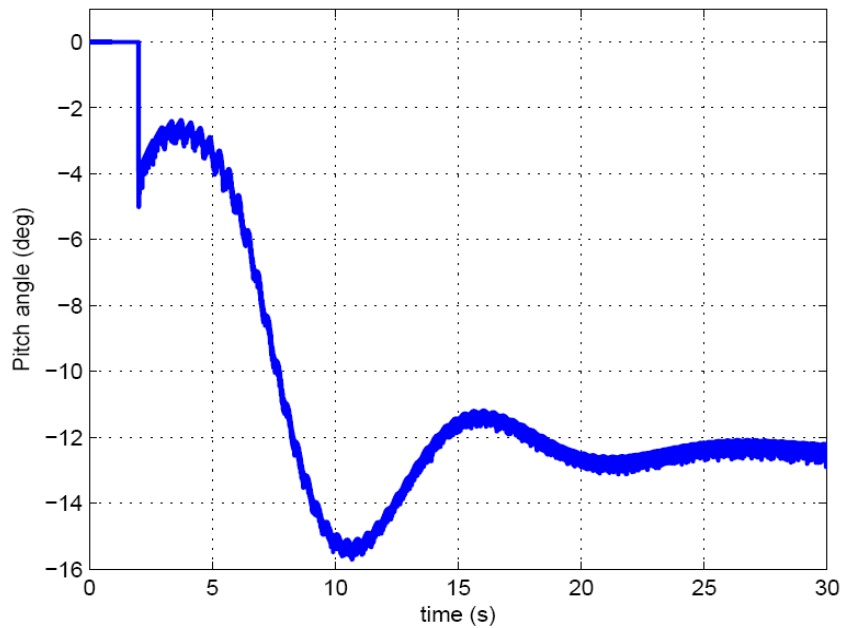
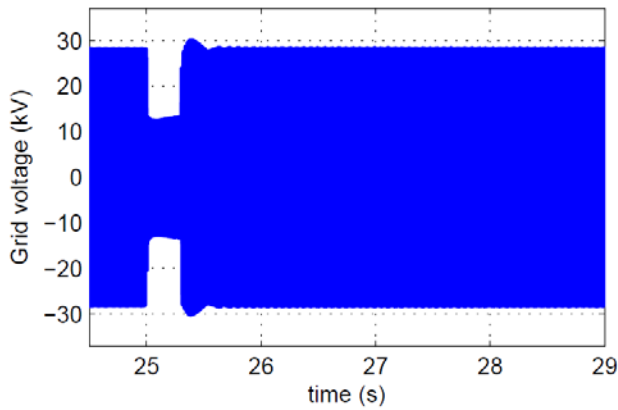


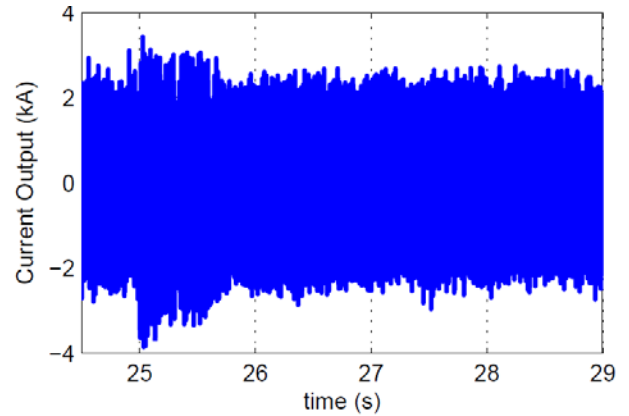
Figure 5.19: Pitch control action.

## 5.4 Dynamic Response

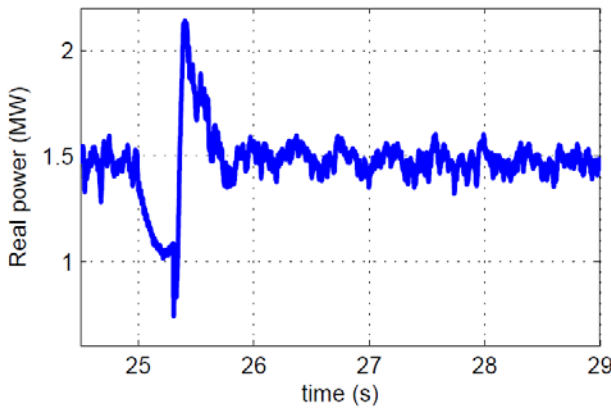
To demonstrate the model's ability to reproduce wind turbine dynamics, a test was created. The wind turbine was operated with a constant wind speed (13 m/s). This wind speed was chosen to be the rated value. A voltage sag on the grid was simulated, and the real and reactive power response of the wind turbine was observed. Note that this is not an implementation of low-voltage ride through (LVRT) but rather a test of dynamic response. The grid voltage drops gradually in this case from 1 p.u. to 0.8 p.u. at  $t=25s$ , and the sag persists for 18 cycles (0.3 seconds). A "V-shaped" sag is observed. The intent of the test is to show that the model does indeed respond to events occurring in the dynamic timescale and that the response of the machine to this event is realistic. Fig. 5.20 shows the results of the test, and shows that the model does indeed respond to the grid event as expected. The grid voltage, rotor converter current demand, real power and reactive power, rotor speed, and pitch angle during the event are shown.



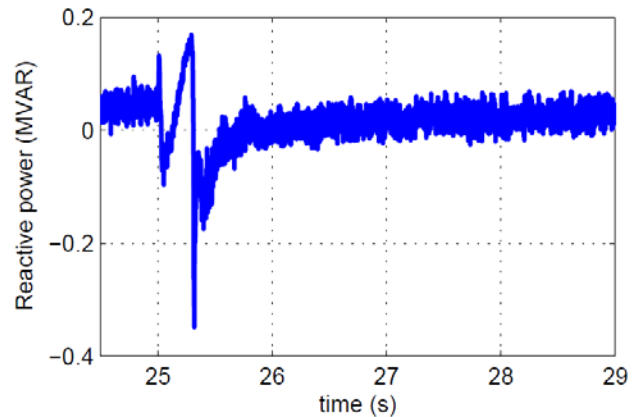
(a) Grid voltage



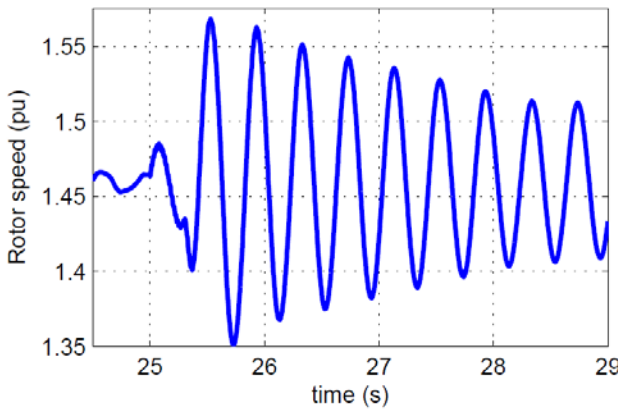
(b) Output current



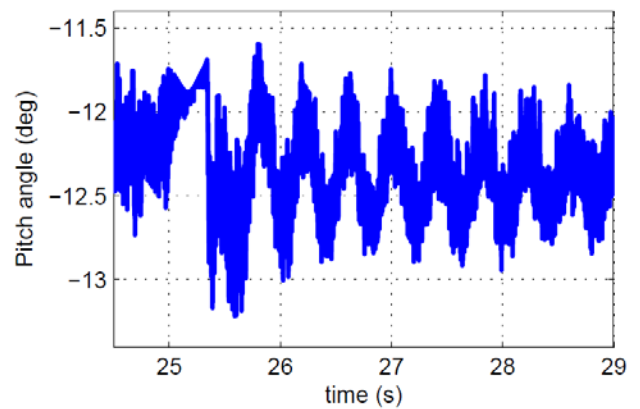
(c) Real power



(d) Reactive power



(e) Rotor speed



(f) Pitch angle

Figure 5.20: Real and reactive power response during voltage sag on the grid.

From Fig. 5.20, observe that real and reactive power show a sharp drop when the event starts. The converter then increases the current demand from the generator, which reflects as a jump in power. The pitch controller too seeks to maintain real power output at 2 MW. A considerable excursion occurs in the rotor speed, but it is eventually damped out. Based on these results, we can say that the model is behaving as expected, and realistic explanations for the response can be offered.

## 5.5 Summary

The development and testing of a detailed single-machine DFIG wind turbine has been presented here. This model is built on the same platform as the Type 1 and Type 2 models. The modeling framework used is unrestricted, manufacturer-independent, and can be implemented in any dynamic modeling software. The model subsystems have been described individually, as have the signals exchanged between these subsystems when assembled into the complete model. Details of model parameters have been provided to allow reproduction of the results shown here. The model testing objectives and methods have also been presented. The power curve requirements have been met, decoupled real and reactive power control requirements have been met, and the pitch controller works as expected. An example of the model's dynamic response has also been provided. In the future, the model can be used as a platform to model various controls such as those needed to provide LVRT and inertial support.

## 6. Modeling of Full-Converter (Type 4) Wind Turbine Generators Employing Permanent Magnet Alternators

### 6.1 Introduction

In the United States, the capacity of wind power being interconnected and being planned for interconnection is steadily increasing [2]. This trend is expected to continue due to increased concerns about the environment, energy security, and job creation. There are a number of different wind turbine technologies competing for market-share in this growing industry. One of these technologies is the full converter wind turbine (FCWT) employing a permanent magnet alternator (PMA). This technology has a number of significant advantages [58]. It effectively decouples the generator from the grid, improving fault response. It allows the turbine to operate over a wide speed range, leading to improved power extraction from the wind. The converter interfacing the turbine to the grid has to handle the entire output of the generator (unlike in a DFIG turbine where the converter handles only 30% to 40% of the generator output) and hence is more costly and lossy, but also provides more headroom to supply reactive power to the grid. The PMA itself has no rotor windings, reducing excitation losses and reducing the size of the generating unit with respect to competing technologies. Absence of rotor slip rings reduces maintenance requirements. This combination of factors is driving the increasing penetration of FCWTs, especially for offshore wind power plants.

The popularity of FCWTs has led to a search for reliable models to evaluate the impacts of integrating these FCWTs into the existing grid. The model presented in this report is a generic, manufacturer-independent model for a PMA-based FCWT, with no restrictions on its use. The converter topology of the model described in this report is a popular one; the PMA is interfaced to the grid through an AC-DC-AC conversion system. The AC-DC converter is comprised of a diode-bridge rectifier and a buck-boost converter which controls the DC link voltage. The DC-AC conversion is accomplished using a current-controlled inverter which controls the real and reactive output power. Although the focus in this report is on the specific topology mentioned, various converter topologies can be modeled with simple modifications using the same framework. In the past we have developed an FCWT model with an entirely different topology using this framework [35]. The mechanical and aerodynamic components of the model presented here are identical to those presented in [35].

A number of FCWT models employing PMAs have been described in the literature. FCWT computer models have been described in [58], [59], [60] and [61]. An electromechanical model employing a boost converter has also been developed [62]. Converter topologies vary widely across all these models. The model described in this report differs from these models on various points. Unlike in [58], the model presented here employs a buck-boost converter. This converter is similar to the converter described in [61] with one notable exception; the PMA-side converter in [61] is intended for maximum power point tracking (MPPT) application while the PMA-side converter described here is intended for DC link voltage control. Details of the model structure and development, as well as details of the model testing, are provided in the following sections.

### 6.2 Model Development

From a modeling standpoint, a full converter PMA wind turbine consists of the following mechanical and electrical subsystems:

- Aerodynamic model for rotor;
- Mechanical two-mass model for drivetrain;
- Reference power calculation block;
- Pitch controller;
- Permanent magnet alternator (PMA) model;

- Rectifier and buck/boost converter models (for DC-link voltage control);
- Inverter model (current-controlled VSI);
- Unit transformer and grid representation.

The interaction between each of the components listed above determines the wind turbine model's steady-state and dynamic response. Each of these subsystems presents a unique modeling challenge. Modeling of the aerodynamics and mechanical drivetrain is based on the differential and algebraic equations that describe their operation. Reference power is currently calculated based on wind speed, though in the future it will be calculated based on rotor speed. The pitch controller currently utilizes both power and rotor speed inputs, though it too will be modified in the future to only use rotor speed as input. A general PMA model is available in PSCAD/EMTDC which can be modified to serve the purposes of this model. The rectifier, buck/boost converter and inverter are modeled explicitly using diode and IGBT models supplied with PSCAD/EMTDC. Details for each of the subsystems are presented in the following subsections.

### 6.2.1 Aerodynamic and mechanical drivetrain models

The aerodynamic and mechanical drivetrain models for the PMA FCWT are identical to the ones presented in Chapter 2. No changes are necessary; the models described in Chapter 2 for fixed-speed (Type 1) are perfectly suitable for application to Type 4 turbines as well.

### 6.2.2 Reference power calculation from wind speed

The reference power calculation is based on user-defined wind speed, as shown in Figure 6.1. Wind speed is per unitized based on rated wind speed, cubed and multiplied by rated power (2 MW) to get output power. If user-defined wind speed exceeds rated wind speed (13 m/s), output power is fixed to 2 MW. A table-based characteristic is used to remove sharp changes from the power output curve. This “softening” of the power curve is discussed in the model testing section.

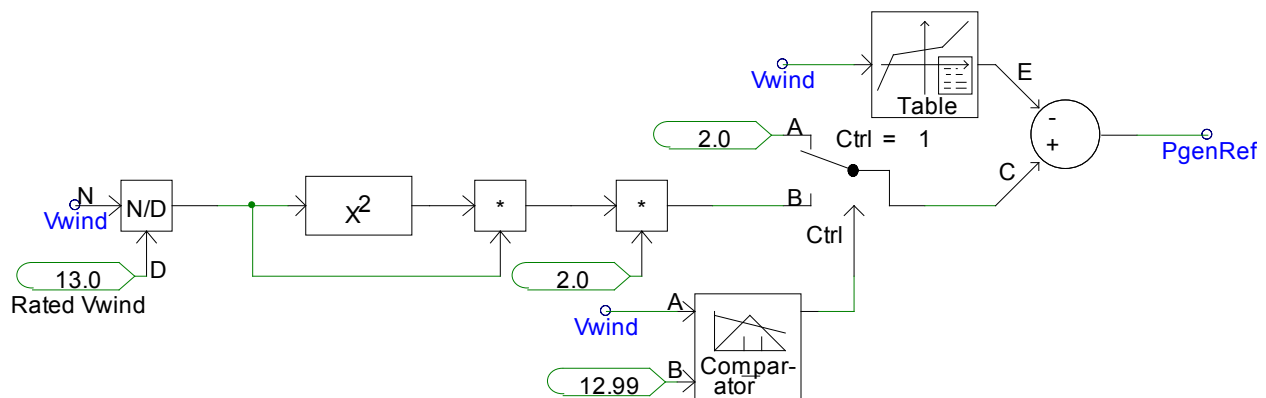


Figure 6.1: Reference power calculation.

### 6.2.3 Pitch control block

The pitch control block (Figure 6.2) changes blade pitch angle at higher than rated wind speeds to spill excess power. Thus power output is maintained at rated value even though wind speed exceeds rated wind speed. In this particular implementation, reference power is per unitized and converted to reference speed based on look-up table (Figure 6.3). A multiplier after the lookup table is included to maintain stability. The reference speed and actual speed are compared, and the error drives the upper PI controller. Reference power and actual power are also compared and the error drives the lower PI controller. PI controller outputs are summed and hard-limited to generate the pitch angle signal. The pitch angle signal is active only when wind speed is close to rated, and otherwise is fixed at zero.

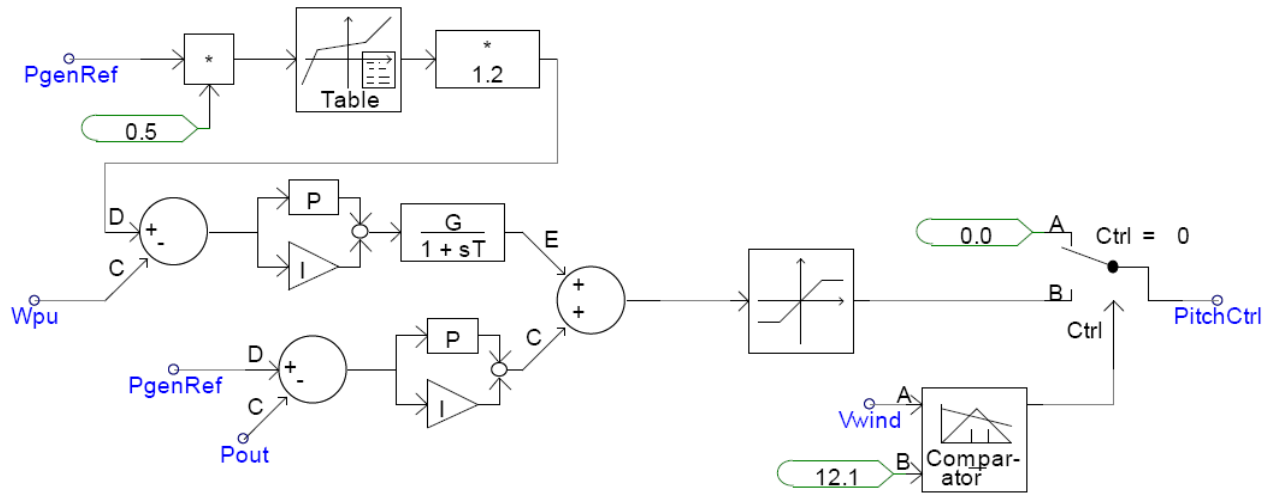


Figure 6.2: Pitch controller.

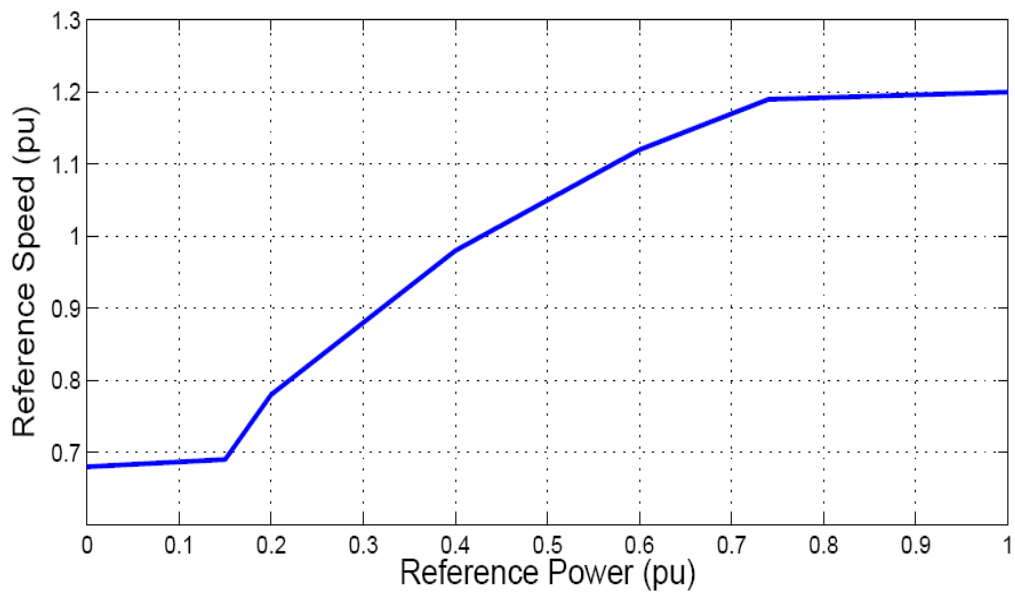


Figure 6.3: Rotor speed lookup table.

### 6.2.4 Permanent magnet alternator

The permanent magnet alternator is modeled using a built-in PSCAD/EMTDC PMA block. The terminals of the block are shown in Figure 6.4, while the type, ratings, and parameters of the machine are provided in Appendix A.

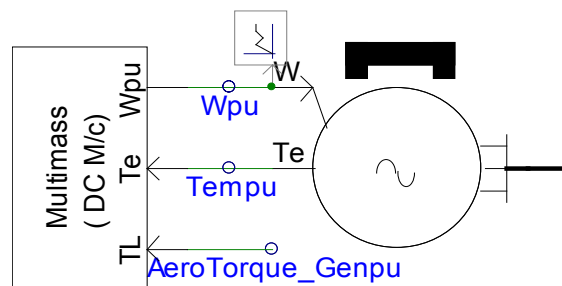


Figure 6.4: Permanent magnet alternator in PSCAD/EMTDC

### 6.2.5 Rectifier and buck/boost converter for DC-link voltage control

The rectifier and buck/boost converter models responsible for converting the AC output of the PMSG to a fixed DC voltage are shown in Figure 6.5. An example of the use of buck/boost converters for DC link control for PMA wind turbines is provided in [61]. A 3-phase diode bridge converts PMA output to a variable DC voltage. The buck-boost converter maintains the DC link at a constant 3.6 kV. The DC link capacitor is modeled as two identical capacitors with ground in between them due to PSCAD/EMTDC ground reference issues. The controller for the buck/boost converter is shown in Figure 6.6. This controller is based on PI control; any error between the desired voltage set-point (3.6 kV here) and the actual voltage drives the PI controller and generates a duty signal output. The duty signal is compared to a triangle wave to generate firing signals for the IGBT in the buck/boost converter.

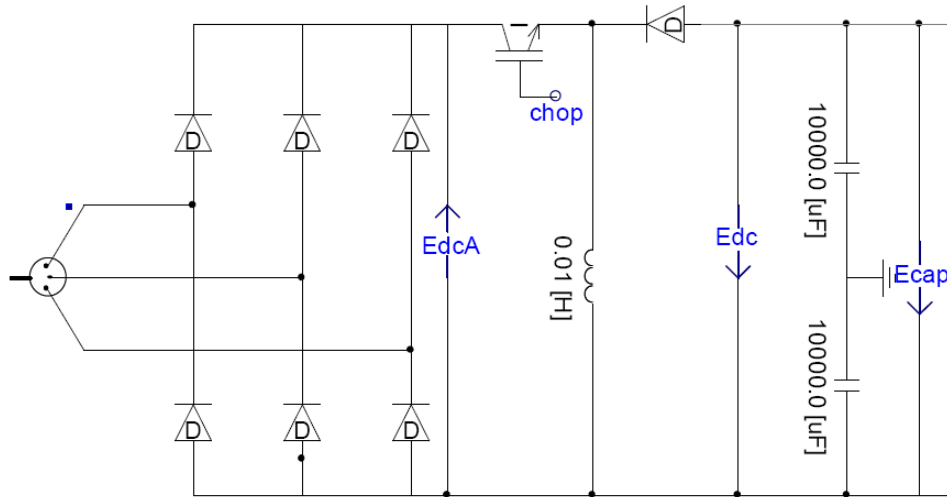


Figure 6.5: Rectifier and buck/boost converter circuit

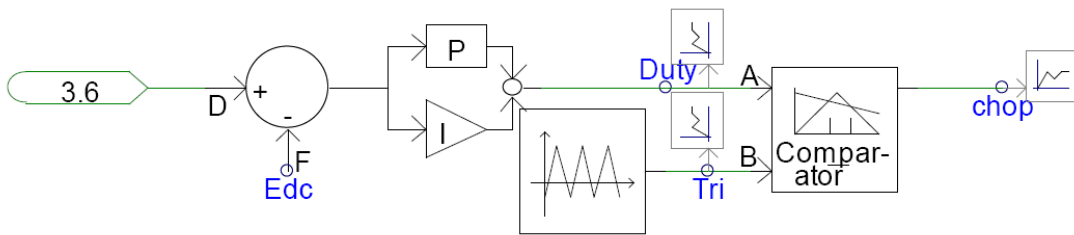


Figure 6.6: Buck/boost converter controller

### 6.2.6 Inverter

The inverter implemented here (shown in Figure 6.7) is a current controlled voltage-source inverter. It is capable of decoupling real and reactive power control, since the controller design for this inverter is based on flux-vector theory. Real and reactive power reference signals are compared with actual values and the error is used to drive two independent PI controllers, as shown in Figure 6.8. The real power error drives the  $I_q$  signal, while reactive power error drives the  $I_d$  signal. These  $dq0$  domain values are converted to reference  $I_{abc}$  values as shown in Figure 6.9 (note that the angle signal  $phis$  is calculated from the voltage phasor). The reference  $I_{abc}$  currents are compared with actual currents and a hysteresis controller (shown in Figure 6.10) switches the inverter IGBTs such that actual current follows the reference current. When the reference currents are achieved, reference real and reactive power is also achieved. Fig 6.11 shows the reference current and the actual current. The actual current can be seen to be closely following the reference current.

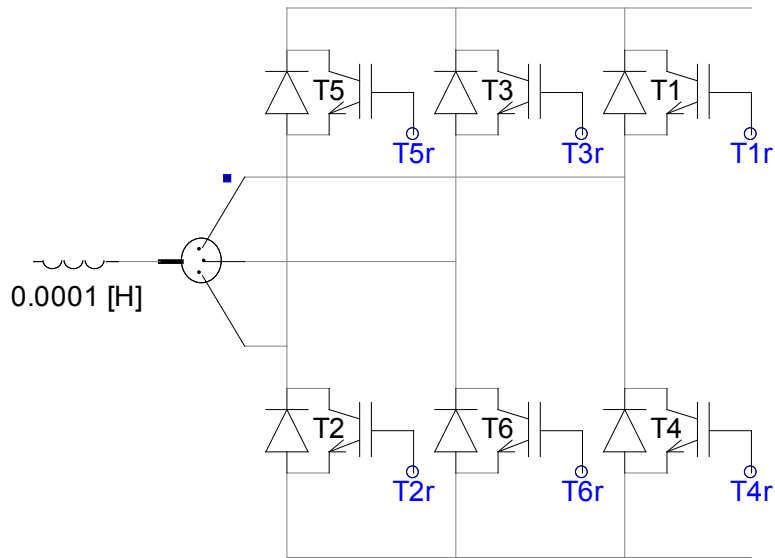


Figure 6.7: Inverter (current controlled VSI).

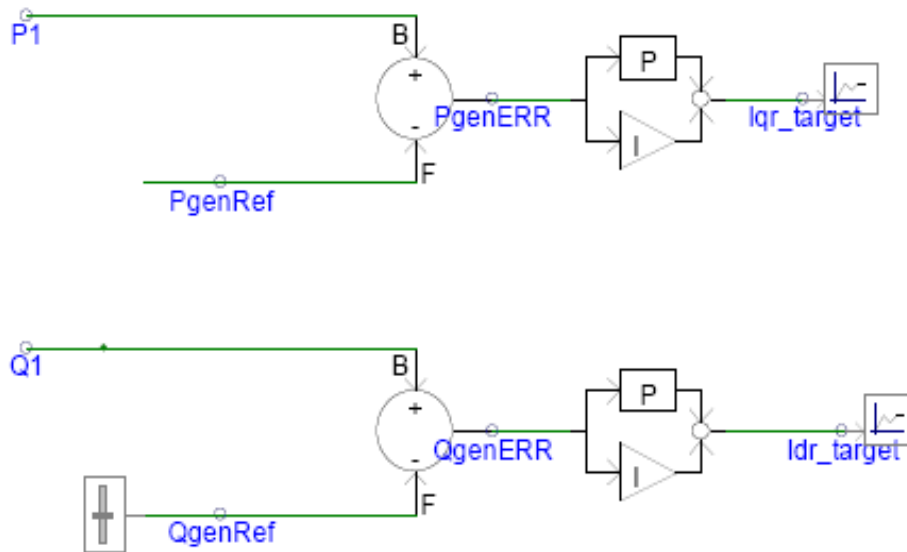


Figure 6.8: Real and reactive power errors drive q- and d-axis current controllers respectively.

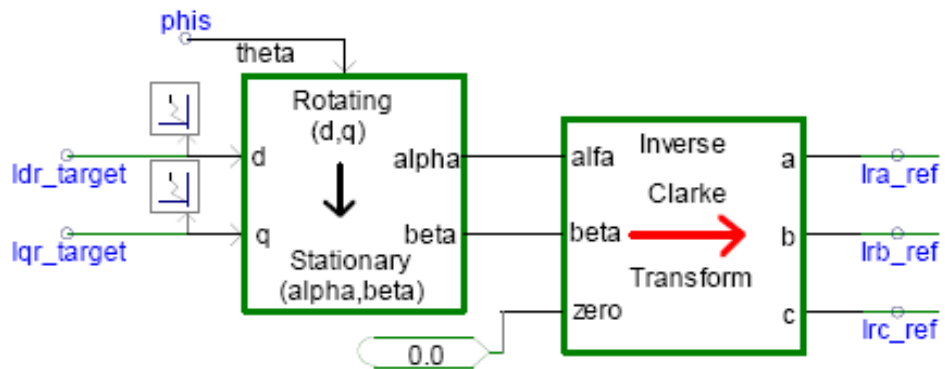


Figure 6.9: Currents are converted from dq0 domain to the abc domain.

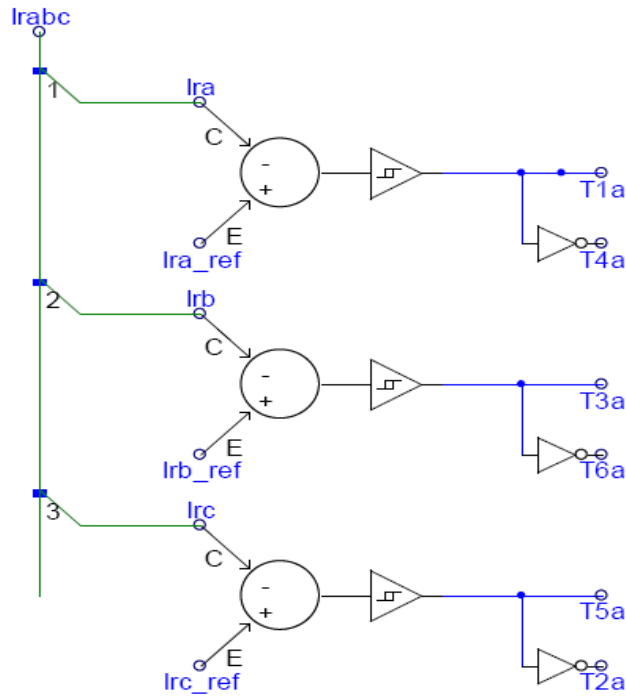


Figure 6.10: Hysteresis control used to achieve reference currents.

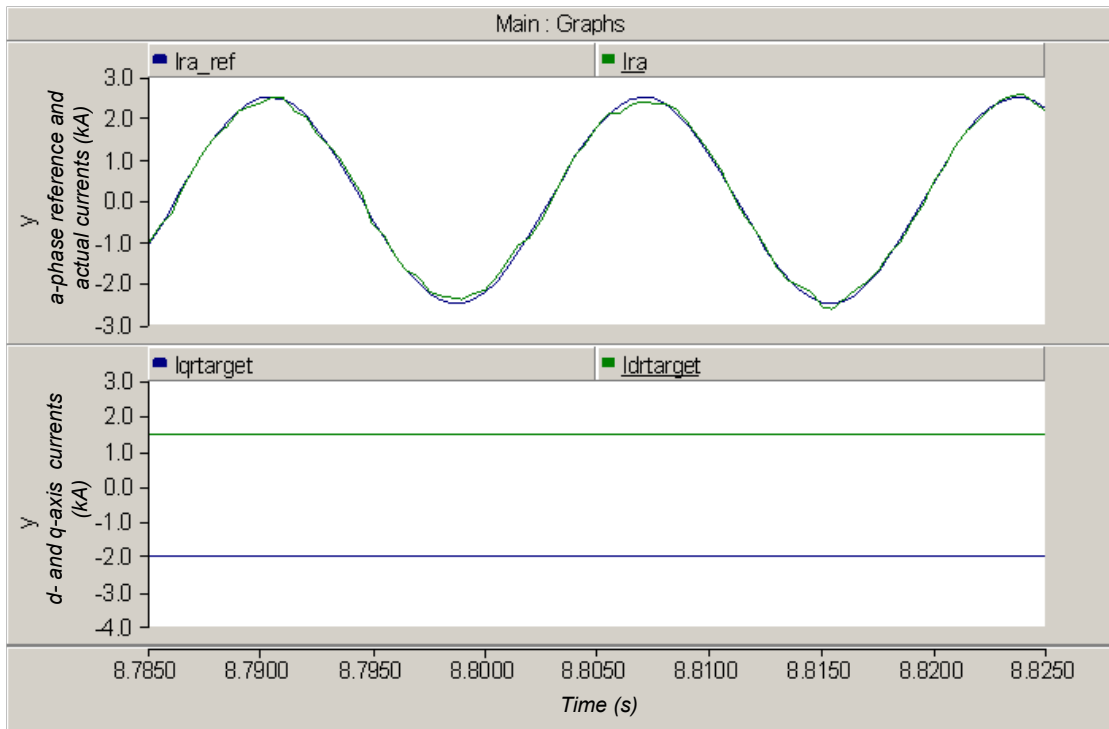


Figure 6.11: Actual a-phase current closely follows the reference current.

### 6.2.7 Unit transformer and grid representation

The unit transformer and grid are both modeled using in-built blocks supplied by PSCAD/EMTDC. The unit transformer is a wye-delta 2-MVA transformer with a primary voltage of 34.5 kV and a secondary voltage of 0.6 kV, and a per unit leakage reactance of 0.1 p.u. During the development and testing phase, the grid is represented by a 34.5-kV voltage source.

### 6.2.8 Complete model implemented in PSCAD/EMTDC

Figure 6.12 shows the complete model, not including the various control blocks, after all the individual subsystems have been assembled. Figure 6.13 shows the user controls that can be used to modify wind speed and reactive power demand. In the next section, the complete model testing is described.

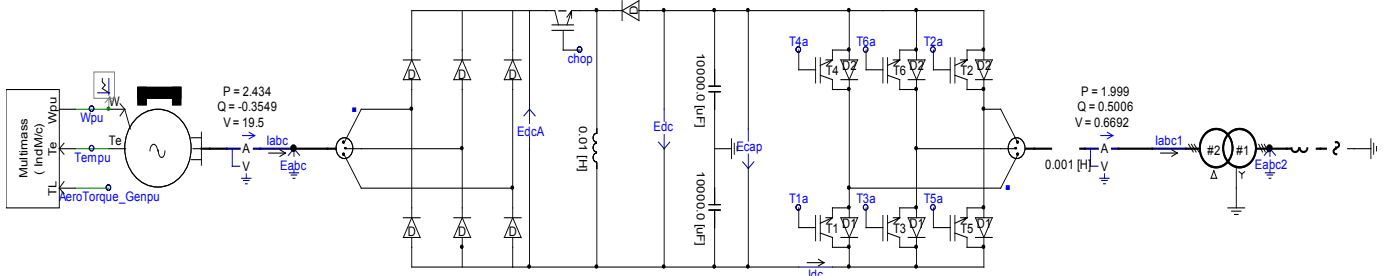


Figure 6.12: Complete model (not including controls and calculation blocks).

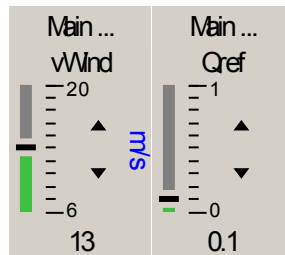


Figure 6.13: User inputs

### 6.3 Model Testing

The model testing phase is essential to evaluate the capabilities of the model. The model testing phase has three main objectives:

- To verify that desired wind turbine power curve is achieved;
- To demonstrate independent real and reactive power control;
- To demonstrate pitch controller action.

If the model is able to meet these objectives, we can use it with confidence as a platform for modeling more advanced controls, such as providing inertia and frequency response.

#### 6.3.1 Power curve

The desired power curve is a cubic function of per unit wind speed (up to rated wind speed). Rated power is achieved at rated wind speed. Beyond rated wind speed, the desired power is flat at rated power. Thus, the curve has sharp edge at rated wind speed. This edge needs to be smoothed out, or else the model will have stability issues around the rated wind speed. The smoothed curve is the one actually implemented in the reference power calculation block discussed earlier. Rated power is thus achieved at 14 m/s rather than 13 m/s, as shown in Figure 6.14. Figure 6.15 shows the actual output of the simulation. From Figure 6.15, the power output tracks the desired (softened) curve closely. The plot is obtained from a PSCAD/EMTDC simulation multi-run to ensure that the power output measured for each wind speed is the steady-state value. Thus, we can claim that that the first objective, that of achieving the desired power curve, is met.

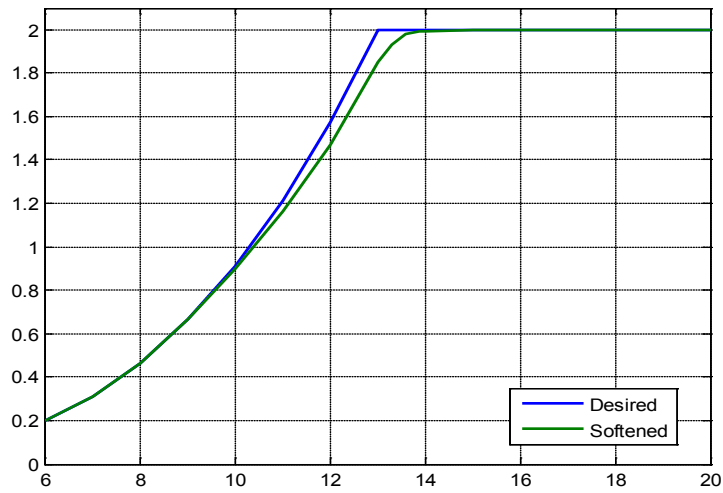


Figure 6.14: Softening of power curve.

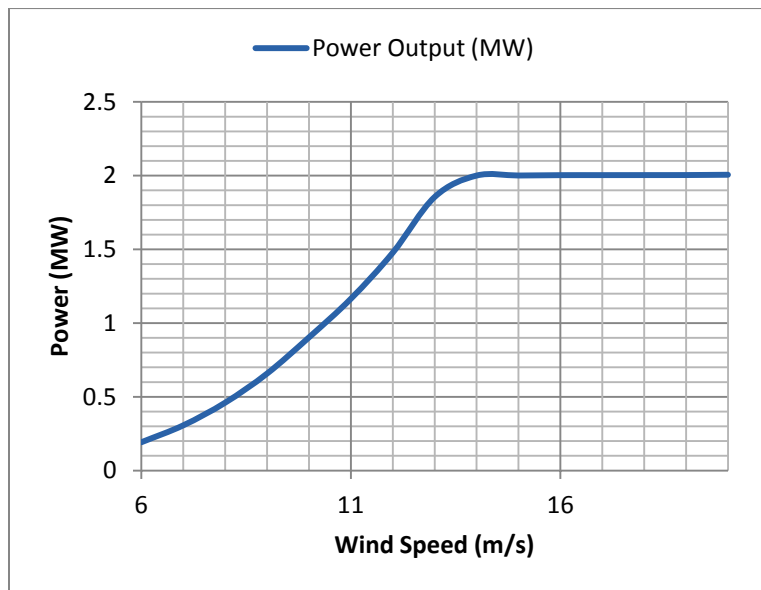


Figure 6.15: Power curve from simulation.

Table 6.1: Data for power curve and slip.

$V_{wind}$ m/s	Power Out MW
6	0.192
7	0.307
8	0.460
9	0.903
10	1.165
11	1.477
12	1.855
13	2.0
14	2.0
15	2.0
16	2.0
17	2.0
18	2.0
19	2.0
20	2.0

### 6.3.2 Independent real and reactive power control

To test if independent real and reactive power control has been achieved, four tests were carried out: real power drop, reactive power drop, real power rise, and reactive power rise. Each of these is modeled as a step change, i.e., at a particular instant, the simulation was paused and a step change was made to either the wind speed or reactive power demand. In the first test, a real power drop was simulated. The wind speed was changed from 13 m/s to 11 m/s at  $t=12$ s. The reactive power demand was set at 0.4 MVAR. The result is shown in Figure 6.16(a). The real power output drops and settles to the new value. Reactive power drops initially, but recovers to the original value. In the second test, a reactive power drop was simulated. The result is shown in Figure 6.16(b). The wind speed remains at 13 m/s throughout the run, but reactive power demand was changed from 0.5 MVAR to 0.2 MVAR at  $t=12$ s. The reactive power dropped, as expected. The real power output shows a slight perturbation, but recovers to the original value. In the third test, a real power rise was simulated. The wind speed was changed from 11 m/s to 15 m/s at  $t=12$ s. The reactive power demand was set at 0.4 MVAR. The result is shown in Figure 6.16(c). The real power output rises and settles to the new value. Reactive power rises initially but recovers to the original value. In the fourth test, a reactive power rise was simulated. The result is shown in Figure 6.16(d). The wind speed remains at 13 m/s throughout the run, but reactive power demand was changed from 0.5 MVAR to 0.7 MVAR at  $t=12$ s. The reactive power rose, as expected. The real power output once again shows a slight perturbation but recovers to the original value.

Consider the real power drop shown in Figure 5.18(a). In this case, when wind speed drops suddenly, the pitch controller is de-activated, and the pitch angle moves quickly to zero. This is likely the cause for the overshoot observed in the power waveform. Within the wind turbine control system, the change in wind speed changes the  $P_{genref}$  value. At this instant, the error between  $P_{genref}$  and the actual power output becomes large, driving a change (reduction) in the value of  $q$ -axis current  $I_q$ . The  $d$ -axis current does not change since the reactive power set-point is not changed. This change in  $I_q$  leads to a corresponding change in the three-phase currents, leading to the desired change in the real power output. The reactive power output stays constant at the set-point. It should be noted that the decoupling effect observed here for Type 4 turbines is even more pronounced than in the Type 3 turbine described in the last chapter, especially under the transient conditions. The reason for this is that the Type 4 turbine is completely decoupled from the grid, unlike the Type 3 turbine in which flux linkages in the stator can be momentarily affected by transients on the grid side. The results here conclusively show that a change in either real power or reactive power demand does not affect the other quantity. Based on the results of the testing, we can claim that the objective of independent real and reactive power control has been achieved.

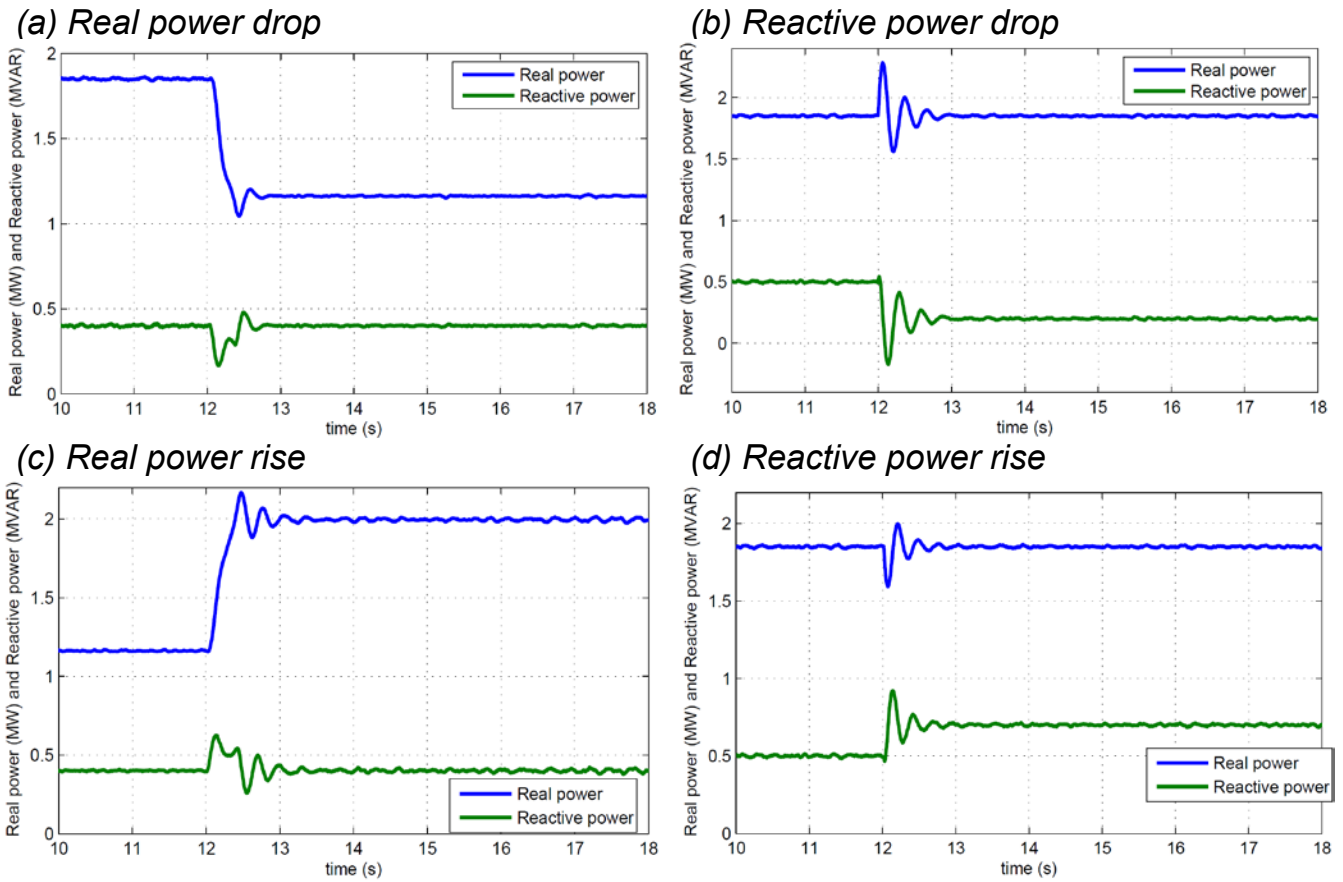


Figure 6.16: Test of decoupling of real and reactive power output for Type 4 turbine model.

### 6.3.3 Pitch control

A test was devised to evaluate pitch controller action. The wind speed changed from 11 m/s to 15 m/s at  $t=25$ s. The pitch angle was initially at 0 degrees (i.e., the pitch controller was inactive). From the results shown in Figure 6.17, it can be seen that the pitch controller becomes active when wind speed change occurs. This occurs due to new wind speed (15 m/s) being higher than rated. Eventually, the pitch angle settles close to -8 degrees, effectively spilling some excess power. It should be noted that the pitch angle values are inverted (negative rather than positive) due to the  $C_p$  lookup table characteristics; -8 degrees here thus corresponds to 8 degrees in the real world. The test shows that the pitch controller does indeed work in a stable fashion.

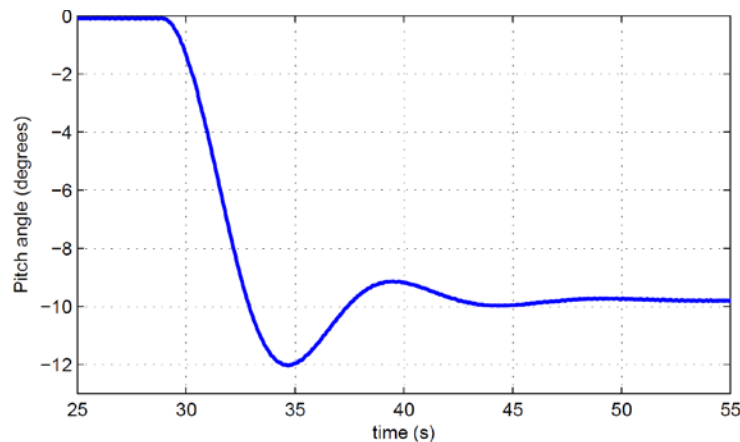
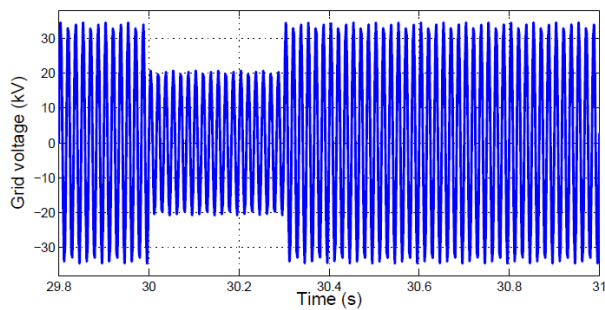


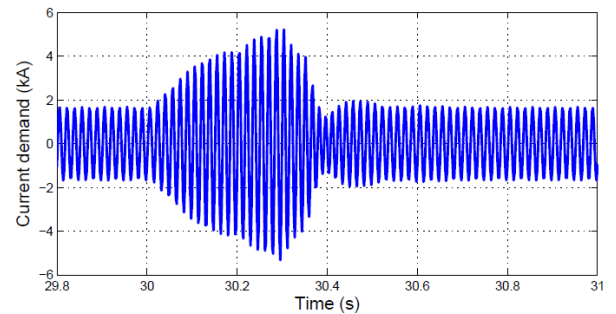
Figure 6.17: Pitch control action.

## 6.4 Dynamic Response

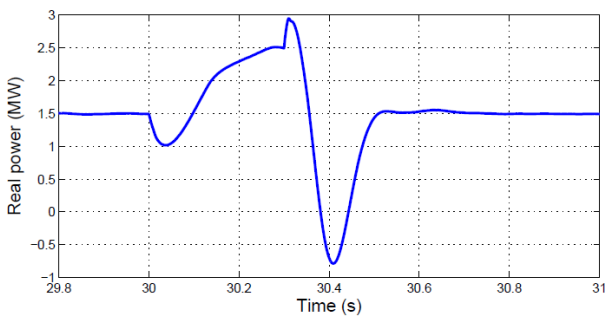
To demonstrate the model's ability to reproduce wind turbine dynamics, a test was created. The wind turbine was operated with a constant wind speed (15 m/s). This wind speed was higher than rated wind speed and hence, the pitch controller was active. A voltage sag on the grid was simulated, and the real and reactive power response of the wind turbine was observed. Note that this is not an implementation of low-voltage ride through (LVRT), but rather a test of dynamic response. The grid voltage drops from 1 p.u. to 0.6 p.u. at  $t=30$ s, and the sag persists for 18 cycles (0.3 seconds). The intent of the test is to show that the model does indeed respond to events occurring in the dynamic timescale and that the response of the machine to this event is realistic. Fig. 6.18 shows the results of the test, and shows that the model does indeed respond to the grid event as expected. The grid voltage, converter current demand, real power and reactive power, rotor speed, and pitch angle during the event are shown.



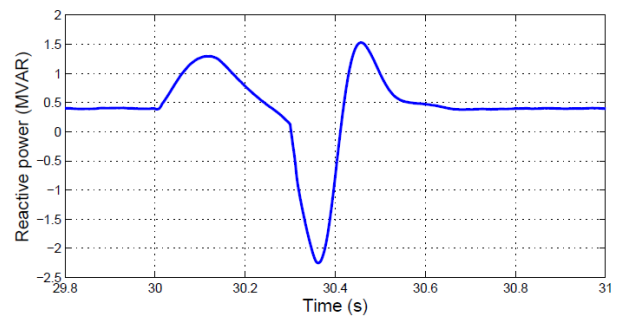
(a) Grid voltage



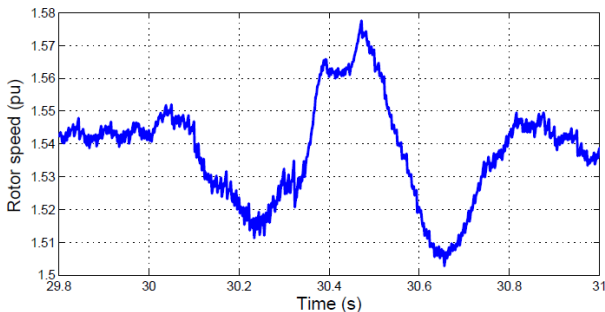
(b) Converter current demand



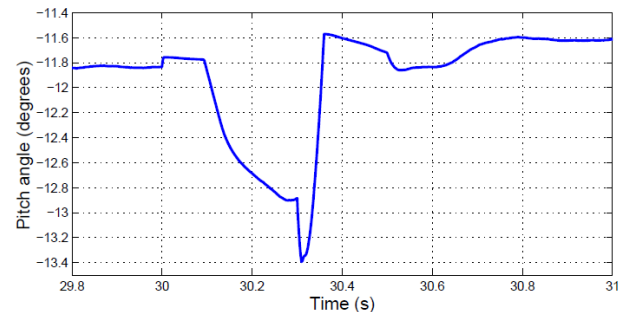
(c) Real power



(d) Reactive power



(e) Rotor speed



(f) Pitch angle

Figure 6.18: Real and reactive power response during voltage sag on the grid.

From Fig. 6.18, it can be seen that real and reactive power show a sharp increase when the event starts. This is due to the grid-side converter attempting to maintain real power output at 2 MW despite the voltage drop occurring. The converter greatly increases the current demand from the generator, which reflects as a jump in power. The pitch controller also seeks to maintain real power output at 2 MW, and hence, begins to move to a lower angle to counter the effects of the converter action. Based on these results, we can say that the model is behaving as expected, and realistic explanations for the response can be offered. The transients when the voltage sag occurs and when the sag ends are also visible. We can thus claim that the model described here offers good resolution and detail. This event is similar to the event used for testing purposes in [60] which offers a useful comparison: the voltage drop was from 1 p.u. to 0.5 p.u. and the sag persisted for 0.5 seconds. The power electronic converters are not explicitly modeled in [60], and the topology and controls are also different from those presented here, leading to a considerable difference in results.

## 6.5 Summary

The development and testing of a full converter wind turbine employing a permanent magnet alternator has been presented here. This model is unique in that it employs a buck-boost converter to control DC link voltage. The modeling framework used is unrestricted, manufacturer-independent, and can be implemented in any dynamic modeling software. The model subsystems have been described individually, as have the signals exchanged between these subsystems when assembled into the complete model. Details of model parameters have been provided to allow reproduction of the results shown here. The model testing objectives and methods have also been presented. The power curve requirements have been met, decoupled real and reactive power control requirements have been met, and the pitch controller works as expected. An example of the model's dynamic response has also been provided. In the future, the model can be used as a platform to model various controls such as those needed to provide LVRT and inertial support.

## 7. Conclusion and Future Work

### 7.1 Conclusion

The primary objective of the work outlined in this proposal was to provide a reliable dynamic modeling platform, and the objective has been met. The secondary objective was to use the models for stability studies, and this objective has also been met. In summary, the completion of the project yielded the following technical contributions:

- A suite of generic, manufacturer-independent, physics-based analytical wind turbine and wind power plant models implemented in PSCAD/EMTDC, allowing a wide variety of grid integration issues can be studied,
- Evaluation of dynamic response of each of the four different basic types of wind turbine, from which the broad conclusion can be drawn that wind turbines which employ power electronic converters (Types 3 and 4) offer a more muted response to voltage sag events on the grid,
- For DFIG (Type 3) turbines, representing entire wind power plant as a unified current source was seen to yield realistic results,
- An “equivalencing” technique, previously used in steady-state models, for reducing wind power plant collector systems to single-line representation has been tested and evaluated for dynamic models and found to be valid,
- Development of a validation technique for validation of models using real data, and employment of this technique to validate a DFIG wind power plant model.

### 7.2 Future Work

In future work, these models will be used for the following purposes:

- To model inertia/frequency support schemes,
- To model sub-synchronous control interactions of wind power plants with the power system,
- To model schemes with wind power plants providing other ancillary services, such as reactive power and voltage control,
- To model interaction of wind power plants with storage and conventional generation, and
- To model wind power plant system protection.

In conclusion, the models provide a useful platform for those in industry or academia to conduct their own investigations into the effects of wind integration on power systems. These models are intended to be “enabling technology” for those who have an interest in wind power to evaluate its impacts on system stability, and to model new controls and techniques for facilitating wind power integration. The broader aim of this project is to allay anxiety about the integration of wind power and speed its adoption.

## Appendices

## Appendix A: Wind Turbine Ratings and Parameters

### A.1 Fixed-Speed (Type 1) Single Turbine Estimated Ratings and Parameters (note: parameters modified for consistency across turbine types)

Table A.1: Type 1 Turbine Example Case.

<i>Turbine make</i>	<i>NEG Micon NM72C 1.5MW</i>
<i>Regulation method</i>	<i>Active stall (disabled)</i>
<i>Rotor diameter</i>	<i>72m</i>
<i>Hub height</i>	<i>62m or 78m</i>
<i>Number of blades</i>	<i>3</i>
<i>Cut-in wind speed</i>	<i>4 m/s</i>
<i>Cut-out wind speed</i>	<i>20 m/s</i>
<i>Rated wind speed</i>	<i>13 m/s</i>
<i>Rotor speed</i>	<i>17.3rpm</i>

Table A.2: Type 1: Induction generator ratings.

<i>Rated MVA</i>	<i>1.5 MVA</i>
<i>Rated Voltage</i>	<i>0.69 kV line-to-line</i>
<i>Number of poles</i>	<i>6</i>
<i>Rated frequency</i>	<i>60 Hz</i>
<i>Stator/rotor turns ratio</i>	<i>0.379</i>

Table A.3: Type 1: Induction generator parameters.

<i>Stator winding resistance</i>	<i>0.0047 pu</i>
<i>Squirrel-cage resistance</i>	<i>0.0021 pu</i>
<i>Stator leakage inductance</i>	<i>0.08 pu</i>
<i>Squirrel-cage inductance</i>	<i>0.0478 pu</i>
<i>Magnetizing inductance</i>	<i>6.8 pu</i>
<i>Angular moment of inertia</i>	<i>0.578 s</i>

### A.2 Variable-Slip (Type 2) Single Turbine Estimated Ratings and Parameters (note: parameters modified for consistency across turbine types)

Table A.4: Type 2 Turbine Example Case.

<i>Turbine make</i>	<i>Vestas V63 1.5MW</i>
<i>Regulation method</i>	<i>Pitch control (disabled)</i>
<i>Rotor diameter</i>	<i>63m</i>
<i>Hub height</i>	<i>64m</i>
<i>Number of blades</i>	<i>3</i>
<i>Cut-in wind speed</i>	<i>4 m/s</i>
<i>Cut-out wind speed</i>	<i>20 m/s</i>
<i>Rated wind speed</i>	<i>13 m/s</i>
<i>Rotor speed</i>	<i>19/15 rpm</i>

Table A.5: Type 2: Induction generator ratings.

<i>Rated MVA</i>	<i>1.5 MVA</i>
<i>Rated Voltage</i>	<i>0.69 kV line-to-line</i>
<i>Number of poles</i>	<i>6</i>
<i>Rated frequency</i>	<i>60 Hz</i>
<i>Stator/rotor turns ratio</i>	<i>0.379</i>

Table A.6: Type 2: Induction generator parameters.

<i>Stator winding resistance</i>	<i>0.005 pu</i>
<i>Wound rotor resistance (int)</i>	<i>1e-6 pu</i>
<i>Wound rotor resistance (ext)</i>	<i>0.0021 pu</i>
<i>Stator leakage inductance</i>	<i>0.08 pu</i>
<i>Squirrel-cage inductance</i>	<i>0.0478 pu</i>
<i>Magnetizing inductance</i>	<i>6.8 pu</i>
<i>Angular moment of inertia</i>	<i>0.578 s</i>

### A.3 Doubly-Fed Induction Generator (Type 3) Single Turbine Estimated Ratings and Parameters (note: parameters modified for consistency across turbine types)

Table A.7: Type 3 Turbine Example Case.

<i>Turbine make</i>	<i>GE 1.5MW</i>
<i>Regulation method</i>	<i>Pitch control (enabled)</i>
<i>Rotor diameter</i>	<i>70.5m</i>
<i>Hub height</i>	<i>65m</i>
<i>Number of blades</i>	<i>3</i>
<i>Cut-in wind speed</i>	<i>4 m/s</i>
<i>Cut-out wind speed</i>	<i>20 m/s</i>
<i>Rated wind speed</i>	<i>12 m/s (13 m/s used)</i>
<i>Rotor speed</i>	<i>11/22 rpm</i>

Table A.8: Type 3: Induction generator ratings.

<i>Rated MVA</i>	<i>1.5 MVA</i>
<i>Rated Voltage</i>	<i>0.575 kV line-to-line</i>
<i>Number of poles</i>	<i>6</i>
<i>Rated frequency</i>	<i>60 Hz</i>
<i>Stator/rotor turns ratio</i>	<i>0.379</i>

Table A.9: Type 3: Induction generator parameters.

<i>Stator winding resistance</i>	<i>0.0071 pu</i>
<i>Wound rotor resistance (int)</i>	<i>0.005 pu</i>
<i>Stator leakage inductance</i>	<i>0.1714 pu</i>
<i>Squirrel-cage inductance</i>	<i>0.1563 pu</i>
<i>Magnetizing inductance</i>	<i>2.9 pu</i>
<i>Angular moment of inertia</i>	<i>0.5 s</i>

## A.4 Full-Converter (Type 4) Single Turbine Estimated Ratings and Parameters (note: parameters modified for consistency across turbine types)

Table A.10: Type 4 Turbine Example Case.

<i>Turbine make</i>	<i>Enercon E82 2MW</i>
<i>Regulation method</i>	<i>Pitch control (enabled)</i>
<i>Rotor diameter</i>	<i>82m</i>
<i>Hub height</i>	<i>78m</i>
<i>Number of blades</i>	<i>3</i>
<i>Cut-in wind speed</i>	<i>4 m/s</i>
<i>Cut-out wind speed</i>	<i>28 m/s</i>
<i>Rated wind speed</i>	<i>15 m/s (14 m/s used)</i>
<i>Rotor speed</i>	<i>6/18 rpm</i>

Table A.11: Type 4: Permanent magnet alternator ratings.

<i>Rated MVA</i>	<i>2 MVA</i>
<i>Rated Voltage</i>	<i>3.6 kV line-to-line</i>
<i>Rated frequency</i>	<i>60 Hz</i>

Table A.12: Type 4: Permanent magnet alternator parameters.

<i>Stator winding resistance</i>	<i>0.017 pu</i>
<i>Stator leakage reactance</i>	<i>0.064 pu</i>
<i>d-axis unsaturated reactance</i>	<i>0.55 pu</i>
<i>q-axis unsaturated reactance</i>	<i>1.11 pu</i>
<i>d-axis damper winding resistance</i>	<i>0.62 pu</i>
<i>d-axis damper winding reactance</i>	<i>0.183 pu</i>
<i>q-axis damper winding resistance</i>	<i>1.11 pu</i>
<i>q-axis damper winding reactance</i>	<i>1.175 pu</i>
<i>Magnetic strength*</i>	<i>5 pu</i>

\* The flux linkage due to the permanent magnet (measured in kWb-turns). One p.u. magnetic strength will produce rated terminal voltage when machine is rotating at rated speed and at no-load.

## Appendix B: Fifth- and Third-Order Equations for Induction Machines

### B.1 Fifth-Order Model

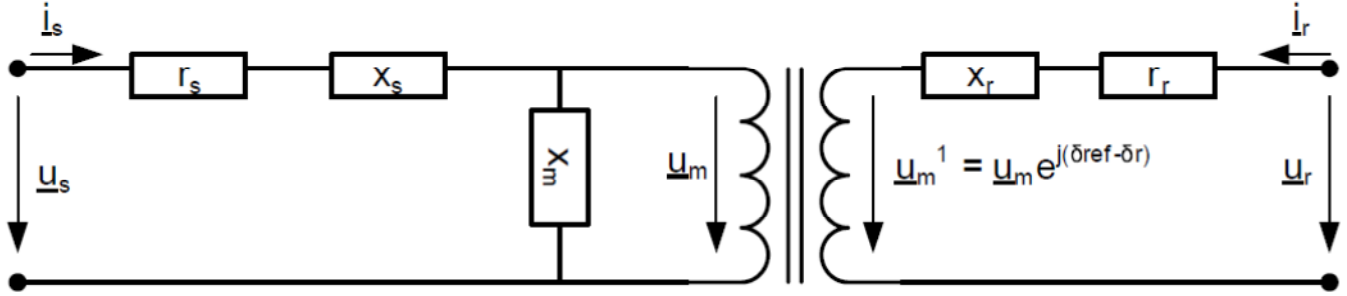


Figure B.1: Induction generator equivalent circuit.

Figure B.1 [12] shows the equivalent circuit diagram of the doubly-fed induction generator, from which the model equations can be derived. The equations are derived in a frame which is rotating at a constant speed  $\omega_{ref}$ . The resulting equations for stator and rotor are:

$$\underline{u}_s = r_s \underline{i}_s + \frac{1}{\omega_n} \frac{d\underline{\psi}_s}{dt} + j \underline{\psi}_s \frac{\omega_{ref}}{\omega_n} \quad (B.1)$$

$$u_r = r_r \underline{i}_r + \frac{1}{\omega_n} \frac{d\underline{\psi}_r}{dt} + j \underline{\psi}_r \frac{\omega_{ref} - \omega_g}{\omega_n} \quad (B.2)$$

In the above equations,  $\underline{u}$  denotes voltage,  $\underline{\psi}$  denotes flux,  $\underline{i}$  denotes current,  $x$  denotes reactance and  $r$  denotes resistance. The flux linkages can be expressed as:

$$\underline{\psi}_s = (x_s + x_m) \underline{i}_s + x_m \underline{i}_r \quad (B.3)$$

$$\underline{\psi}_r = x_m \underline{i}_s + (x_m + x_r) \underline{i}_r \quad (B.4)$$

The induction machine model also includes the following mechanical equation:

$$J \frac{d\omega_g}{dt} = t_{mech} + t_{elec} \quad (B.5)$$

The electrical torque can be calculated from the stator current and flux (note that all quantities are in per unit referred to the stator side):

$$t_{elec} = \text{Im}(\underline{\psi}_s + \underline{i}_s^*) \quad (B.5)$$

### B.2 Third-Order Model

A model derived from the aforementioned equations can represent the majority of transients on the rotor and stator. A third-order model can be derived for studies that require a lower resolution (higher time step), i.e., where computational power is a constraint (note that the mechanical equation is the same as for the fifth-order model):

$$\underline{u}_s = r_s \underline{i}_s + j \underline{\psi}_s \frac{\omega_{ref}}{\omega_n} \quad (B.1)$$

$$u_r = r_r \underline{i}_r + \frac{1}{\omega_n} \frac{d\underline{\psi}_r}{dt} + j \underline{\psi}_r \frac{\omega_{ref} - \omega_g}{\omega_n} \quad (B.2)$$

## Bibliography

- [1] P. Kundur, N. Balu, and M. Lauby, *Power system stability and control*. McGraw-Hill Professional, 1994.
- [2] S. Lindenberg, B. Smith, K. O'Dell, and E. DeMeo, "20 Percent Wind Energy by 2030: Increasing Wind Energy's Contribution to U.S. Electricity Supply," tech. rep., U.S. Department of Energy, July 2008. Available at <http://www.nrel.gov/docs/fy08osti/41869.pdf>.
- [3] "Global wind 2008 report." Global Wind Energy Council, 2009. Available at <http://www.gwec.net/fileadmin/documents/Publications/Global%20Wind%202008%20Report.pdf>.
- [4] R. Redlinger, P. Andersen, and P. Morthorst, *Wind energy in the 21<sup>st</sup> century: Economics, policy, technology, and the changing electricity industry*. Palgrave Macmillan, 2002.
- [5] P. Ledesma, J. Usaola, and J. Rodriguez, "Transient stability of a fixed speed wind farm," *Renewable Energy*, vol. 28, no. 9, pp. 1341–1355, 2003.
- [6] D. Trudnowski, A. Gentile, J. Khan, and E. Petritz, "Fixed-speed wind generator and wind-park modeling for transient stability studies," *IEEE Transactions on Power Systems*, vol. 19, no. 4, pp. 1911–1917, 2004.
- [7] V. Akhmatov, H. Knudsen, A. Hejde Nielsen, J. Kaas Pedersen, and N. Kjølstad Poulsen, "Modelling and transient stability of large wind farms," *International Journal of Electrical Power and Energy Systems*, vol. 25, no. 2, pp. 123–144, 2003.
- [8] E. Muljadi, C. Butterfield, B. Parsons, and A. Ellis, "Effect of variable speed wind turbine generator on stability of a weak grid," *IEEE Transactions on Energy Conversion*, vol. 22, no. 1, pp. 29–36, 2007.
- [9] I. Erlich, J. Kretschmann, J. Fortmann, S. Mueller-Engelhardt, and H. Wrede, "Modeling of wind turbines based on doubly-fed induction generators for power system stability studies," *IEEE Transactions on Power Systems*, vol. 22, no. 3, pp. 909–919, 2007.
- [10] P. Eriksen, T. Ackermann, H. Abildgaard, P. Smith, W. Winter, and J. Rodriguez Garcia, "System operation with high wind penetration," *IEEE power & energy magazine*, vol. 3, no. 6, pp. 65–74, 2005.
- [11] V. Akhmatov, *Analysis of dynamic behaviour of electric power systems with large amount of wind power*. PhD thesis, Electric Power Engineering, Oersted-DTU, Technical University of Denmark, 2003. Available at <http://www.studenterpraest.dtu.dk/upload/centre/cet/projekter/05-va-thesis.pdf>.
- [12] M. Pöller, "Doubly-fed induction machine models for stability assessment of wind farms," in *IEEE Power Tech. Conference*, (Bologna, Italy), June 2003.
- [13] C. Johnson and R. Smith, "Dynamics of wind generators on electric utility networks," *IEEE Transactions on Aerospace and Electronic Systems*, pp. 483–493, 1976.
- [14] H. Davitian, "Wind power and electric utilities: a review of the problems and prospects," *Wind Engineering*, vol. 2, no. 4, pp. 234–255, 1978. Available at <http://www.entekpower.com/Papers/Windpower%20and%20Electric%20Utilities.pdf>.

- [15] H. Zaininger and D. Bell, "Potential dynamic impacts of wind turbines on utility systems," *IEEE Transactions on Power Apparatus and Systems*, pp. 4821–4829, 1981.
- [16] E. Hinrichsen and P. Nolan, "Dynamics and stability of wind turbine generators," *IEEE Transactions on Power Apparatus and Systems*, pp. 2640–2648, 1982.
- [17] P. Anderson and A. Bose, "Stability simulation of wind turbine systems," *IEEE Transactions on Power Apparatus and Systems*, pp. 3791–3795, 1983.
- [18] S. Chan, R. Cresap, and D. Curtice, "Wind turbine cluster model," *IEEE Transactions on Power Apparatus and Systems*, pp. 1692–1698, 1984.
- [19] J. Sloopweg, H. Polinder, and W. Kling, "Dynamic modelling of a wind turbine with doubly fed induction generator," in *IEEE Power Engineering Society Summer Meeting*, vol. 1, pp. 644–649 vol.1, 2001.
- [20] T. Ackermann, *Wind power in power systems*. John Wiley Chichester, West Sussex, England, 2005.
- [21] Siemens PTI, *PSS/E 30.2 Program Operational Manual*, 2nd ed., 2005.
- [22] H. Fankhauser, K. Aneros, A.-A. Edris, and S. Torseng, "Advanced simulation techniques for the analysis of power system dynamics," *Computer Applications in Power, IEEE*, vol. 3, pp. 31–36, oct 1990.
- [23] Manitoba HVDC Research Centre, *EMTDC: Transient Analysis for PSCAD Power System Simulation*, 4.2 ed., April 2005. Available at [https://pscadd.com/resource/File/PSCADV421Student/EMTDC\\_Users\\_Guide\\_V4.2.pdf](https://pscadd.com/resource/File/PSCADV421Student/EMTDC_Users_Guide_V4.2.pdf).
- [24] E. Muljadi and A. Ellis, "Validation of wind power plant models," in *2008 IEEE Power and Energy Society General Meeting-Conversion and Delivery of Electrical Energy in the 21st Century*, pp. 1–7, 2008.
- [25] M. Behnke, A. Ellis, Y. Kazachkov, T. McCoy, E. Muljadi, W. Price, and J. Sanchez-Gasca, "Development and validation of WECC variable speed wind turbine dynamic models for grid integration studies," in *AWEA WindPower Conference*, 2007.
- [26] L. Hansen, P. Madsen, F. Blaabjerg, H. Christensen, U. Lindhard, and K. Eskildsen, "Generators and power electronics technology for wind turbines," in *The 27th Annual Conference of the IEEE Industrial Electronics Society (IECON)*, vol. 3, pp. 2000–2005, 2001.
- [27] J. Baroudi, V. Dinavahi, and A. Knight, "A review of power converter topologies for wind generators," in *IEEE International Conference on Electric Machines and Drives*, pp. 458–465, May 2005.
- [28] M. Singh and S. Santoso, "Electromechanical and Time-Domain Modeling of Wind Generators," in *IEEE Power Engineering Society General Meeting*, (Tampa, FL), June 2007.
- [29] S. Santoso, M. Singh, D. Burnham, and E. Muljadi, "Dynamic modeling of wind turbines," tech. rep., University of Texas at Austin and National Renewable Energy Laboratory, 2009.
- [30] S. Santoso, M. Singh, and E. Muljadi, "Modeling and validation of doubly-fed induction generator wind turbines," tech. rep., University of Texas at Austin and National Renewable Energy Laboratory, 2008.

- [31] M. Singh, K. Faria, S. Santoso, and E. Muljadi, "Validation and analysis of wind power plant models using short-circuit field measurement data," in *IEEE Power and Energy Society General Meeting*, (Calgary, AB), July 2009.
- [32] S. Santoso, M. Singh, E. Muljadi, and V. Gevorgian, "Dynamic model of full-converter PMSG wind turbine with frequency response controls," tech. rep., University of Texas at Austin and National Renewable Energy Laboratory, 2011.
- [33] M. Singh and S. Santoso, "Dynamic model for full-converter wind turbines employing permanent magnet alternators," in *IEEE Power Engineering Society General Meeting*, (Detroit, MI), July 2011.
- [34] M. Vyas, M. Singh, and S. Santoso, *Handbook of Wind Power Systems*, ch. Grid Integration of Wind Power Systems: Modeling of Wind Power Plants. Springer, 2011.
- [35] M. Singh, M. Vyas, and S. Santoso, "Using generic wind turbine models to compare inertial response of wind turbine technologies," in *IEEE Power and Energy Society General Meeting*, (Minneapolis, MN), July 2010.
- [36] J. Slootweg and W. Kling, "Aggregated modeling of wind parks in power system dynamics simulations," in *IEEE Power Tech. Conference*, (Bologna, Italy), June 2003.
- [37] M. Uctug, I. Eskandarzadeh, and H. Ince, "Modelling and output power optimisation of a wind turbine driven double output induction generator," *IEE Proceedings - Electric Power Applications*, vol. 141, pp. 33–38, mar 1994.
- [38] S.-K. Kim, E.-S. Kim, J.-Y. Yoon, and H.-Y. Kim, "PSCAD/EMTDC based dynamic modeling and analysis of a variable speed wind turbine," in *IEEE Power Engineering Society General Meeting*, (Denver, CO), pp. 1735–1741, Vol.2, june 2004.
- [39] R. Gagnon, G. Sybille, S. Bernard, D. Pare, S. Casoria, and C. Larose, "Modeling and Real-Time Simulation of a doubly-fed induction generator driven by a wind turbine," in *Proceedings of the International Conference on Power systems Transients (IPST '05)*, (Montreal, QC), pp. 19–23, 2005.
- [40] A. Betz, "Wind Energy and its Exploitation by Windmills," *Gottingen: Van-denhoeck und Ruprecht*, p. 64, 1926.
- [41] H. Glauert, "Windmills and fans," *Aerodynamic theory*, vol. 3, 1935.
- [42] J. Manwell and J. McGowan, *Wind energy explained: theory, design and application*. Wiley Chichester, 2003.
- [43] R. Delmerico, N. Miller, W. Price, and J. Sanchez-Gasca, "Dynamic Modeling of GE 1.5 and 3.6 MW Wind Turbine-Generators for Stability Simulations," in *IEEE Power Engineering Society General Meeting*, (Toronto, ON), pp. 13–17, 2003.
- [44] B. Kuo, *Automatic control systems*. Prentice Hall, 1995.
- [45] V. Akhmatov, *Induction generators for wind power*. Paul & Co. Pub. Consortium, 2007.

- [46] L. Hansen, L. Helle, F. Blaabjerg, E. Ritchie, S. Munk-Nielsen, H. Bindner, P. Sørensen, and B. Bak-Jensen, “Conceptual survey of generators and power electronics for wind turbines,” tech. rep., Risø National Laboratory, Roskilde, Denmark, 2001. Available at <http://citeseerx.ist.psu.edu/viewdoc/download?doi=10.1.1.130.9619&rep=rep1&type=pdf>.
- [47] D. Burnham, S. Santoso, and E. Muljadi, “Variable rotor-resistance control of wind turbine generators,” in *IEEE Power & Energy Society General Meeting*, (Calgary, AB), pp. 1–6, July 2009.
- [48] S. Chapman and Y. Man, *Electric machinery fundamentals*. McGraw-Hill, 1985.
- [49] N. Jenkins, J. Ekanayake, L. Holdsworth, and X. Wu, “Dynamic modeling of doubly fed induction generator wind turbines,” *IEEE Transactions on Power Systems*, vol. 18, no. 2, 2003.
- [50] Y. Lei, A. Mullane, G. Lightbody, and R. Yacamini, “Modeling of the wind turbine with a doubly fed induction generator for grid integration studies,” *IEEE Transactions on Energy Conversion*, vol. 21, no. 1, pp. 257–264, 2006.
- [51] S. Auddy, R. Varma, and M. Dang, “Field Validation of a Doubly Fed Induction Generator (DFIG) Model,” in *IEEE Canada Electrical Power Conference*, pp. 484–489, 2007.
- [52] J. Tande, E. Muljadi, O. Carlson, J. Pierik, A. Estanqueiro, P. Sørensen, M. OMalley, A. Mullane, O. Anaya-Lara, and B. Lemstrom, “Dynamic models of wind farms for power system studies—status by IEA Wind R&D Annex 21,” in *European Wind Energy Conference & Exhibition (EWEC)*, (London, UK), 2004.
- [53] J. Tande, J. Eek, E. Muljadi, O. Carlson, J. Pierik, J. Morren, A. Estanqueiro, P. Sørensen, M. OMalley, A. Mullane, O. Anaya-Lara, B. Lemstrom, and S. Uski-Joutsenvuo, “IEAWIND Annex XXI Final Technical Report: Dynamic models of wind farms for power system studies,” tech. rep., IEA Wind, 2007. Available at [http://www.ieawind.org/wnd\\_info/Publications\\_Tasks/IEA\\_Wind\\_Task\\_21\\_wind\\_farm\\_models\\_final%20report.pdf](http://www.ieawind.org/wnd_info/Publications_Tasks/IEA_Wind_Task_21_wind_farm_models_final%20report.pdf).
- [54] P. Krause, O. Wasynczuk, and S. Sudhoff, *Analysis of electric machinery and drive systems*. IEEE Press, 2002.
- [55] Z. Lubosny, *Wind turbine operation in electric power systems: advanced modeling*. Springer, 2003.
- [56] T. Hagglund and K. Astrom, “Revisiting the Ziegler-Nichols tuning rules for PI control,” *Asian Journal of Control*, vol. 4, no. 4, pp. 364–380, 2002.
- [57] A. D. Hansen and G. Michalke, “Fault ride-through capability of DFIG wind turbines,” *Renewable Energy*, vol. 32, no. 9, pp. 1594 – 1610, 2007.
- [58] A. Perdana and O. Carlson, “Aggregated Models of a Large Wind Farm Consisting of Variable Speed Wind Turbines for Power System Stability Studies,” in *Proceedings of 8th International Workshop on Large-Scale Integration of Wind Power into Power Systems as well as on Transmission Networks for Offshore Wind Farms*, (Bremen, Germany), October 2009.
- [59] J. Conroy and R. Watson, “Low-voltage ride-through of a full converter wind turbine with permanent magnet generator,” *Renewable Power Generation, IET*, vol. 1, pp. 182 –189, September 2007.

- [60] J. Morren, J. Pierik, and S. de Haan, "Voltage dip ride-through control of direct-drive wind turbines," in *39th International Universities Power Engineering Conference*, vol. 3, (Bristol, UK), pp. 934 – 938, 2004.
- [61] T. Tafticht, K. Agbossou, and A. Cheriti, "DC bus control of variable speed wind turbine using a buck-boost converter," in *IEEE Power Engineering Society General Meeting*, (Montreal, QC), July 2006.
- [62] S.-H. Song, S.-I. Kang, and N.-K. Hahm, "Implementation and control of grid connected AC-DC-AC power converter for variable speed wind energy conversion system," in *Eighteenth Annual IEEE Applied Power Electronics Conference and Exposition (APEC '03)*, vol. 1, (Miami Beach, FL), pp. 154 – 158, 2003.